Electromagnetic Modelling of High-speed Induction Motors

A thesis submitted to The University of Manchester for the degree of

Master of Philosophy

in the Faculty of Engineering and Physical Sciences

2016

Roberto Velazquez Velazquez

School of Electrical and Electronic Engineering

Table of Contents

Word count: 22,102

List of Figures

List of Tables

List of Notations

Symbol	Meaning	SI Units
a	complex number factor	
A	cross sectional area	m^2
A	magnetic vector potential	V*s/m
B	magnetic flux density	T
D	electric displacement field	C/m^2
E	electric field strength	V/m
E	electromotive force	V
F_r	radial force	N
F_t	tangential force	N
H	magnetic field strength	A/m
I_{ph}	current per phase	A
J	current density	A/m^2
k	wave number	1/m
k_w	winding factor	
l	axial length	m
N_c	number of conductors per slot	
N_{PH}	number of conductor per phase	
P_{in}	input power	W
p	pole pair number	
R	rotor resistance	Ω
s	slip	
S	layer thickness	M
t	time	s
T	torque	N*m
v	layer velocity	m/s
V	voltage	V

X	reactance	Ω
α	field constant	1/m
λ	wave length	m
μ	absolute permeability	H/m
ρ	electric charge density	C/m^2
ρ	layer electrical resistivity	Ω*m
σ	electrical conductivity	S/m
υ	harmonic number	
ω	angular velocity	rad/s
υ	harmonic number	

List of Abbreviations

AC	Alternating Current
CAD	Computer-aided Design
DC	Direct Current
EDM	Electrical Discharge Machining
FDM	Finite Difference Method
FE	Finite Element
FEA	Finite Element Analysis
FEMM	Finite Element Method Magnetics
HSEM	High-speed Electrical Machine
HSIM	High-speed Induction Machine
IM	Induction Machine
LR	Laminated Rotor
LIM	Linear Induction Machine
LRIM	Laminated Rotor Induction Machine
MCM	Magnetic Circuit Method
MLM	Multi-layer Model
mmf	magnetomotive force
PC	Personal computer
PM	Permanent Magnet
rpm	revolutions per minute
SR	Solid Rotor
SRIM	Solid Rotor Induction Machine
SRM	Synchronous Reluctance Machine
2-D	two-dimensional
3-D	three-dimensional

Abstract

The University of Manchester

Roberto Velazquez Velazquez

Master of Philosophy (MPhil)

Electromagnetic Modelling of High-speed Induction Motors

07/2016

Improvement in the power density of induction machines can be achieved when they operate at high rotational speeds using frequency converters that provide a higher frequency supply to the motor. Applications such as compressors require intrinsically high-speed operation. In these cases the mechanical integrity is prioritized over the electromagnetic performance and solid rotors are normally used instead of laminated rotors so they can withstand the peripheral and radial stresses caused by the high speeds.

Small skin depths are associated with solid rotor structures; this complicates the electromagnetic analysis when FE modelling is used because a fine mesh is typically required. Although analytical methods in general tend to be less accurate than FE models, they can provide faster and reasonably accurate results.

This thesis evaluates the use of an analytical multi-layer model as a preliminary design tool for determining the electromagnetic performance of high-speed copper-coated solid rotors. A simple FE model is developed in order to validate the results obtained from the analytical model.

The input to the analytical multi-layer and FE models is normally current; consequently they are modified to work with voltage as the input reference. The multi-layer model is compared under constant current operation and constant voltage operation. The limitations of the analytical multi-layer model are highlighted.

Declaration

No portion of the work referred to in the thesis has been submitted in support of an application for another degree or qualification of this or any other university or other institute of learning.

Copyright Statement

Acknowledgments

I would like to show my gratitude to my supervisor, Professor Sandy Smith, for all his patience and valuable guidance throughout this research project.

I am deeply grateful to CONACYT-Mexico for the financial support during this project.

Finally I wish to thank my family and friends for their constant encouragement and for always making me smile.

Chapter 1

Introduction

1.1 Overview

Advancements in frequency converter technology have made it possible to achieve higher rotational speeds in AC machines by increasing the input frequency. With high rotational speeds the overall efficiency of integrated systems generally improves. For example, gas compression applications that would normally require an electric motor coupled to a gearbox for the compression process, can be replaced by direct drive systems, which can occupy only approximately one third of the original space [1] without additional couplings or gearboxes. Examples of high-speed electrical machine (HSEM) applications are: automotive and power generation, flywheel energy storage systems, high-speed spindle systems, turbomolecular pumps, gas compressors, industrial air compressors and blowers, and microturbines [2].

There are different types of high-speed topologies that arise from the need to satisfy certain performance requirements. Usually for peripheral speeds above 300 m/s, solid rotor structures are preferred due to their robust mechanical integrity. Other advantages of using solid rotor structures include: reduced cost of manufacture, high reliability, high thermal durability, low vibration and low acoustic noise level [3], [4]. The main disadvantage of a solid rotor construction, however, is the poorer electromagnetic performance when compared to laminated rotors with copper cages. A copper-coated rotor can be used to improve the electromagnetic characteristics of solid rotors (SRs); such rotor topology is used throughout this thesis to perform the electromagnetic analysis.

1.2 Background and motivation

When operating at high rotational speeds, special mechanical, thermal and electromagnetic design considerations emerge. These are normally analysed using finite element (FE) software due to its accuracy, reliability and practicability. For the case of the electromagnetics in high-speed SRs, however, FE based methods can cause issues because of the small skin depths in the conducting areas. A very detailed mesh for example would increase significantly the computing times and when testing or trying different material parameters in the machine is required, FE analysis becomes very time-consuming. For this reason, the use of analytical models for the determination of the electromagnetic performance in high-speed machines becomes a sensible option because it can overcome the meshing and computational resources issues associated with FE modelling.

Research into SR machines reveals that there are available a number of analytical methods able to model the electromagnetics of such machines: [4]–[13]. Some of these methods obtain the equations of the magnetic fields for specific design cases. The level of complexity associated with any of the analytical methods depends on how comprehensive the method formulation is for modelling the physics of the problem. Analytical models that include in their formulation the cylindrical nature of the machine using Bessel functions are normally mathematically complex, but on the other hand they can deliver more accurate results. Depending on the machine topology, some models can be more appropriate to implement than others. For the case of copper-coated solid rotors, it is possible to implement an easy-to-use analytical model called the multi-layer model (MLM) whose formulation particularly suits the simple geometry of copper-coated SRs. The MLM has been used in the literature to determine the electromagnetic performances of high-speed induction machines (HSIMs) with solid rotors [6] and slitted solid rotors [4]. This practical analytical model is used to carry out the electromagnetic performances of the copper-coated solid rotor machine in this thesis.

1.3 Project aim and objectives

The project aims to assess the suitability of the MLM in the design of canned SRs for high-speed motor applications. Since the MLM is intended to be used as a rapid preliminary design tool to determine the electromagnetic performance of high-speed machines, its implementation seeks to be as practical as possible. For this reason the MLM (which operates with current as the input to the model) is solved using simple voltage source operation and accounts for the whole structure of the induction motor (IM), including the stator region, by means of the concept of surface admittance [14]. Although it is possible to modify the methodology of the MLM to take into account the effects of saturation [15], the MLM developed here, for simplicity, ignores saturation. Additionally, the capabilities of the MLM are extended from the original model by including magnetic anisotropy in the tangential direction of the machine, making possible to provide a better modelling in the stator slotted region.

To assess the suitability of the MLM for canned SRs in high-speed applications, a basic model of the motor is analysed using both: a classical numerical method (FE) and the MLM analytical method. These electromagnetic models are compared, and an assessment of the MLM based on the accuracy and computational times achieved, taking the FE modelling as reference, is provided.

1.4 Thesis structure

This section details how the thesis is organised and provides a brief summary of the remaining chapters which are structured as follows:

Chapter 2: Literature Review – High-speed Electrical Machines presents some of the research that has been carried out previously in the area of high-speed electrical machines. This includes a summary of the advantages, disadvantages, applications, topologies, physical limitations, etc. It also mentions the methods and techniques that are used in the literature to determine the electromagnetic performance of high-speed electrical machines. This chapter focuses on solid-rotor technologies with the emphasis

on copper-coated solid-rotor topology. This canned solid-rotor topology is analysed throughout subsequent chapters of the thesis.

Chapter 3: Finite Element Modelling provides the background and general concepts of the FEA method and of the FE software (FEMM) used to perform the modelling in this thesis. It describes the two types of FEMM approaches that are used to model the canned high-speed machine. An explanation of the relationship between the FEMM approaches is provided in appendix B.

Chapter 4: Analytical Modelling details the methodology of the MLM approach to calculate the electromagnetic performance of the canned solid-rotor IM model. Similar to chapter 3, in this chapter there are two approaches for the modelling of the machine, both of them are explained and the relationship between approaches is highlighted.

Chapter 5: Comparison and Review of the Analytical and Finite Element Models evaluates both numerical (FEMM) and analytical (MLM) models directly with each other. With the FE model as reference, it is possible to illustrate the effect of neglecting saturation in the analytical model by increasing the MLM current. Finally, a discussion is provided at the end of the chapter that addresses the scope of the analytical method.

Chapter 6: Conclusions and Future Work summarises the results obtained in this project and outlines what remains to be done in the analytical model that would improve its performance as a preliminary design tool for high-speed canned rotors.

Chapter 2

Literature Review – High-speed Electrical Machines

2.1 Overview

In this chapter a broad view of HSEMs is provided and more specifically induction machines. These have two main rotor topologies: laminated rotors (LRs) and SRs. This chapter starts with the generalities of different types of HSEMs: characteristics, applications, advantages, disadvantages, etc. and then it focus on HSIMs. The mechanical and electromagnetic performances of HSIMs are contrasted between their different rotor topologies. Methods used to calculate the electromagnetic performance of HSIMs is also revised.

2.2 Background

Frequency converter technology has made it possible to achieve high rotational speeds in AC machines by increasing the input frequency from conventional values of 50 and 60 (Hz) to up to 1000 (Hz) depending on the machine requirements. In general, when rotating electrical machines operate at high rotational speeds, not only the efficiency of the energy-conversion process improves [16] but also the power density, which allows replacing a 50/60 (Hz) machine with a smaller and faster version of the same rated power [17]. HSEMs can be integrated as complementary elements in existing high-speed mechanical applications, as in the case of automotive and power generation; or they can entirely replace existing mechanical systems, as in gas compressors [2]. HSEMs are usually preferred in the following applications: power-generation in hybrid vehicles for

the improvement of fuel efficiency; modern high-speed rotational flywheels which are able to achieve higher power densities than batteries in hybrid vehicles; spindle applications that require high rotational speeds; turbomolecular pumps for high vacuum environments; gas compressors which require a reduction of environmental, regulatory and maintenance issues; oil-free industrial air compressors and air blowers; and energy generation with microturbines which overcome space limitations [2]. Some HSEM examples are presented in Table 2.1; as can be seen there are different types of motors used for high-speed operation, such as: synchronous machines (Syncs), IMs, permanent magnet machines (PMs), claw pole, axial PM, synchronous reluctance (SRM) and switched reluctance motors. Each type of motor has certain advantages and the selection of a particular motor depends on the application requirements. Table 2.2 summarises some of their advantages and disadvantages.

Machine type	**Speed (krpm)**	**Output (kW)**	**Application**
Sync	5.25	30000	Load-commutated inverter
Sync	4.9	4200	Load-commutated inverter
IM	8	3500	-
IM	10	6750	Load-commutated inverter
IM	11	3300	Compressor
PM	15	1000	Cogeneration
IM	30	556	Cogeneration
PM	45	70	Machine tool spindle
SRM	48	32	Fuel pump
PM	60	200	Test machine
Claw	80	50	Generator for maglev
Claw	90	31	Hybrid car
Claw	100	25	Helium pump
PM	100	2.6	Mobile generator
IM	180	10	Test machine
IM	180	1.6	Machine tool spindle

Table 2.1 Examples of HSEMs [17].

Machine type	Advantage	Disadvantage
IM	Easy starting Open loop speed regulation	Rotor losses Low power factor at high-speed
PM	Large air gap length High power factor	Rotor robustness Iron loss at idling Field weakening
Claw	High power factor Field adjustment	Complicated rotor structure Rotor losses
Homopolar	High power factor Field adjustment Simple rotor structure	Windage losses Iron losses
Axial PM	High power factor Low rotor loss Large air gap length	Field weakening Complicated structure
SRM	Simple rotor structure Low rotor loss Field adjustment	Low power factor Windage loss Small air gap length
Switched reluctance	Simple rotor structure High rotor/inertia ratio Field adjustment	High vibration Windage loss Small air gap length

Table 2.2 Advantages and disadvantages of HSEMs [17].

In the design and analysis of HSEMs, mechanical, thermal and electromagnetic problems emerge due to the high rotational velocities. The most obvious problem is the design of the rotor, which has to withstand high mechanical stresses whilst maintaining good electromagnetic properties. There is a trade-off between the mechanical and electromagnetic properties; when the mechanical properties are enhanced, the electromagnetic ones are normally weakened and vice versa. Additionally, because high-speed in AC machines involves high supply frequencies, special thermal design is also required (Table 2.3 shows a comparison of the techniques used in HSEM cooling systems). Some of the key considerations in the design of HSEMs are: the rotor should be robust enough to withstand centrifugal forces and meet the shear stress at high rotational speeds; the electromagnetic losses should be as low as possible because the heat produced in the rotor is difficult to remove; the shaft supporting systems should be stable and reliable whilst reducing losses and maintenance; high rotor critical speeds helps to avoid vibrations due to flexible shaft movements; and the cooling system should be as simple as possible [17]. At the same time special requirements also emerge for

controllers, sensors and power electronics: appropriate power electronic circuits that can operate at high frequency voltage/current and high efficiency; fast controllers that allow fast calculation of voltage and current; and simple and robust sensors that detect angular position as well as speed [17].

Cooling system	**Current density (A/mm^2)**	**Advantages**	**Disadvantages**
Fins and heat sinks	5 to 8	Simple method	Increase in weight and size
Water or oil jacket	10 to 15	Effective stator cooling	Increase in diameter and weight
Direct liquid cooling and hollow conductors	up to 30	Very intensive cooling of the stator winding	Increase in weight and size. Too expensive for machines rated below 200 (kW)
Spray oil-cooled end turns of rotor winding	over 28	Very intensive cooling of the rotor winding	Wet rotor; contamination of cooling medium (oil) with time
Liquid cooled wedges	8 to 15	Intensive cooling of rotor winding	Does not effectively cool the rotor poles
Cold plates between poles and rectangular wire rotor winding	about 22	Intensive cooling of rotor winding	Requires installation of cold plates in rotor and cooling medium circulation

Table 2.3 Cooling techniques in HSEMs [3].

At this point it is important to mention the different perspectives from which the term "high-speed" can be used [4] and also to show which ones could be regarded as more distinctive when referring to "high-speed" machines. The most obvious perspective would be the mechanical point of view. Peripheral rotor velocities over 100 (m/s) are regarded as high-speed [18]. However, the mechanical parameter should not be taken as sole criterion for "high-speed" because very large machines operating at 50/60 (Hz), which are rarely regarded as high-speed, would then also enter the high-speed category [19]. Hence, the other perspective that is normally used to classify "high-speed" in HSEMs is the power electronic supply involving frequencies in the range of hundreds of hertz [4].

There are physical limitations between the rated power and rated speed in HSEMs. These limitations depend on the machine type. As can be seen from Figure 2.1, induction machines, and SR machines particularly, are well suited for very high-speeds close to 250 (krpm) leading to the highest possible rpm/kW ratio. In a similar way, using high-strength retention mechanisms (Inconel, titanium or carbon fibre) [2], PM machines can also reach high rotational speeds and deliver a high rpm/kW ratio. Figure 2.1 also shows the limitations that laminated rotor induction machines (LRIMs) have in attaining higher speeds, falling behind in comparison to SR and PM machines. Table 2.4 summarises the high-speed limits in electrical machines.

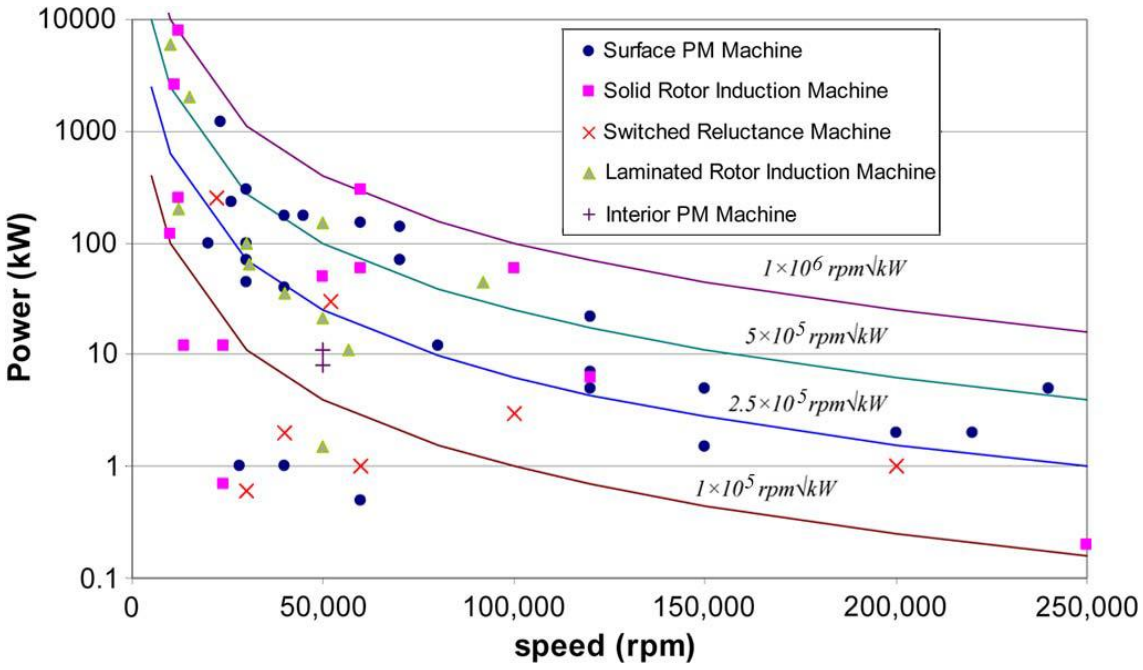

Figure 2.1 Power and speed of different types of HSEMs [2].

Machine type	**rpm/kW**	**m/s**
Solid-rotor IM	$1x10^6$	400
Surface PM with sleeve (no rotor laminations)	$8x10^5$	300
Laminated rotor IM with high strength SiFe	$6x10^5$	280
SR with high strength VCoFe laminations	$3.5x10^5$	210
Laminated rotor IM with normal SiFe	$2.5x10^5$	185
IPM with high strength SiFe laminations	$1.5x10^5$	230

Table 2.4 Summary of the limits in HSEMs [2].

2.3 High-speed induction machines

Due to their mechanical robustness and simple construction HSIMs are frequently used in direct-drive systems (see Figure 2.2) that replace high-speed systems composed of step-up gears, mechanical couplings and driven machines (e.g. pumps, fans, compressors, etc.). The overall system efficiency is improved and the inverter drive systems are smaller by a half to a third of the original installation space [1]. There are two different ways in which the feasibility of IMs has been investigated for high-speed applications, by improving either: the mechanical properties of laminated rotors or the electromagnetic properties of solid rotors [20].

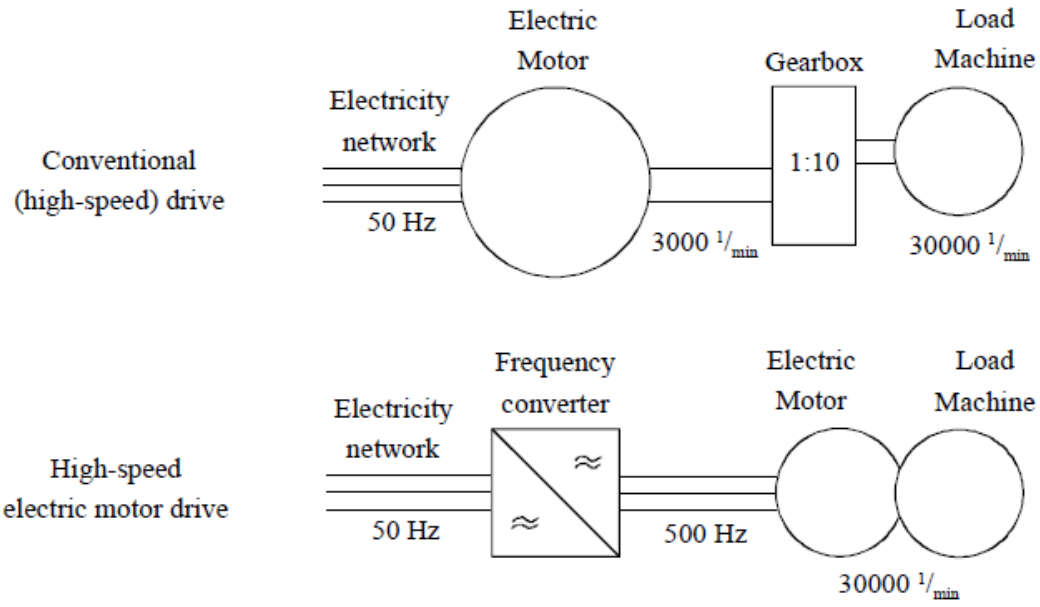

Figure 2.2 Replacement of a conventional drive system by a high-speed electric drive [21].

2.3.1 Laminated rotor HSIMs

LRIMs are broadly designed to be used with the standard utility supply of 50/ 60 (Hz) due to their good electromagnetic performance in reducing the rotor losses. Once inverter-driven AC variable high-speed systems became available, research on LRIMs for high-speed applications focused on bringing the good electromagnetic properties of the LRIMs into the high-speed area as [1] shows.

LRs can be designed to meet a mechanical high-speed criteria from 6 (krpm) to up to 20 (krpm) and in the power range between 4 (MW) to 25 (MW) [20]. However, it is not always possible to implement LR constructions in high-speed applications as important mechanical restrictions arise from high rotational speeds. In general, subcritical operation of a laminated rotor requires a smaller rotor (compared to SRs) in order to compensate for the low bending stiffness, which decreases the natural frequency of the machine [21]. At high rotational speeds the laminations are subject to centrifugal stresses and bending of the rotor, causing them to move so that in terms of unbalance a solid rotor has a better performance [21]. Nevertheless, LRs have better electromagnetic properties than SRs, e.g.: low slip, low circulating current, high power factor, high efficiency, etc. and if the LR topology (Figures 2.3 and 2.4) in [20], [22] is adopted (LR with embedded copper bars with copper end plates and end shafts assembled by tie rods) the rotor can reach a peripheral speeds up to 300 (m/s), but it often requires a laborious manufacturing process and some operational constraints. The manufacture of LRs for high-speed applications tends to be demanding as mentioned in [20], [22]; even for simpler structures as in [23] where cutting of the machine laminations was done using EDM instead of water jet or laser cutting because the latter two resulted in lamination vibration.

In general, a laminated rotor construction should be used whenever possible for high-speed applications due to the better electromagnetic performance. But at very high power and speed, solid rotors may be the only possible solution due to the mechanical constraints. Copper-coated rotors are also an option at very high-speeds. [21]

Examples of high-speed laminated rotors are: 200 (kW), 200 (Hz), 2-pole motor [1]; 15 (Hp), 960 (Hz), 2-pole compressor [24]; 1.5 (kW), 833 (Hz), 2-pole and 1.5 (kW), 1667 (Hz), 4-pole motors [23]; 10 (MW), 200 (Hz), 2-pole compressor [20]; 235 (W), 400 (Hz), 4-pole motor [25]; 2400 (kW), 179 (Hz), 2-pole motor [22]; 60 (kW), 1000 (Hz), 2-pole motor [21].

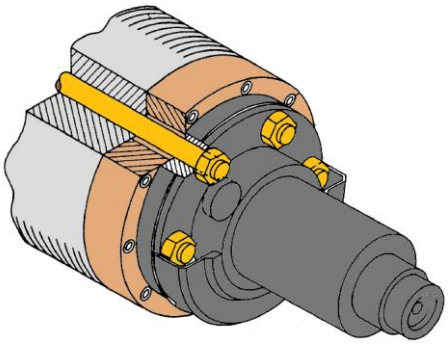

Figure 2.3 Laminated rotor with embedded squirrel cage [20].

Figure 2.4 Laminated rotor with embedded squirrel cage [22].

2.3.2 Solid-rotor HSIMs

Research into solid-rotor induction machines (SRIMs) started in the 1920s by the contribution of the Russian scientists Shenfier and Bruk. The study of SRIMs continued developing during the 20th century with the theory for the analysis of electromagnetic fields on such machines. The progress of SRIMs has been accompanied by the necessity to remove the drawbacks of LRIMs: simplifying and reducing manufacture costs of the rotor; improving mechanical integrity of the rotor at high-speeds as well as the reliability; increasing the lifetime of the rotor compared to wound or LRs; and reducing the vibration and acoustic noise levels. Although SRIMs can possess the advantages listed above, they intrinsically have a lower electrical performance compared to laminated rotors (e.g. lower output power, lower power factor, lower efficiency, higher no-load slip and higher mechanical time constant). The electrical performance of SRIMs, however, can be improved by reducing the rotor impedance through: the selection of the SR material with a small relative magnetic permeability-to-electric conductivity ratio; the

use of a layered rotor with high magnetic permeability and high conductivity materials; and the use of an additional cage winding on the rotor. [3]

There are a number of topologies for SRs (built from a solid piece of ferromagnetic material) used in the area of HSIMs. The simplest topology of all is the smooth SR core (Figure 2.5a) which has the best mechanical and fluid dynamical properties; however, it is the poorest with regard to its electromagnetic properties [4]. For this reason, there are other topologies that seek an improvement on the electromagnetic properties of the SR, e.g. slitted SR, cage SR and copper-coated SR (Figures 2.5b, 2.5c and 2.5d respectively). Unfortunately, for each topology there is a trade-off between their mechanical and electromagnetic properties. Regardless of the topology implemented, HSIMs are often designed to operate below the first critical speed (first specific frequency) [6].

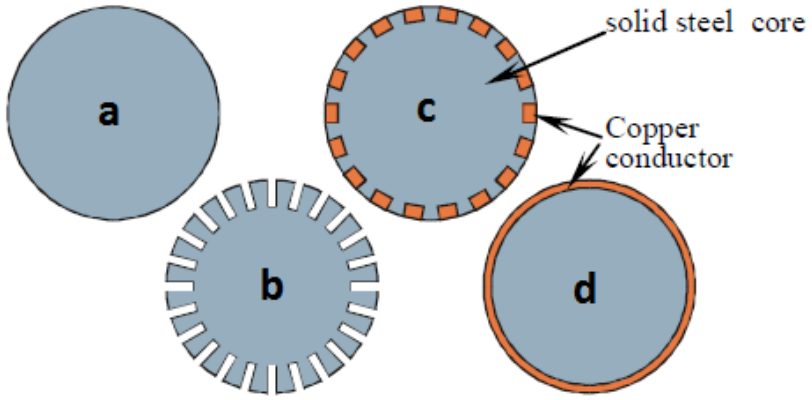

Figure 2.5 Different solid rotor topologies (modified from [26]).

Slitted SRs have been investigated since the 1950's. In 1958, Peesel [4] tested 25 different slitted SRs for a 19 (kW), 50 (Hz), 4-pole induction motor; in 1967, Dorairaj [27] studied the effects of axial slits, end rings and cage windings for a 3 (hp), 50 (Hz), 6-pole induction motor and two years later, Rajagopalan and Balarama [28] presented an approach to analyse these type of rotors. In the high-speed area, slitted SRs have been researched by a number of authors [4], [20], [21], [26], [29]–[34]. The rotor slitting improves the penetration depth of the flux density in the rotor material and has a significant impact in the rotor performance producing better torque properties, higher

efficiency and higher power factor [33]. Deeper slitting provides better torque-generation capabilities; however, the slits can produce crack propagation increasing the vulnerability to fatigue damage [32]; for this reason, slitting is usually limited to no more than 50% of the radius of the rotor [33]. In addition to mechanical issues (at the expense of electromagnetic improvement), air friction in slitted SRs is 60% higher than in smooth rotors [33]. Examples of high-speed slitted SRIMs are: 430 (kW), 170 (Hz), 2-pole induction motor [32]; 9(MW), 200 (Hz), 2-pole induction motor [32]; 8 (MW), 200 (Hz), 2-pole gas compressor; [33]; 120 (kW), 170 (Hz), 2-pole gas compressor [33] .

Cage type solid rotors further improve the electromagnetic properties because the cage serves as a low-resistivity path for the induced currents [21]. The mechanical performance, however, of the SR structure is again compromised by adding copper bars in order to achieve better electromagnetic performance. As the rotational speed increases so do the centrifugal forces on the copper bars; this constrains the tip peripheral speed to roughly 180 (m/s) for this type of topology [7]. Examples of squirrel-cage SRIMs are: 60 (kW), 1000 (Hz), 2-pole [21] and 10 (MW), 200 (Hz), 2-pole [35] induction motors.

Copper-coated SRs are from a manufacturing point of view, very similar to smooth SRs. They have the same rotor structure as smooth SRs but with an additional thin copper layer coating on the rotor surface. The copper layer may cover the entire rotor acting as the end rings as well. The objective of this topology is to prioritise the mechanical strength but creating a main circuit path for the fundamental current by means of the copper coating (part of the fundamental current, however, also circulates in the steel rotor core) [21]. The bonding between the coating and the core needs to achieve a strength of approximately 100 (MPa), which is more than acceptable for a thin copper coating [21]. This type of topology has a tip speed limit of 550 (m/s) [7]. The higher stator-iron-to-rotor-iron air gap, compared to cage constructions, also reduces the higher harmonics by increasing the copper coating thickness, but there is a limit in the coating thickness. Any increase above this limit leads to a reduction in the torque developed [8] (for example, the 800 Hz, 2-pole machine in [8] reaches its maximum torque when the copper layer is about 0.5 mm). Although the stator-iron-to-rotor-iron air gap reduces the harmonic content of the magnetic flux seen by the rotor, it also leads to a higher magnetization current and higher stator winding losses [21]. Copper-coated SRIMs can be manufactured in the range of 70 to 250 (kW) and 50 to 18 (krpm) respectively [21].

Research examples in copper-coated SRIMs are: 300 (kW), 1000 (Hz), 2-pole compressor [7]; 800 (Hz), 2-pole induction machine [8]; 1500 (W), 666 (Hz), 2-pole induction machine [30]; 60 (kW), 1000 (Hz), 2-pole compressor [21].

An interesting comparative study on the mechanical and electromagnetic properties of smooth, slitted, cage and copper-coated SRs (Figure 2.5) is presented in [26]. For the same stator parameters, rotor size and rated rotating speed of 60 (krpm) in the four topologies of SRIMs, it was found that: the best mechanical properties were achieved by the smooth SR construction followed by the copper-coated SR, slitted SR and finally the cage SR. From the electromagnetic viewpoint, however, the performance of the solid rotor topologies was different; with the cage SR as the topology with the best performance and the smooth SR the worst. The highest starting torque was achieved by the cage SR followed by the copper-coated SR, then the slitted SR and lastly the smooth SR. The rotor slip of the smooth and slitted SRs tended to increase compared to the cage and copper-coated SRs. Between the SR topologies the lowest stator winding current (with the same load torque) was achieved by the cage SR, then the copper-coated SR, followed by the slitted SR and finally the smooth SR.

2.3.3 Electromagnetic methods to analyse HSIMs

In the literature there are different methods that can be used to model the electromagnetic performances of HSIMs. These methods can be classified as follows: numerical methods, equivalent circuit methods and analytical methods.

Numerical methods [8], [9], [13], [21], [23]–[26], [29]–[31], [34]–[40] (finite elements in particular) are more frequently used when analysing general HSIMs. This has to do with their reliability and practicability which allows modelling from simple structures to more complex topologies. Time-stepping numerical methods [24], [29], [34]–[37] are also used regularly to obtain better accuracy in the predictions of the motor operation and also to optimise the design, because it takes into account the nonlinear behaviour of the materials in the machine. A finer mesh usually provides more accurate results; however, this also increases the processing time. A full 3-D time-stepping FE analysis of solid rotor structures would still be a very demanding problem for ordinary PC's to solve in a

reasonable time [34]. For this reason, a number of approaches can be adopted when stepping-time is required. In [34], for example, the electromagnetic torque of a 180 (kW), 10.2 (krpm) SRIM is calculated with a 2-D representation instead of a full 3-D model. The 3-D time-stepping model of the end effects is simplified by solving a 2-D model that modifies the rotor effective resistivity using a corresponding end effect factor. Another approach consists of simplifying the meshing of the machine: the cross-section of a motor for example can be discretised using the 2-D finite difference method instead of the finite element method (FEM) [35]. Numerical methods can also be coupled with analytical methods as a technique to reduce the computing time [8], [9], [13]; [9] and [13] for example combine reluctance networks with the FE model using 2-D and 3-D approaches respectively to determine the electromagnetic performances faster than implementing solely the FEM.

Equivalent circuit methods can also be used to determine the parameters of the machine. For high-speed laminated cage rotors, the classical equivalent circuit is well suited to calculate the electromagnetic performances of the machines [41] due to their similarity to standard induction machines. However, this is not the case for smooth solid rotors because they lack the well-defined current paths found in conventional cage rotors. There have been investigations that seek to represent the operational behaviour of SRs using equivalent circuits. One of the first equivalents circuits for high-speed SRs [1], considered the solid core as a secondary conductor. The solid core allows the flow of current in the rotor; for the locked rotor condition the power factor of the solid rotor core is low, compared to a laminated core. It is also possible to model canned SRIMs using an equivalent circuit that includes the eddy-currents in all regions directly into the circuit [10].

There are a number of analytical methods that can be used for electromagnetic modelling of HSIMs [4]–[6], [11], [12], [28], [42]. These methods tend to be based on Maxwell's equations that represent the physics of electromagnetic problems. When an analytical method is used, it avoids time stepping and meshing of the rotor; this translates directly in a reduction in the processing time and improves practicability as well, because at high-speeds the skin depths are generally very small and as consequence a very fine discretisation in an FE model would be required [8]. There are some drawbacks however whilst applying analytical methods. Analytical models that represent the physics of the

problem would be expected to be mathematically complex, e.g. solving in a polar coordinate system or solving a 3-D analytical model. On the other hand, in order to simplify the model, some parts of the problem are not considered in detail or not considered at all; the accuracy of the results would be reduced accordingly. A compromise therefore between accuracy and complexity of the model exists. In the literature the analytical models of HSIM with SRs focus on three topologies: smooth, slitted and copper-coated SRs. Smooth SRs can be analysed with the multi-layer transfer-matrix method (multi-layer model) as in [6], where the 3-D effects of the machine are included in the analytical model. Analytical methods that use a polar coordinate system to calculate the fields in smooth SRs, take into account the effects of the rotor curvature [5], which is an important consideration in slitted rotors. Good agreement can be obtained when a detailed Fourier analysis [11] is implemented on high-speed smooth SRs; this analysis can model the effects of curvature and also the stator slotting effects on the field distribution of the machine [12]. For the case of slitted SRs, the effect of axial slits on the performance of the machine can be modelled using an analytical method [28] that models the tooth and slit profile as a flux line. In [4] the performance of a slitted SR is determined using the multi-layer transfer-matrix method, which is modified by introducing an end-effect factor and a curvature factor into the model. For copper-coated SRs, an analytical method to calculate the electromagnetic performance of an HSIM is presented in [42]; here a 300 (kW), 60 (krpm) 2-pole machine for an air compressor is analysed using a double-layered structure of copper and steel. No literature was found, however, for copper-coated HSIMs using the multi-layer model. The simple geometry of the copper-coated SR is particularly well suited to the practical and versatile multi-layer model; this method is adopted therefore in this thesis for the calculation of the electromagnetic performance of the HSIM showed in appendix A.

2.4 Summary

Literature on HSEMs was reviewed with the emphasis on the main HSIM topologies: LR; smooth SR; slitted SR; cage SR and copper-coated SR. Each topology has strengths and weaknesses, generally linked by a trade-off between the mechanical and the electromagnetic properties. The selection of one topology over another depends on the requirements. The rotor speed is normally the main factor that determines what topology should be implemented. Whenever possible the LR should be used due to the good electromagnetic performance; however, as the peripheral speed increases SRs are a more sensible choice because of their mechanical integrity and simpler manufacture. The HSIM topology analysed in this thesis is the copper-coated SR topology which can offer good mechanical and electromagnetic performances.

Literature on the methods used to analyse the electromagnetic performance of HSIMs was also reviewed. There are three main methods used to model HSIMs: numerical methods, equivalent circuits and analytical methods. Although accurate, numerical methods tend to consume significantly more processing time than analytical methods. On the other hand analytical methods become mathematically complex for detailed models. The approach followed in this thesis is a simple analytical method used as a preliminary design tool to determine the electromagnetic performance of copper-coated machines. The topology of these types of machines is well-suited to the multi-layer model formulation.

Chapter 3

Finite Element Modelling

3.1 Overview

FE modelling is an important tool in the design and simulation process for electrical machines. It has become the predominant method in engineering to analyse complex problems. With due care the FE modelling delivers accurate results close to the real measurements.

This chapter starts with a general insight into FE modelling from its background to some specific techniques used in electrical motors. There is an introduction to FEMM, which was the FE software used to carry out the analysis of the HSIM, with special emphasis on the magnetics module. This chapter provides methods to correctly simulate the canned HSIM in FEMM. Section 3.4.3 of the chapter presents the results (torque, voltage, current and can losses) of the HSIM under certain conditions. The results obtained in this chapter, using the FE method, will be compared with analytical model results in later chapters.

3.2 The finite element method

3.2.1 Introduction

FEM is a well-known numerical iterative technique with a broad application range over a variety of complex physical problems. In engineering systems it has become a fundamental tool for modelling and simulation due to its ability to solve complex

problems where there is little or no information about the behaviour and outcome of the problem. This versatility of the method is related to its capability to approximate the model using discrete elements, which make possible an accurate model in practical problems. The reliability of the method allows it to be applied directly to reducing budget by minimising prototyping costs to meet a given performance. As a result the FEM has positioned itself as the preferred method in the analysis of engineering systems, especially when a simple analytical solution is not available.

3.2.2 History

The origins of the FEM can be traced back to 1851, when Shellback devised a procedure to determine the differential equation of a surface of minimum area within a delimiting contour; it consisted in discretizing such surface into several triangles and then, by means of a finite difference expression, obtain the resultant triangle-divided area. Shellback's contribution was used in the early 1900s to approximate the behaviour of structural frameworks. However it was not until 1943 that the origin of the present-day FEM came to light thanks to Courant's work. He presented a method to find the torsional rigidity of a hollow shaft by means of several triangles; in each one of them an interpolation was used to find the stress across them, so that the stress would vary linearly as a function of the distribution of intersecting points in the triangles (also known as nodes). In the mid-1950s the pursuit in the aircraft industry for determining the stresses induced in aircraft wings made engineers develop the FEM further. In particular the work of Tuner, Clough, Martin and Topp in 1956 related to the modelling of the wing skin using three-node triangles was a fundamental contribution to the development of the FEM. In 1960 Clough formally introduced the name of finite element to the method. At the same time the mathematical basis of the method was recognized as a form of the classical Rayleigh-Ritz method which along with the developing processing capabilities of the digital computer, encouraged the development and popularity of the method in a diverse range of problems. By the late 1960s Zienkiewicz and Cheung produced a general interpretation of the method, showing its applicability to any general field problem. Today the FEM is used mainly within applied mathematics for the solution of complex ordinary and partial differential equations; and engineering, where the FEM has become the industry standard for the solution of many engineering systems. [43]

3.2.3 Computer-aided analysis

It is worth pointing out that the popularity and development of the FEM would not have been the same if there had not been the practical means to apply the method; fortunately the reducing processing times of the digital computer made its implementation viable and still continues to develop. Today there are many software packages that incorporate the FEM in the solution to specific types of problems. They basically solve, with suitable boundary conditions, a set of differential equations which describe the physics of the problems. FEM essentially solves a set of differential equations numerically, as a matrix arranged of algebraic equations in an iterative process.

In general terms, the computer-aided analysis of problems using the FEM is performed using four standard steps. First, the problem domain is converted into a geometrical representation so that the geometry of the problem becomes a collection of elements such as lines, arcs, surfaces, etc. The task of setting up the geometry of the problem can be simplified with the use of CAD software. Processing times can also be reduced if it is possible to find symmetrical patterns or if the problem can be modelled in a 2-D rather than 3-D. Secondly, the material properties of the problem are defined; here the material properties (thermal, mechanical, electrical, etc.) are assigned to the model. In the third step, the problem boundary and the initial and loading conditions are specified for the problem; they are the information regarding the problem environment. The final step is to mesh the geometry; here the geometry of the problem is discretised into small elements, also known as cells. By discretising the problem into finite elements the solution can then be approximated by polynomial functions in each element, enabling the solution of the whole problem domain to be determined by the contribution of every elemental solution. The meshing is commonly carried out using triangular elements due to their flexibility in modelling complex geometries. However, their drawback is that they are less accurate than quadrilateral elements. The accuracy of the results depends on how detailed the meshing is. On the other hand the processing time increases proportionally to the number of elements in the mesh. [44]

Many engineering applications have benefited from the implementation of the FEM. For example in civil engineering, the FEM is used in structures for the static analysis of bridges, the natural frequencies for structure stability, the response of structures to

aperiodic loads; in the aircraft industry it is used for the static analysis of aircraft wings, fuselages, stability of the aircraft and the dynamic response of aircraft and spacecraft to aperiodic loads; in heat conduction for steady-state temperature distribution in solids and fluids; in hydraulic engineering for analysis of potential flows; in nuclear engineering for analysis of pressure vessels and containment structures; in mechanical design for stress analysis problems, stability of linkages, gears, and machine tools; and in electrical machines and electromagnetics for steady-state analysis of synchronous and induction machines, eddy current, core losses, and transient behaviour of motors and actuators. [43]

3.2.4 Finite element method in magnetics

3.2.4.1 Overview

In complex electromagnetic problems the accuracy of the FEM is noticeable when comparing it to traditional analytical methods like the magnetic circuit method (MCM). The FEM as opposed to the MCM does not require any assumption on the direction of the magnetic flux paths and this makes the FEM particularly useful in design because it does not rely on empirical correction factors as the MCM does (for example the effects of flux fringing, saturation and leakage flux). The power of the FEM has meant it can be employed in many electrical machine problems, for example, improved quantification of the effects of magnetic saturation and complex geometries on motor efficiency; and calculation of the magnetic field distribution around the motor perimeter in the air gap region. [45]

3.2.4.2 Computer modelling

Computer-aided modelling using the FEM in magnetics is divided into three steps: pre-processing, processing and post-processing respectively. Pre-processing defines and prepares the problem for discretisation and approximation using the problem environmental input information: geometry, materials and boundary conditions. The processing step obtains the field solution over the problem domain. Solver accuracy will

depend on the input error bounds and as consequence, the iteration steps and processing time will be affected accordingly. Finally, the post-processing step uses the solution generated in the processing stage and prepares it to calculate field quantities and to evaluate macroscopic quantities such as forces. The post-processing step makes use of different tools for the analysis of the results, such as: diagrams, flux plots, plots of the lines of constant potential, etc. [46]

Since mesh generation influences directly the accuracy of the results in the solution of the problem, it is worth mentioning some characteristics of the meshing process in computer-aided analysis. Knowing that mesh generation is the automated process of discretising the problem domain into elements; it should run with the minimum of the user interaction and in doing so avoid as many errors as possible. Errors associated with the problem solution are usually related to an inadequate meshing strategy. Automated mesh adaptation offers a convenient mesh strategy because it improves the meshing using an iterative process. If automated meshing is available, the initial mesh should be done with the minimum of discretisation because the meshing algorithm itself will strategically enhance the quality of the discretisation in successive computation steps. In meshing 2-D models, the elements are usually triangular whereas for 3-D problems they are tetrahedrons [46]. The more time-consuming three-dimensional meshing can be approached using two strategies: mesh extrusion, which extrudes a 2-D mesh in the third dimension, and solid modelling which first discretises the surface of the model and then meshes the volume of the solid directly [46].

The FEM can analyse all types of electrical machine, which makes the task of improving existing designs practical. Although all electric machine models, as with any other physical problem, are intrinsically 3-D in nature, they are frequently simplified into 2-D models which can still provide accurate results with the benefit of reducing the computational processing time. However, in some cases 2-D modelling produces less accurate results, so to maintain the accuracy of the method in different scenarios other FE implementations can be found: three-dimensional, one-dimensional, zero-dimensional and open-boundary. For example, for motors with very short axial stacks, a 3-D finite model will produce better results than a 2-D model [47], [48]. Zero-dimensional and one-dimensional are also used to model conventional circuit elements (resistors, capacitors and inductors) and motor excitation circuits (voltage sources) respectively

[49], [50]. Open-boundary, as its name suggests, is used for the analysis of fields with no obvious boundary, end-region fluxes in electric motors for example [51].

FEM strategies in motor design are performed using two approaches. In the first one, the FEM is combined with the equivalent circuit method. Circuit parameters of the motor such as resistances, inductances and impedances are extracted from the FEM model to provide the values for the circuit simulation which performs the analysis of the motor performance over its operational range. Time-stepping FE on the other hand, analyses the motor performance exclusively using the FEM, in this time-varing scheme the equivalent circuit method is not able to handle magnetic saturation adequately. For some operational conditions, magnetic saturation in the magnetic circuit reduces the accuracy of the approach because the circuit parameters are assumed to be linear. Although it is possible to approximate the effect of saturation in the equivalent circuit (by varying the circuit parameters accordingly with the motor speed), the approach still lacks the means to determine important information such as cogging torques and the transient behaviour. Time-stepping, which is the second approach to motor design, directly computes in detail the motor performance. The time-stepping model is able to overcome the limitations from the equivalent circuit method by using zero-, one-, and three-dimensional finite elements in the calculation of the motor performance, including cogging torques and transient behaviour as well. Drive circuits can also be attached to the model using zero-dimensional FEs. Since the time-stepping FE predicts the performance of the motor (torque, eddy currents, etc.) as functions of time, the rotor data (at constant speed or attached to the mechanical load) is acquired directly by allowing the rotor to move. As might be expected, the main limitation of the time-stepping model is the significantly increase of computational resources (in contrast to the equivalent circuit software). [45]

3.2.4.3 Software packages

For practicability magnetic FEM is normally integrated into specialised software. There are many different options of software available, each one of them with its own strengths and weaknesses. Nonetheless, they share in common the aim to make the task of designing and modelling easier. Software packages usually include modules that provide better interaction between the software and the user. At the pre-processing stage it is

common to find: graphical drawing tools to generate the geometry; a material library manager to edit material properties; a file manager to transfer data; and the option to import and export geometries by means of CAD file formats. In the processing stage the relevant tools are: the mesh generator, which undertakes the numerical discretisation of the problem domain; and the equation solver, which completes the problem solution of the mesh generated. In the post-processing stage it is convenient to have tools to evaluate the field solution such as: colour distributed plots; plots of the lines of constant potential; flux plots; and the calculation of physical quantities such as the flux density, field strength or forces associated with the solution.

For the analysis and modelling of electromagnetic problems, as well as electrical machines, there are a number of software packages available to choose from. Among the well-known packages are: 'ANSYS', 'CAMEDA', 'FLUX', 'MAXWELL', 'MEGA', 'QFIELD', 'VECTOR-FIELD' and 'FEMM'. In this thesis the analysis of the HSIM is carried out using 'FEMM' which is introduced and described in the following section.

3.3 FEMM

3.3.1 Introduction

Finite Element Method Magnetics (FEMM) is a FE software package which can model: magnetic, electrostatic, heat flow and current flow problems. Problems in FEMM are solved by executing three programs: 'femm.exe', 'triangle.exe' and the solver, which depends on the nature of the problem: 'fkern.exe' for magnetics; 'belasolv.exe' for electrostatics; 'hsolv.exe' for heat flow problems or 'csolv.exe' for current flow problems. 'femm.exe' is the interactive shell that establishes the interface in the pre-processor and post-processor stages; it is able to import and export CAD files '.dxf' which makes the generation and analysis of geometries easier. 'triangle.exe' generates the mesh of the problem using triangular finite elements, for which the solution is approximated by interpolating potential values at the nodes of the triangles. The solvers, implemented at the processing stage, compute the partial differential equations and

determine the problem solution using an iterative process, which converges to a specified error and provides the solution to be used in the post-processing stage.

FEMM makes available an option to simplify the problem geometry in axisymmetric problems, performing a 2-D simulation. A 3-D problem therefore can often be modelled by recasting it into an appropriate 2-D representation. Although FEMM is not able to take into account moving elements (i.e. the rotor), or set the voltage as input to the machine directly; it can model such problems by implementing an approach that will be described in section 3.4.

Despite of some limintations of FEMM in comparison to commercial software packages, FEMM can provide accurate results. There are a number of applications in electric machines and other electrical engineering problems in which FEMM has been used in modelling and designing [52]–[59]. For example, in [57] FEMM presented good agreement with prototypes in the redesign of a PM DC motor.

To gain insight into FEMM operation the following section covers key points in the use of FEMM; however, only the magnetic module [60] is discussed since this thesis only focuses on the electromagnetic analysis of HSIMs.

3.3.2 Partial differential equations

FEMM, as with any other FE software, computes the solution of the relevant partial differential equations that describe the problem. The partial differential equations for magnetic problems are obviously Maxwell's equations. In magnetics there are two operating conditions from which Maxwell's equations are implemented: when the fields are time-invariant; and when they are time-variant. In both cases the displacement currents in Maxwell's equations are ignored because at 'low frequencies' the effects of displacement current can be neglected [61]. The next section shows the development of Maxwell's equations that leads to the partial differential equations that FEMM uses to solve a problem for both: magnetostatic and time-harmonic problems.

Using Maxwell's equations:

$$\nabla \times E = -\frac{\partial B}{\partial t} \tag{3.1}$$

$$\nabla \cdot D = \rho \tag{3.2}$$

$$\nabla \times H = J + \frac{\partial D}{\partial t} \tag{3.3}$$

$$\nabla \cdot B = 0 \tag{3.4}$$

For magnetostatic problems there is no variation in time so the Maxwell's equations that describe such conditions become:

$$\nabla \times H = J \tag{3.5}$$

$$\nabla \cdot B = 0 \tag{3.6}$$

B and *H* are subjected to the constitutive relationship:

$$\mu(B) = \frac{B}{H(B)} \tag{3.7}$$

FEMM solves eqns. 3.5 and 3.6 using a magnetic vector potential approach by finding the vector potential solution *A* which satisfies all the previous conditions:

$$\nabla \times \left(\frac{1}{\mu(B)} \nabla \times A \right) = J \tag{3.8}$$

Where the flux density is given by the following vector potential relationship:

$$B = \nabla \times A \tag{3.9}$$

In time-harmonic magnetic problems the time-varying fields induce eddy currents inside materials of non-zero conductivity. Noting that displacement currents (eqn. 3.3) are disregarded, it is possible to carry out a phasor transformation that yields a steady-state

equation. The resultant partial differential equation, eqn. 3.10, is used by FEMM for harmonic magnetic problems in which the field is varying at one fixed angular frequency. As can be seen from eqns. 3.8 and 3.10 FEMM is current driven, which means the natural input source in FEMM is current.

$$\nabla \times \left(\frac{1}{\mu_{eff}(B)} \nabla \times a \right) = -j\omega\sigma a + \hat{J} - \sigma \nabla V \tag{3.10}$$

Where ∇V is an additional voltage gradient, $\hat{J}$ is the phasor transform of the applied current sources and the vector potential is given by the phasor transformation:

$$A = \mathrm{Re}\left[a(\cos(\omega t) + j\sin(\omega t))\right] = \mathrm{Re}\left[ae^{j\omega t}\right] \tag{3.11}$$

3.3.3 Boundary conditions

In the FEMM software, there are five magnetic boundary conditions: Dirichlet, Neumann, Robin, periodic and antiperiodic; they are needed to ensure a unique solution. The Dirichlet boundary represents a fixed constant value for the magnetic potential; the condition is particularly useful to prevent the flux from crossing a boundary. The Neumann boundary specifies the normal gradient of potential on a boundary; for example the behaviour of highly permeable materials would be represented by assigning the value of 0 which could force the flux to cross the boundary at right angles. The combination of Dirichlet and Neumann conditions represents the Robin boundary, which can be used to imitate the behaviour of an unbounded region to a bounded domain like the convection boundary condition in heat flow problems. The periodic boundary joins one boundary to another making the potential values of each boundary the same. Finally the antiperiodic condition connects two boundaries similar to the periodic one but with opposite signs. The last two conditions are used to reduce the geometry of a problem using symmetry and therefore solution times (Figures 3.1 and 3.3).

3.3.4 Field analysis

3.3.4.1 Pre-processing

The pre-processing stage in FEMM is the interface where the model input data is captured (geometry, materials, etc.) as well as problem definition values: problem type, length units, current frequency, depth, solver precision, etc. The FEMM pre-processor has tools that facilitate assigning the problem geometry such as: drawing lines and curves, placing and connecting nodes, adding block labels, specifying boundary conditions on outer edges of the geometry, navigating with view manipulation tools, assigning a grid size, etc. In addition to simplifying the geometry setup of a model, FEMM is also able to import and export '.dxf' CAD files. Figure 3.1 shows the pre-processing stage for a cage induction motor as an example.

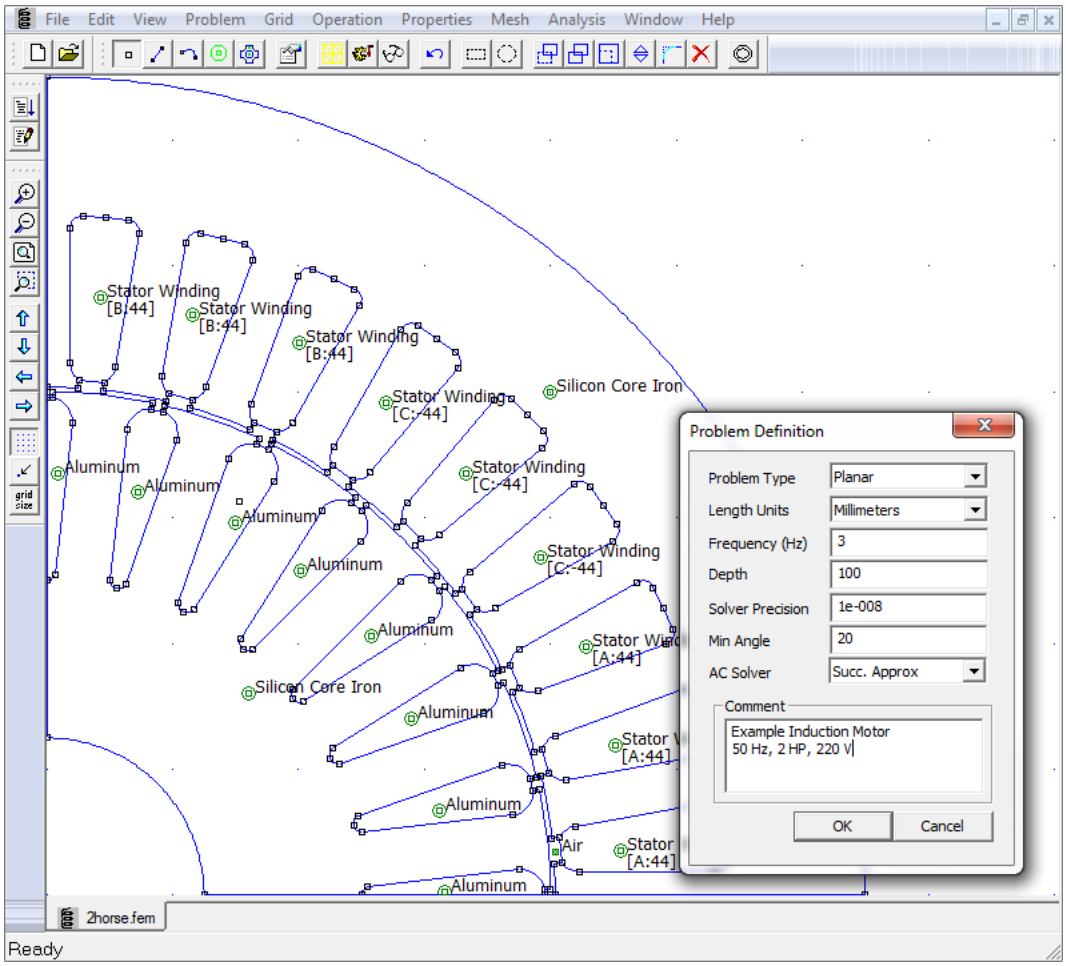

Figure 3.1 Magnetics pre-processing [62].

3.3.4.2 Processing

Once the input information of the problem is completed in the pre-processing stage, the generation of the system equations and the solution take place in the magnetics solver. The solver first calls the mesh generator to verify (or create) the mesh, and then solves the system of algebraic equations generated from the meshing. Although there is no need to directly execute the mesh generator because the mesh generator is called by the solver, it is a good practice to review the mesh before solving. The solution time depends on the size and complexity of the problem. The precision of the solver and the level of detail in the meshing influence the computing time as well. Broadly speaking, magnetostatic problems take less time to compute than steady-state time-harmonic problems; the latter uses complex numbers which doubles the number of unknowns compared to the same mesh under magnetostatic conditions.

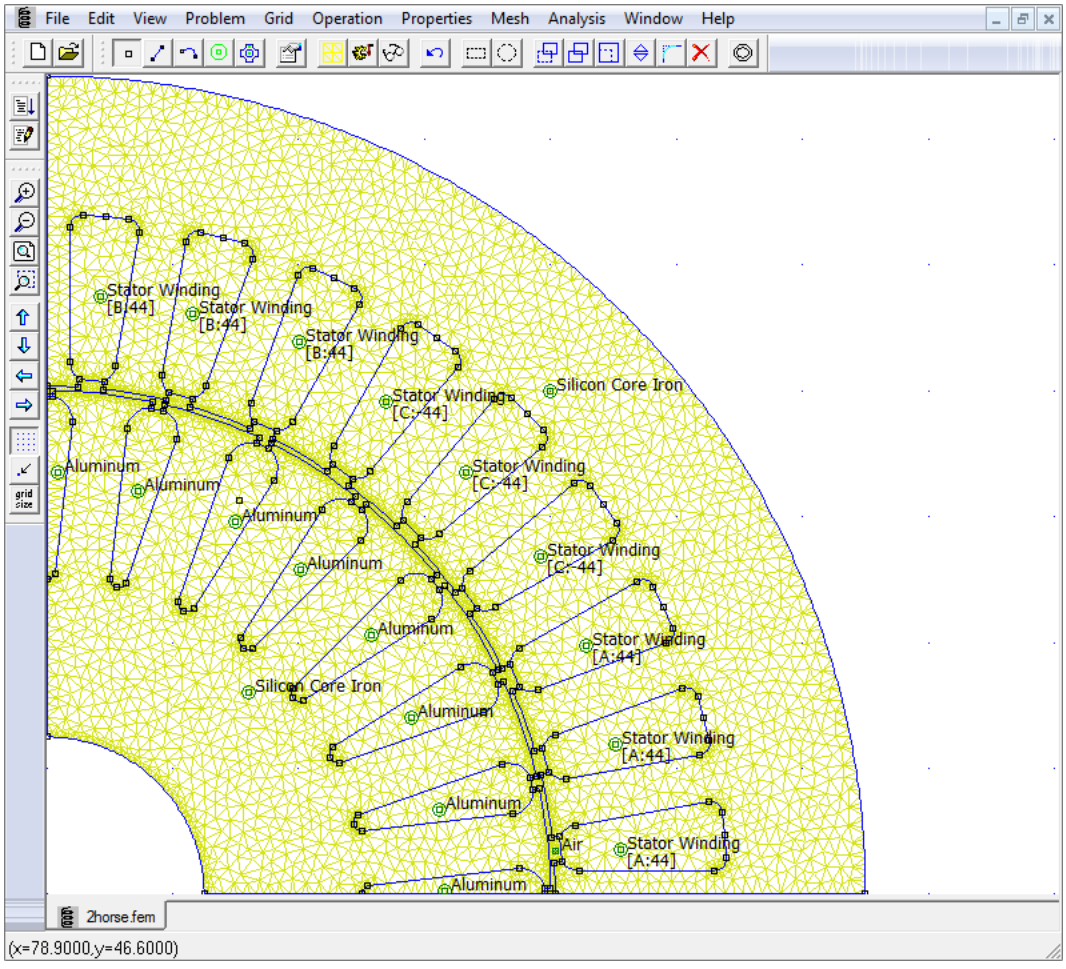

Figure 3.2 Magnetics processing [62].

3.3.4.3 Post-processing

In the post-processing stage the solution generated by the solver is displayed and the potential solution is used to calculate additional quantities such as: losses, eddy currents, etc. Common post-processor tasks include: drawing contours to perform certain operations, e.g. dot product; selecting blocks to calculate integrals, e.g. stored energy; plotting properties over a defined contour, vectors, density distribution; integrating line functions such as the total flux passing normal to a contour, the tangential field intensity along a contour, contour length, force from stress tensor, torque from stress tensor; integrating block functions such as mutual inductances, magnetic field energy, magnetic field co-energy, hysteresis, losses, total current, volume, force by weighted stress tensor, torque by weighted stress tensor, etc. Figure 3.3 shows the interface for the magnetics postprocessor.

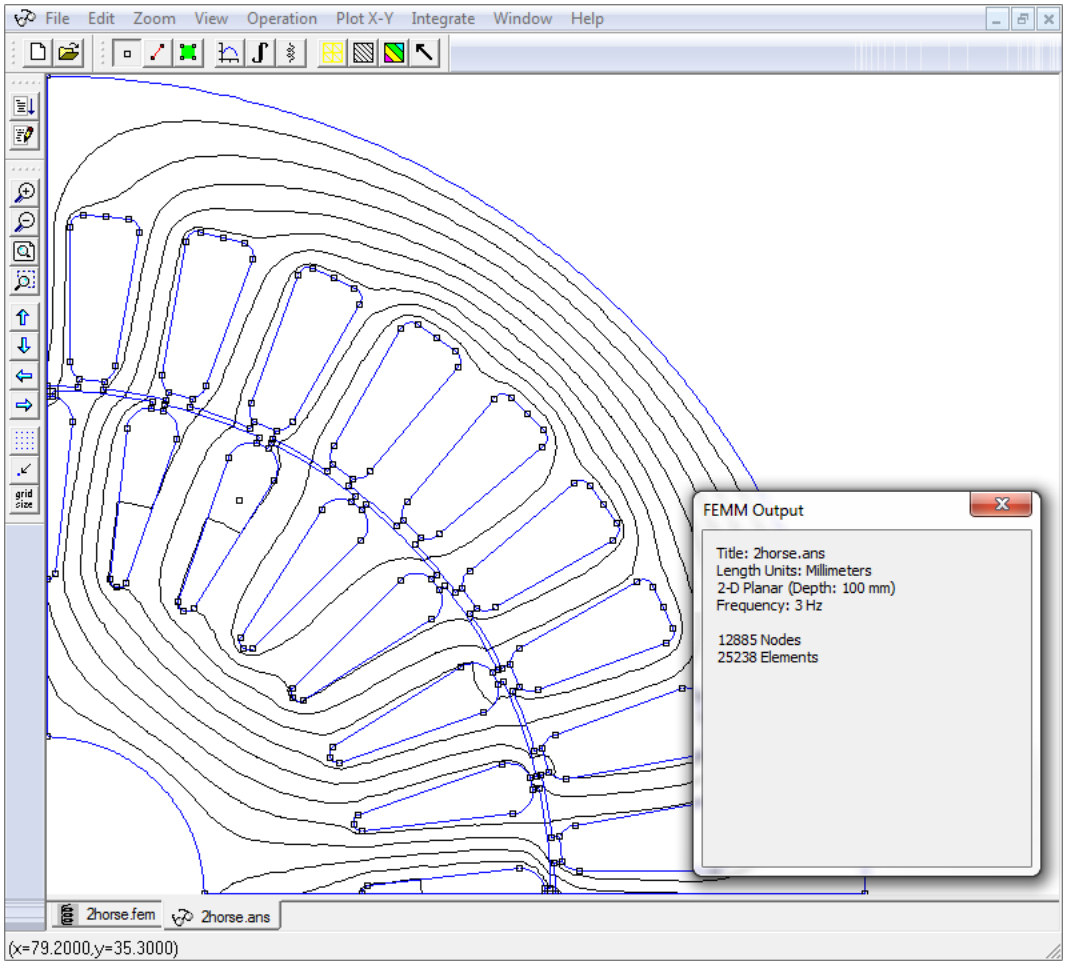

Figure 3.3 Magnetics post-processing [62].

3.3.4.4 Lua and OctaveFEMM

Lua is an embeddable scripting language that is capable of managing various machine resources; it was developed with the aim of being integrated in software written in C and other conventional languages such as: FORTRAN, Java, Smalltalk, Ada, C#, etc. Lua started in 1993 as an in-house language and is now in widespread use in many areas thanks to its attractive features: extensibility, it can be expanded through Lua and external code; simplicity, it is easy to learn with limited language; efficiency, it provides fast scripting; and portability, it is capable of running on several platforms with virtually the same code (Windows, Unix, PlayStation, Xbox, Mac OS-9, MS-DOS, IBM main-frames, among others). [63]

FEMM uses Lua code so that scripts programmed in Lua (typed in text editor software like notepad) can be executed in FEMM. The benefit of Lua scripting becomes significant when the problem requires the implementation of repetitive tasks. However, if more complex tasks are involved then the more practical option is to use OctaveFEMM, which is a matrix-oriented Matlab/Octave toolbox that allows implementing more sophisticated operations in FEMM via the Matlab/Octave functions [64].

Figure 3.4 shows a Lua script which retrieves the torque calculation at different frequencies for the 3-phase IM of Figure 3.1. Figure 3.5 illustrates an OctaveFEMM script which determines the operating point of a 3-phase transformer.

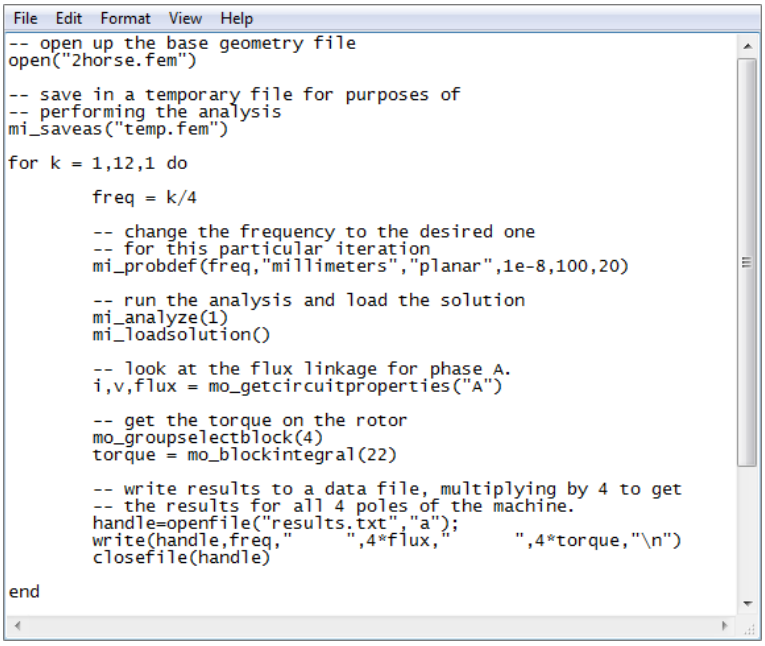

Figure 3.4 Lua scripting [62].

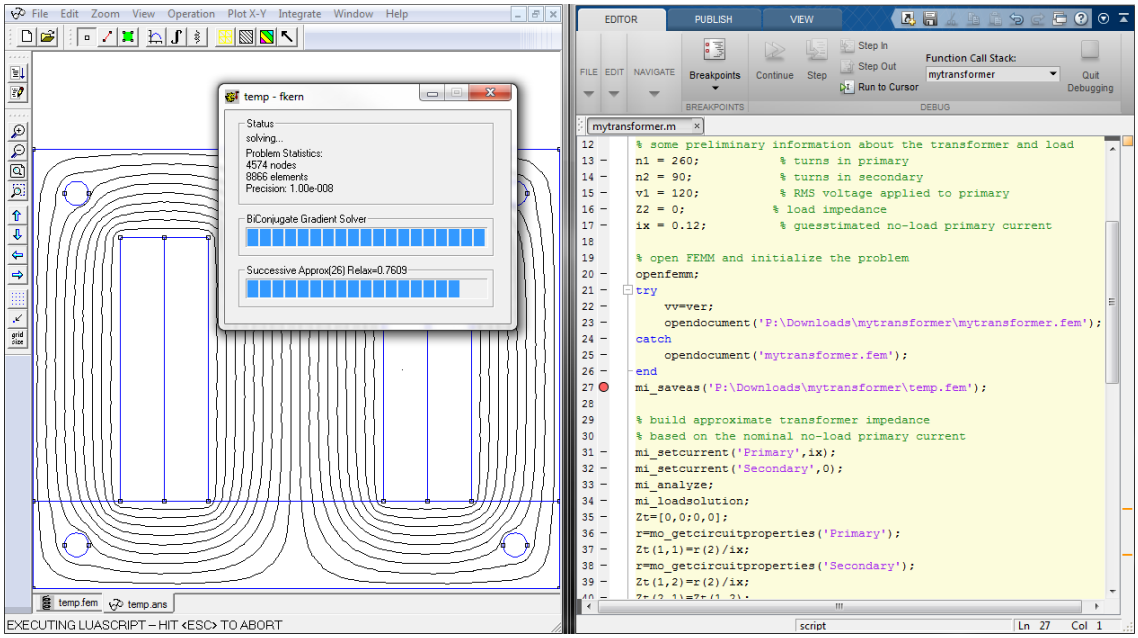

Figure 3.5 OctaveFEMM Matlab script communicating with FEMM [64].

3.4 High-speed induction motor modelling

3.4.1 Introduction

The IM modelled in this thesis is a 4-pole three-phase canned-rotor motor. The rotor has a continuous smooth copper can placed on the outer surface of the iron rotor core. The complete geometry of the IM can be seen in appendix A, along with some additional information. In order to save processing time the IM geometry is simplified using symmetry, in this case the geometry can be reduced to one quarter of the circumference as shown in Figure 3.6.

In the previous section, it was mentioned that FEMM did not have a way of specifying rotor movement directly, which presents an obstacle in modelling IMs. Fortunately there are ways to simulate rotor motion in an IM which are explained in section 3.4.2. Another consideration that has to be taken into account in modelling IMs in FEMM is the winding input source. As pointed out in section 3.3.2, the FEMM input source is a current source (constant current operation) but similar to rotor motion, it is also possible to modify the input source to a voltage source (constant voltage operation).

The different methods for modelling rotor motion in section 3.4.2 are implemented in section 3.4.3 using a current source. With the voltage source only the slip conductivity approach is used, so there are three operating conditions for which the HSIM is analysed: slip frequency rotor simulation using a constant current source; slip conductivity, with a constant voltage source; and slip conductivity, with a constant voltage source.

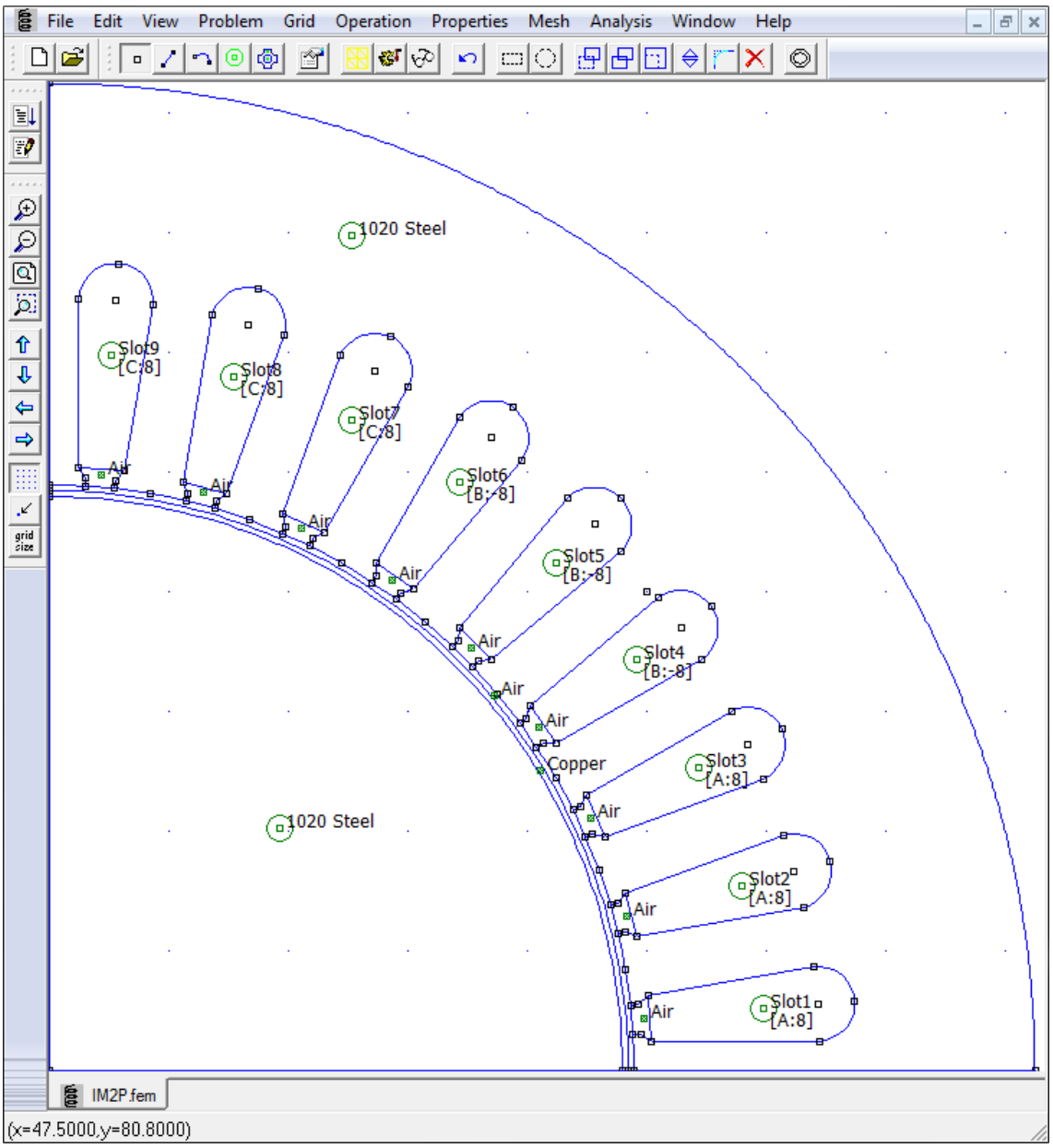

Figure 3.6 Simplified geometry of the three-phase induction motor.

3.4.2 Modelling rotor motion

3.4.2.1 Overview

There are two possible approaches for simulating rotor motion in FEMM. In both of them the rotor can is rotating under steady state conditions. In the first approach (slip frequency [62]) rotor motion is modelled by varying the frequency at which the eddy currents in the rotor can and core of the HSIM are induced (or rotor bars for a squirrel-cage IM). This represents the electrical condition in the rotor when the IM is running under steady state conditions. In the second approach (slip conductivity) the rotor can resistance of the IM is modified by varying the electrical conductivity of the can material to create a similar effect as the slip frequency approach. Figure 3.7 shows the basic per-phase IM steady state equivalent circuit.

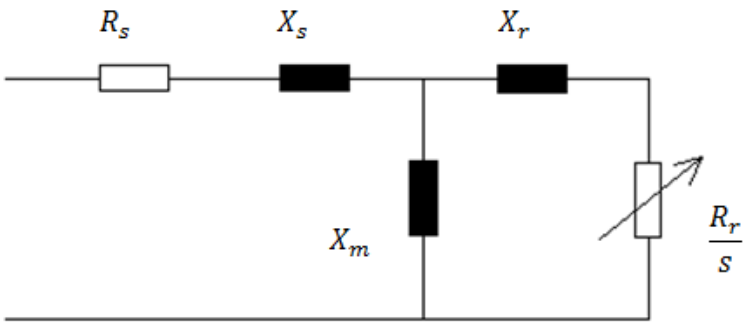

Figure 3.7 Per phase equivalent circuit of an induction machine.

3.4.2.2 Slip frequency approach

The slip frequency approach used to simulate rotor motion is based on the relationship between synchronous speed, rotor speed, stator frequency and slip as follows:

$$\omega_s = \omega - p\omega_r \tag{3.12}$$

Where:

$$\omega_s = s\omega \tag{3.13}$$

ω_s is the slip frequency, ω the electrical frequency, s the slip, p the pair poles and ω_r the mechanical rotor speed.

Because the rotor does not move in FEMM, it remains stationary ω_r=0 and the slip frequency ω_s is the angular stator frequency ω_s=ω. Varying the problem frequency in FEMM from 0 to the stator frequency ω_s means that the magnetic fields rotate at slip frequency with slip varying from 0 to 1. Therefore synchronous speed is achieved when the input frequency is 0 (magnetostatic conditions); and locked rotor condition when the input frequency is the supply frequency (s=1).

The slip frequency approach only requires changing the input frequency. A lua script can easily manage the collection of data throughout the IM slip domain. Figure 3.8 illustrates a flowchart for the slip frequency approach and Table 3.1 shows the relationship between the slip and the problem frequency, and the torque, losses, etc.

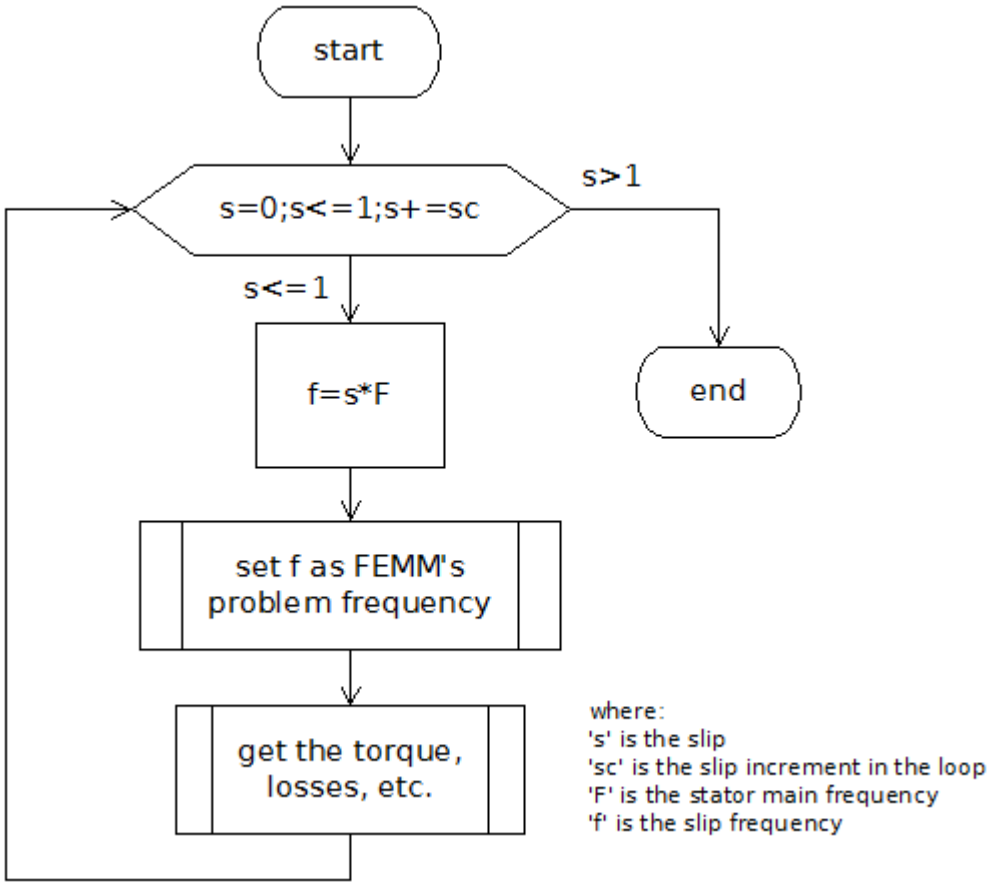

Figure 3.8 Flowchart of the slip frequency approach.

Slip	**Slip frequency ω_s (FEMM's problem frequency input)**	**Torque (or other quantity: losses, etc.)**
0	0	T_0
f_1/F	f_1	T_1
f_2/F	f_2	T_2
. . .	. . .	. . .
1	F	T_n

Table 3.1 Relationship between torque (and or any other quantity) and slip in FEMM.

3.4.2.3 Slip conductivity approach

Rotor motion in the slip conductivity approach is modelled in a similar way to the slip frequency method. The rotor can resistance varies as the slip varies under normal operating conditions at fixed supply frequency.

As can be seen from Figure 3.7 the steady-state speed of an IM is directly related to:

$$\frac{R_r}{s} \tag{3.14}$$

Where R_r is the rotor resistance and s the slip

The method of modifying the rotor can resistance is via its electrical conductivity. From Figure 3.9 the resistance of the rotor can is given by:

$$R_r = \frac{l}{\sigma A} \tag{3.15}$$

From eqn. 3.14 and eqn. 3.15, we get:

$$\frac{R_r}{s} = \frac{l}{s\sigma A} \tag{3.16}$$

Or:

$$\frac{R_r}{s} = \frac{l}{\sigma' A} \tag{3.17}$$

With:

$$\sigma' = s\sigma \tag{3.18}$$

Where l is the length of the can, A the cross sectional area, σ the electrical conductivity, σ' the equivalent conductivity and s the slip.

As shown in eqns. 3.17 and 3.18, the slip conductivity approach only requires changing the electrical conductivity of the rotor can material over an appropriate range. Again a lua script can easily manage the data collection throughout the variation in the rotor resistance for constant input frequency (motor stator frequency). Figure 3.10 illustrates the flowchart for the slip conductivity approach and Table 3.2 shows the relationship between the slip and the rotor can conductivity, and the torque, losses, etc. Additionally, Table 3.3 summarises the slip frequency and conductivity approaches, where: in the first approach the problem frequency is varied with constant rotor can conductivity, and in the second approach the rotor can conductivity is varied with a constant supply frequency.

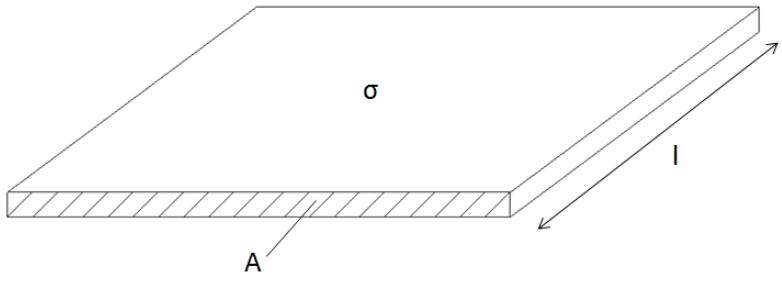

Figure 3.9 Rotor can.

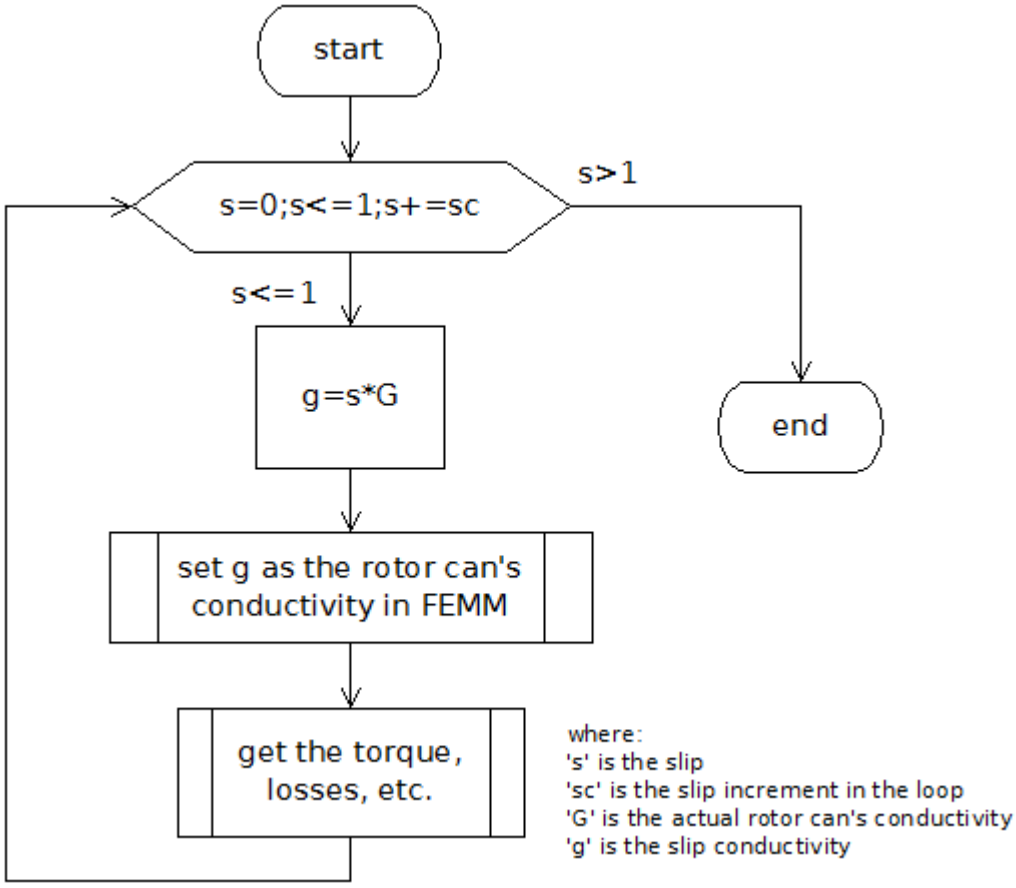

Figure 3.10 Flowchart of the slip conductivity approach.

Slip	**Slip conductivity σ' (FEMM's rotor can conductivity input)**	**Torque (or other quantity: losses, etc.)**
0	0	T_0
σ_1'/σ	σ_1'	T_1
σ_2'/σ	σ_2'	T_2
. . .	. . .	. . .
1	σ	T_n

Table 3.2 General procedure to obtain the values of torque and slip in FEMM for a range of slips; σ is the actual rotor conductivity.

Variable	**Method**	
	Slip frequency ω_s=s*f	Slip conductivity σ'=s*σ
f	(var) 0…f_{stator}	(cst) f_{stator}
σ	(cst) σ_{can}	(var) 0…σ_{can}

Table 3.3 Comparison between the slip frequency and slip conductivity approaches in FEMM.

3.4.3 Stator winding input

3.4.3.1 Overview

The analysis of an IM under constant current might sound strange because the 3-phase supply provides a constant voltage source. The reason comes from the way in which FEMM addresses the relevant partial differential equations in magnetics (section 3.3.2) using a current source. If FEMM had the option of solving problems using the voltage as input, then constant current operation would not be necessary. Nonetheless, it is possible to approximate constant voltage operation (section 3.4.3), but it requires an understanding of constant current operation. Furthermore the comparison of energy-related quantities (such as losses, mechanical power developed, etc.) between the slip frequency and slip conductivity approaches is better visualized using the constant current source.

3.4.3.2 Constant current operation

In the constant current operation, the 3-phase stator winding current remains constant throughout the entire slip domain. The flowchart of Figure 3.11 illustrates the simplicity of this operating regime.

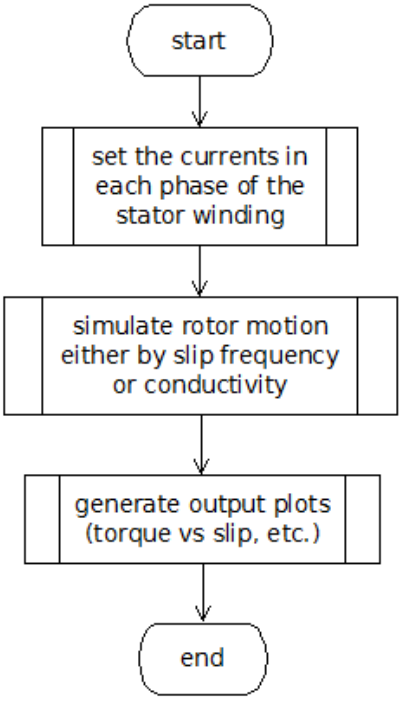

Figure 3.11 Flowchart of IM operation under constant current regime.

Following the flowcharts of Figures 3.8, 3.10, 3.11 and establishing a constant excitation current of 20 (A) in the stator winding the HSIM results obtained are shown in Figures 3.12 - 3.15. As expected the input current is constant across the slip range, Figure 3.12. For both approaches, slip frequency and conductivity, denoted as 'sF' and 'sG' respectively, the torque via weighed stress tensor is practically the same which means both approaches are correctly modelling the fields around the air gap. However, for the per-phase voltage across the winding and the can losses there is a discrepancy between the two approaches, particularly at slip values close to 0. For slip values close to 1, the error reduces (Figures 3.14 and 3.15). This has to do with the conditions under which each method operates: in the slip frequency approach the induced voltage in the rotor can depends on a slip-dependant frequency that varies the voltage from a minimum at slip 0 to a maximum at slip 1; and for the slip conductivity approach the can induced voltage depends on a fixed frequency that causes the voltage going from a maximum value at slip 0 to a minimum at slip 1. At slip 1 both approaches have the same value. A detailed explanation of the relationship of the slip frequency and conductivity approaches regarding voltage and losses can be found in appendix B.

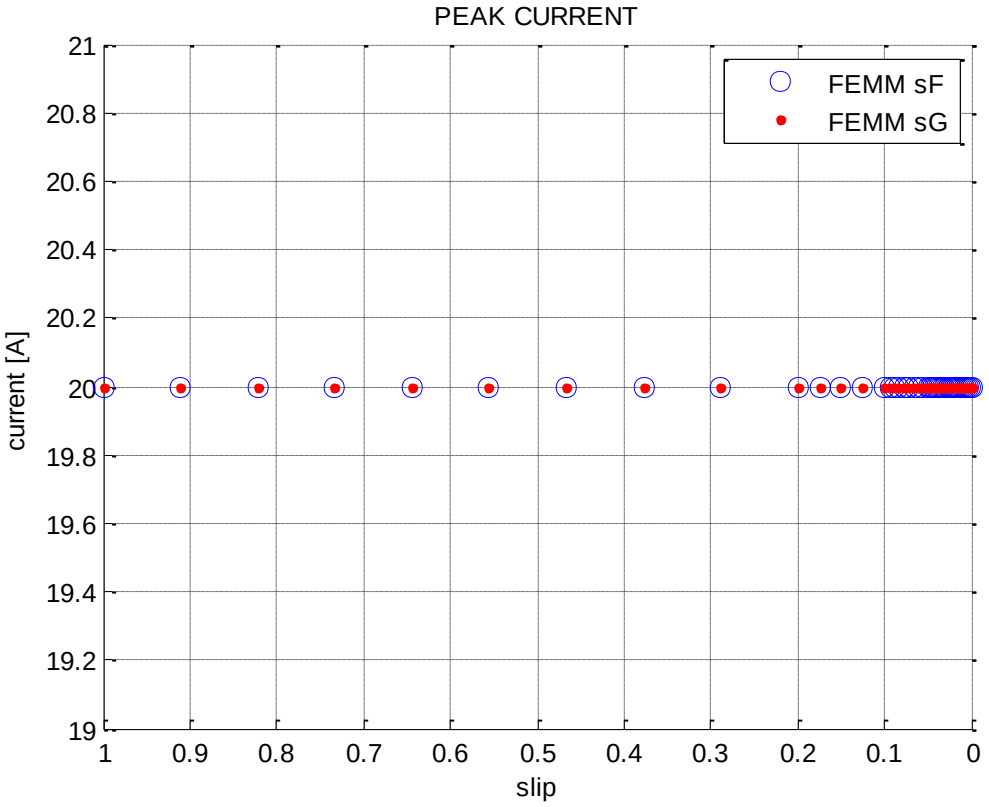

Figure 3.12 Peak stator current per phase.

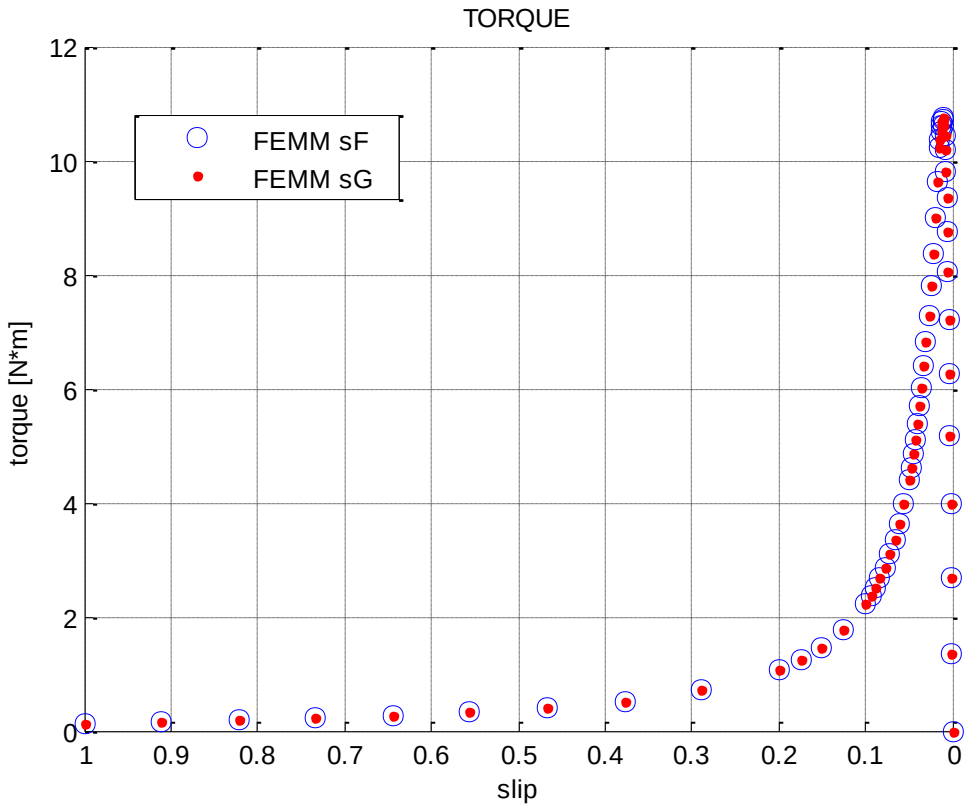

Figure 3.13 Torque developed.

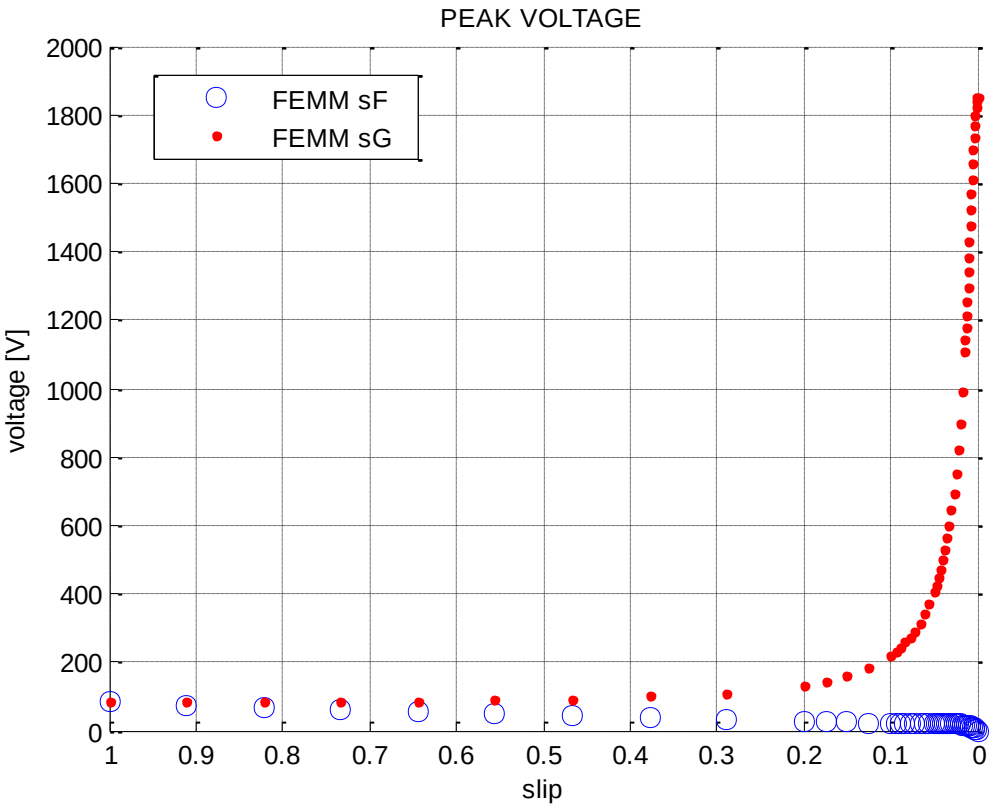

Figure 3.14 Peak stator voltage per phase.

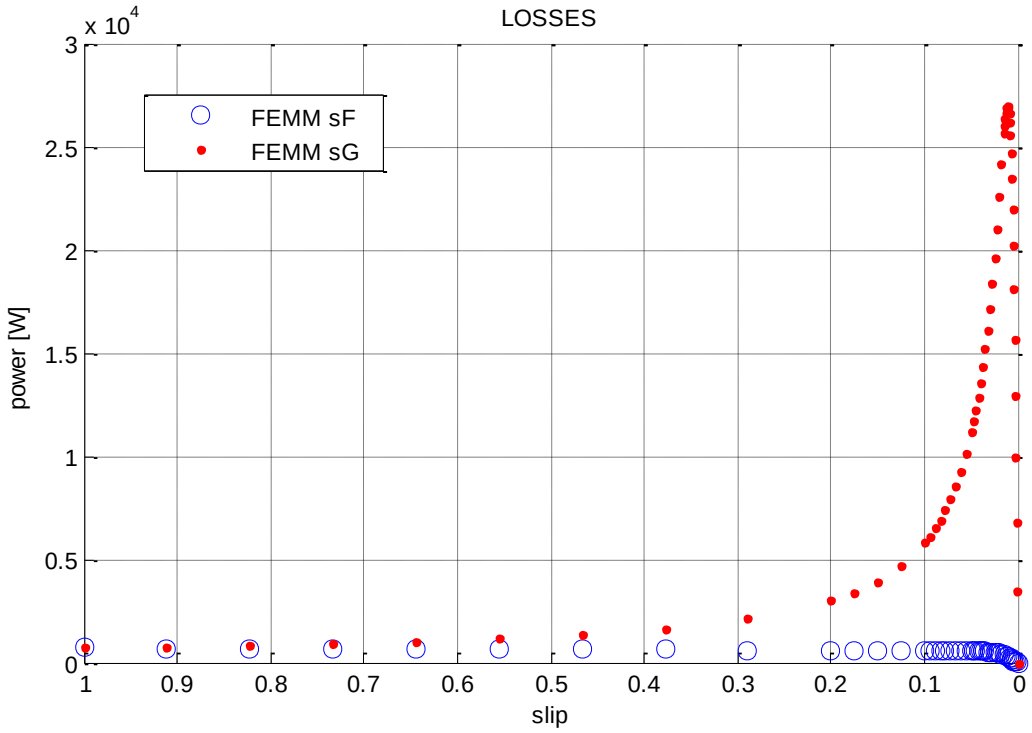

Figure 3.15 Rotor can losses.

3.4.3.3 Constant voltage operation

In section 3.2.4.2 different strategies for FE computer modelling of electric machines were discussed. To model constant voltage operation in FEMM, one can either extract the values of the equivalent circuit elements (inductances, resistances, etc.) under constant current conditions, and then solve the equivalent circuit for constant voltage operation as in [62], or perform an FE analysis by making FEMM vary the current at any slip in an iterative process until the target voltage value is reached. In this thesis, the second method to simulate constant voltage is used.

As illustrated in Figure 3.14, the effect of using constant current in the stator windings is a variable winding voltage across the slip range. To model the HSIM under constant voltage conditions, it is necessary to find the current at which the voltage of the stator winding equals the required voltage across the slip range. Determining the correct value of the current to obtain the target voltage can be done using a numerical iterative method; in this case the bisection method was implemented. An initial current is set in the winding and the corresponding voltage across terminals determined; if the voltage does not meet the error criterion, then it iterates the current until the error between the measured and desired voltage reaches its target. In the modelling of constant voltage only the slip conductivity approach is of practical use, because in the slip frequency approach the voltage in the stator winding decreases to zero as the slip decreases to zero which is not what happens in practice. There is always voltage (constant) on the other hand, across the stator terminals in the slip conductivity approach. The flowchart of Figures 3.16 and 3.17 illustrates the solution procedure to obtain constant voltage in the IM stator.

The HSIM results (‘sG’ denotes slip conductivity) in Figures 3.18 - 3.21 use a reference of 170 V for the stator peak voltage with a convergence error of 2% and the flowchart procedure in Figures 3.16 and 3.17. The effect of the convergence error over the constant voltage operation is illustrated in Figure 3.18. A lower convergence error leads to a smoother voltage close to the desired value, but increases the processing times. The current, torque and rotor can losses, however, are reasonably constant as can be seen in Figures 3.20 and 3.21 respectively.

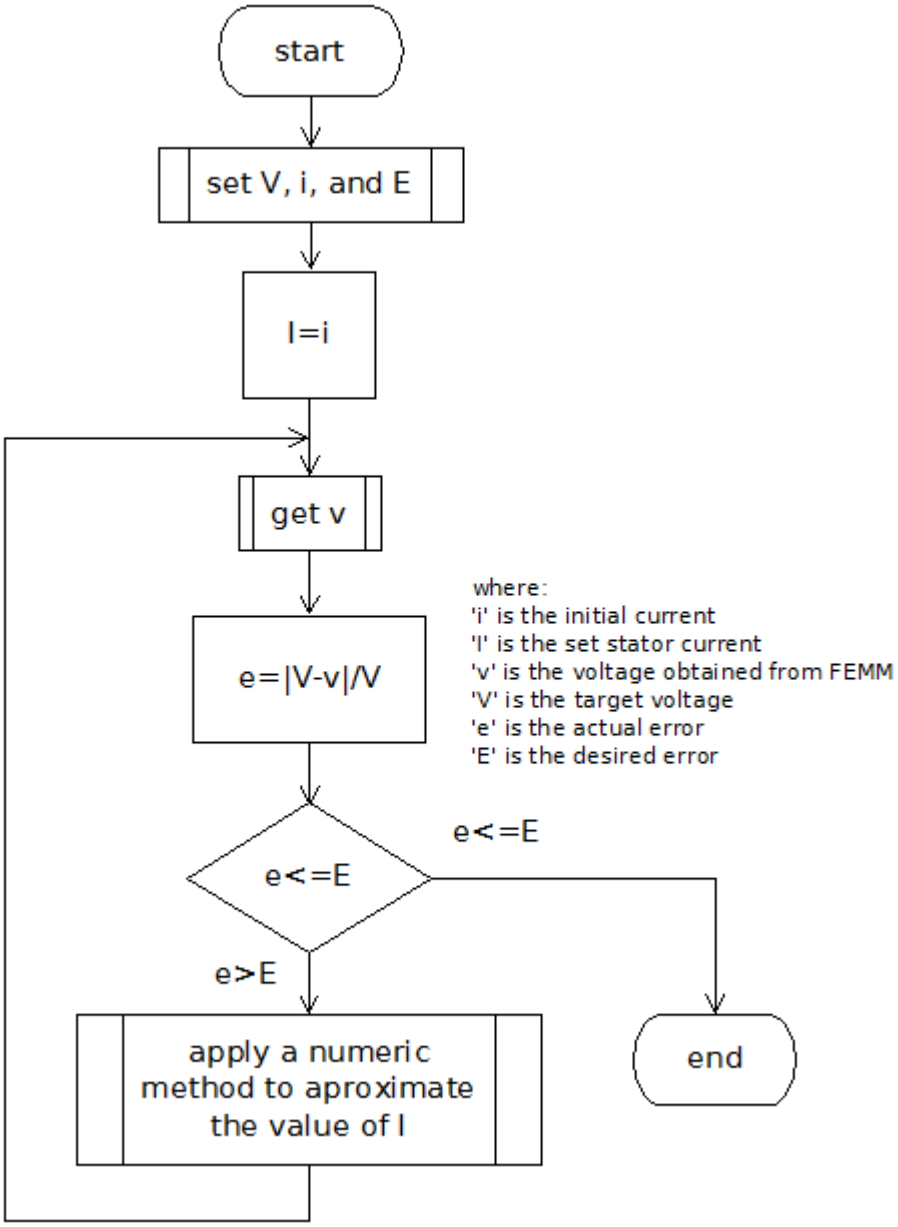

Figure 3.16 Iterative subroutine for the error bound for the voltage operation.

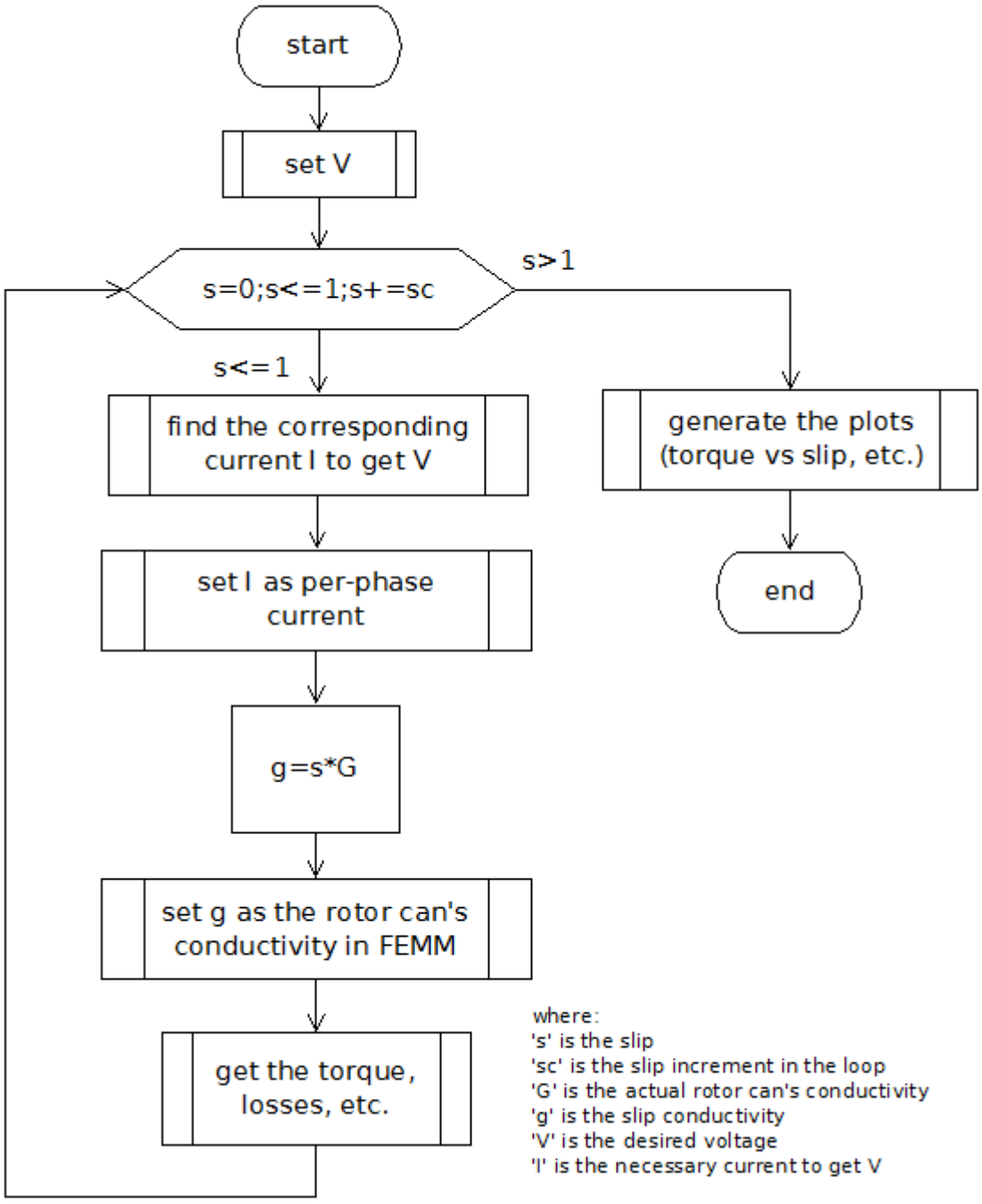

Figure 3.17 Flowchart of constant voltage operation.

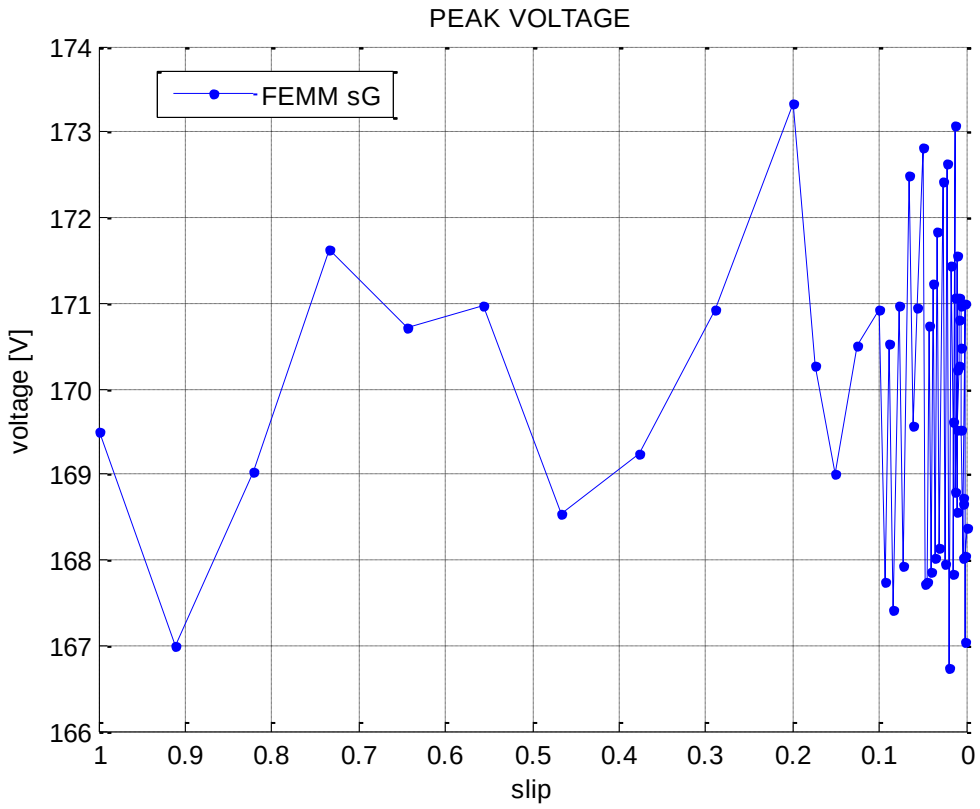

Figure 3.18 Peak stator voltage per phase.

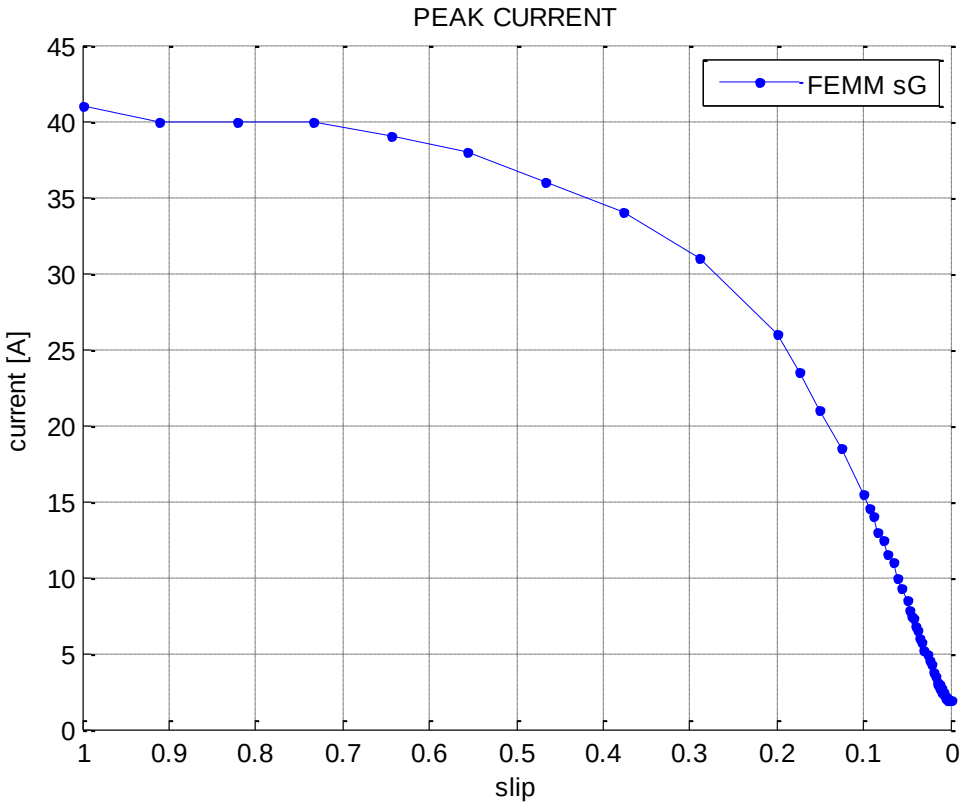

Figure 3.19 Peak stator current per phase.

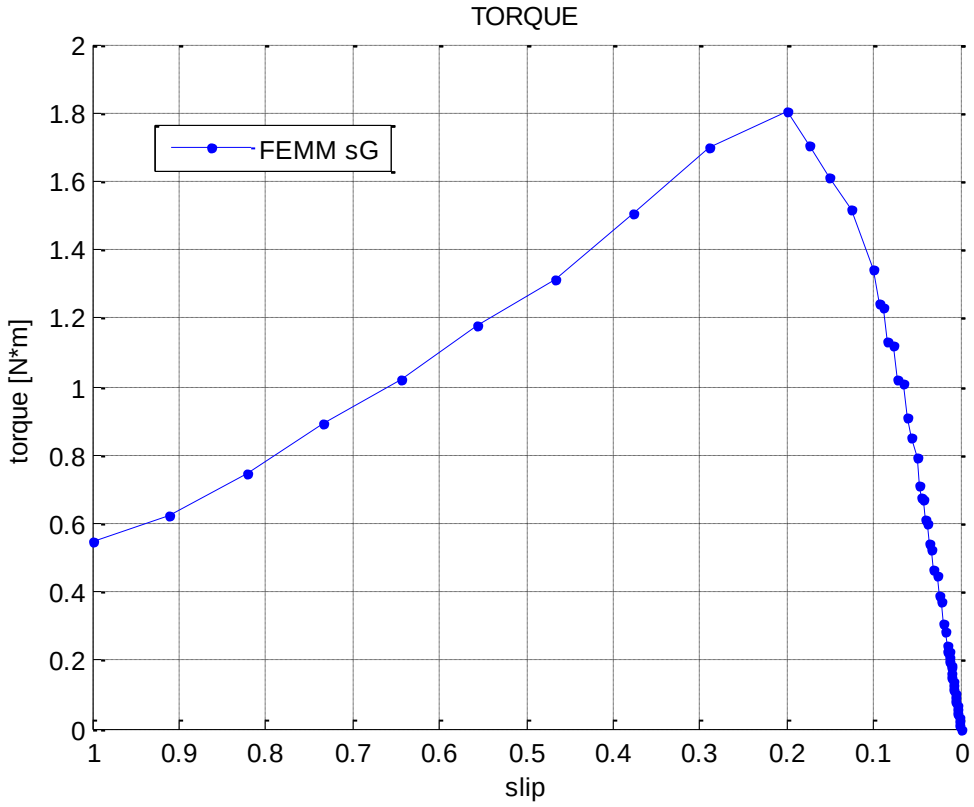

Figure 3.20 Torque developed.

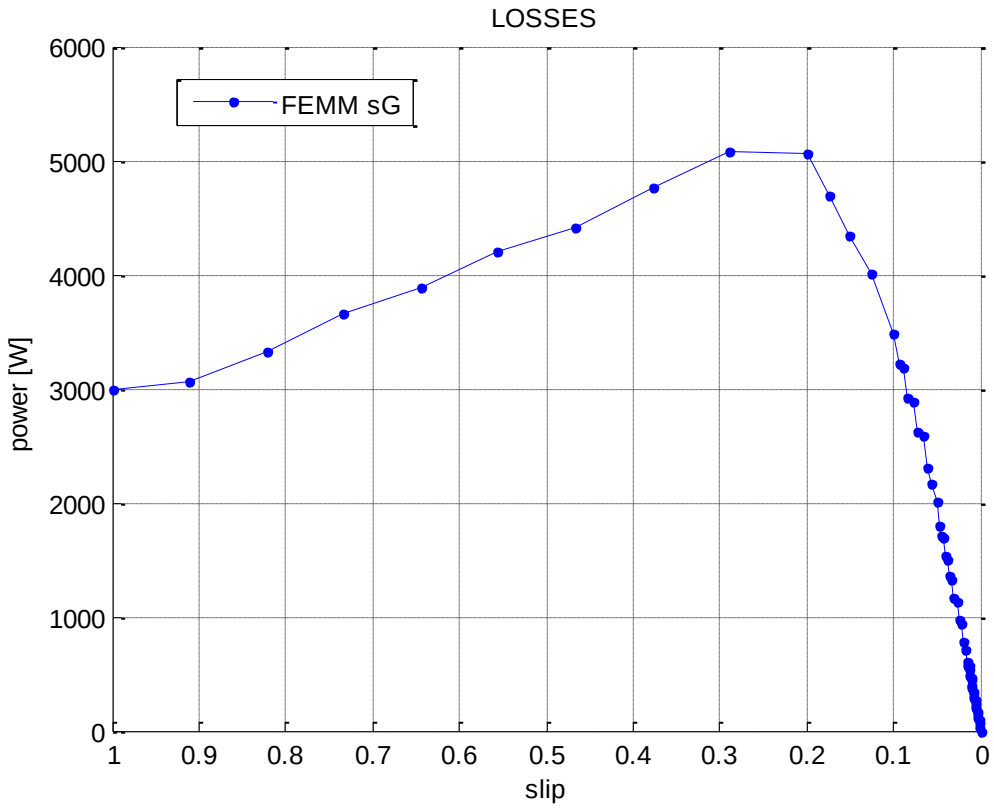

Figure 3.21 Rotor can losses.

3.5 Summary

The finite element modelling is based on obtaining approximate solutions to the governing partial differential equations. The development of the FEM provided a new range of capabilities in numerical analysis by overcoming the limitations of its predecessor, the finite difference method (FDM). The FDM lacked the versatility FE possesses, because its approach is better suited to problems that can be approximated by rectangular boundary geometries. The FEM is usually carried out by meshing a model with triangular elements, which is particularly good for cylindrical problems with circular geometries; this normally provides more accurate results, where in general, reducing the size of the triangular elements around a boundary improves the solution but increases the processing time. Although the FEM was originally conceived to analyse stresses in complex air-frame structures, it has become widely used in a diverse range of physical problems including electrical machine analysis.

In this thesis, FE modelling of an HSIM is performed using FEMM. Electrical machine simulation using FEMM differs from other software packages in the lack of specialized modules for electrical motors, because FEMM is targeted at generic magnetics problems. However, there are ways to overcome the limitations of FEMM including rotor motion and constant voltage operation; both of them discussed in this chapter. The FEMM results were obtained using three approaches: slip frequency, constant current; slip conductivity, constant current; and slip conductivity, constant voltage.

Chapter 4

Analytical Modelling

4.1 Overview

Before FE modelling in the analysis of IMs became generally available, the method for determining the performance of IMs was done with the aid of classical circle diagrams using phasors. The accuracy of the method, however, deviated from the measured performance and an analytical method emerged in the 1950's as a better alternative in predicting the performance of IMs.

This chapter presents the analysis of an HSIM implementing the multi-layer analytical model. The background and theory of the analytical model will be described and then the general methodology required for modelling IMs. The last sub-chapter analyses the HSIM model using the MLM.

4.2 History

The MLM is an analytical method developed between the 1950's and 1970's; it was presented as a better alternative for analysing IMs. The model was proposed by Mishkin [65] as a more accurate way to determine the stator current and torque of cage IMs. These were calculated traditionally using a classical circle diagram that assumed constant leakage inductance. In reality the leakage inductance varied with the rotor slip. Since Mishkin's model was directly derived from Maxwell's field equations, the model did not require the assumption of constant leakage inductance against slip. However, it did simplify some of the fine detail in the construction in the machine. The teeth and slotted

areas for example were replaced with anisotropic magnetic masses with equivalent permeabilities. In this model the stator current and torque were calculated as functions of slip in a unified analytical solution. Mishkin's model improved the calculations in IMs; however, the results were still subject to errors to the measured performance.

Following Mishkin, however, the layer method continued improving. An important contribution to the method was made by Cullen and Barton [66] introducing the wave impedance concept, which included the ability to simulate the effects of tooth-top and zigzag leakage fluxes but neglected end effects. The model not only simplified Mishkin's version but also brought better results. Cullen and Barton's wave impedance came from the similarity between the MLM's resultant field equations and transmission line equations. The possibility of relating field quantities with circuit parameters led to the opportunity of regarding the problem as an approximate solution to the actual field problem, if viewed from a circuit perspective or as the exact solution of an idealized problem, if viewed from a field perspective.

Independently from the MLM development, Pipes [67] presented a mathematical technique that simplified the calculation of electromagnetic fields in conducting metal plates produced by an external alternating magnetic field. Greig and Freeman [68] implemented Pipe's technique in the MLM and with it they established the 'formal' matrix MLM methodology to calculate the field values in the model. Before Greig and Freeman, the use of the MLM was limited to four layers due to the algebraic limitations of the existing theory. Greig and Freeman's contribution overcame such limitations by simplifying the implementation of the MLM, which could now be solved for any number of layers without increasing the complexity of the solution.

Freeman [69] incorporated Cullen and Barton's wave impedance concept into the MLM. The integration of the surface impedance simplified the method by enabling the transfer of the impedances throughout the multi-layer region instead of the fields. Each region of the model could be conveniently represented as a T-equivalent circuit and the whole model was able to be solved as an equivalent circuit whilst maintaining the properties of any particular layer independently from the others.

Some years later Williamson [70] presented a comprehensive paper in which the MLM's capabilities were extended. Now the model permitted the presence of anisotropy in the rotor and stator without the introduction of additional assumptions. This provided the necessary means to explore and investigate new configurations of linear motors, particularly transverse flux types.

The MLM has been used by a number of authors for the exploration and design of linear and cylindrical IMs. Williamson and Smith [71] included the effects of the rotor skew and slot leakage in the analysis of IMs and modelled the rotor current considering its discrete nature. They also used the MLM as a routine design optimisation tool for permanent-magnet eddy current couplings [14]. Peralta [72] developed a methodology to analyse canned line-start PM motors. Chalmers and Hamdi [15] analysed and explore a new composite-rotor IM prototype. Cox [73] designed a novel linear machine which was cheap and easy to mass-produce. In the field of HSIM, the MLM has served to analyse the electromagnetics of HSIMs as the work of Pyrhönen [6] and Huppunen [4] shows.

4.3 Theory

4.3.1 Introduction

There are different versions of the MLM, the one used in this thesis is the original method developed by Greig and Freeman [68] with some modifications (shown in the methodology). The theory and methodology of the MLM are presented in the following section. Similar to the FE modelling, displacement currents in the analytical model are neglected and end effects are not taken into account.

4.3.2 Model formulation

An IM can be simulated using the MLM once its geometry is represented as an adequate layer model (see Figure 4.1). For the case of LIMs and SRIMs the approximation is accurate and straightforward. Knowing the input current or field levels, the MLM can

determine the field distribution of the IM in every layer. Figure 4.2 shows the generic multi-region.

The MLM comes from the abstraction of an electromagnetic problem into an equivalent multi-region model, which consists of homogeneous layers of infinite longitudinal extent (the *x* direction of Figure 4.1) that are subject to the influence of electromagnetic travelling waves. Flux densities and magnetising forces are distributed through the multi-region model. Each layer has a certain thickness, permeability, conductivity and velocity. Taking Figure 4.1 as reference, the travelling wave problem is addressed from the general case in which a current sheet lies between two layers. The aim is to determine the field distribution in all the layers (from 1 to *N*). The stationary reference frame of the travelling field is used so that its velocity is ω/k (m/s), where ω is the synchronous frequency and k is the wave number. For a layer n in which the angular frequency is $\omega_n=s_n\omega$, its velocity relative to the stationary frame results in $(1-s_n)\omega/k$ (m/s) (see appendix C). If the field values are known, the power loss and forces acting on any region can be calculated. A more detailed view of a layer is shown in Figure 4.2. This general region has a given resistivity ρ_n and relative permeability μ_n and is surrounded above and below by neighbouring layers. The boundary upper and lower fields for the *n-th* layer are, B_n, H_n and B_{n-1}, H_{n-1} respectively.

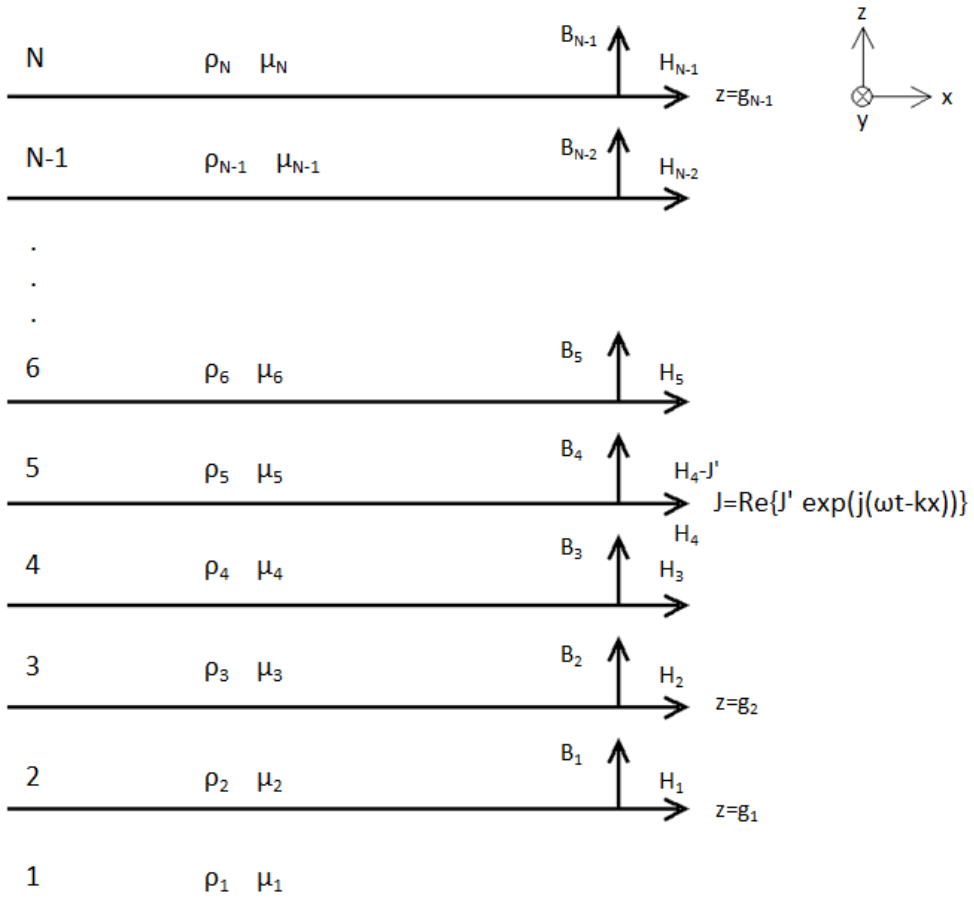

Figure 4.1 Multi-layer model [68].

The excitation to the model is an infinitely thin current sheet, *Re{J'exp(j(kω$_n$t-kx))}*, which lies between two regions (layers 4 and 5 in Figure 4.1); it varies sinusoidally in time and space along the *x* direction. Alternatively, it is also possible to solve the model assuming field levels ([4], [15]), and then match the current for a given machine performance. In this thesis, however, a current sheet is taken as the input to the model in order to make the simulation of the motor as practical as possible.

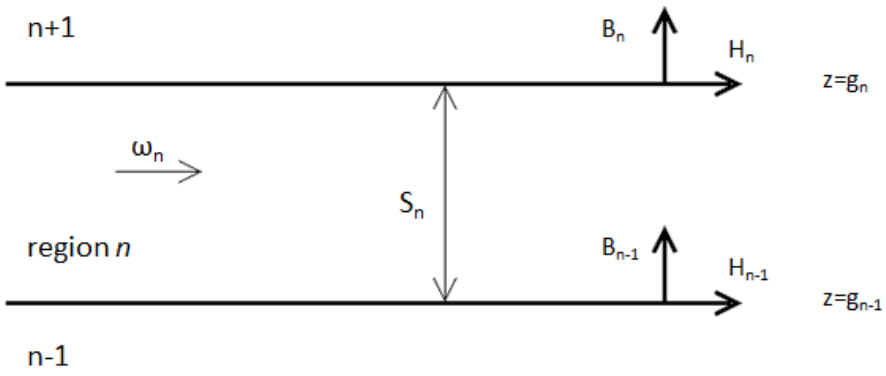

Figure 4.2 General layer of the model [68].

4.3.3 Boundary conditions

The boundary conditions for the MLM are as follows: [68]

(a) B_n is continuous across a boundary.

(b) All field components disappear at $z=\pm\infty$.

(c) If a current sheet exists between two regions, then $H_n=H_{n-1}-J'$, where H_n is the magnetic field strength immediately above the current sheet and H_{n-1} is the magnetic field strength immediately below the current sheet.

4.3.4 General equations

The upper and lower fields in a general region of Figure 4.2 must obey the laws of electromagnetism described by Maxwell's equations:

$$\nabla \cdot B = 0 \tag{4.1}$$

$$\nabla \cdot J = 0 \tag{4.2}$$

$$\nabla \times E = -\frac{\partial B}{\partial t} \tag{4.3}$$

$$\nabla \times H = J \tag{4.4}$$

And additionally:

$$B = \mu H \tag{4.5}$$

$$J = \sigma E \tag{4.6}$$

Applying Maxwell's equations in the general layer, the following differential equation is obtained:

$$\frac{\partial^2 H_z}{\partial z} - \alpha^2 H_z = 0 \tag{4.7}$$

For the general layer of Figure 4.2, α is:

$$\alpha^2 = k^2 + j\sigma\mu_n\omega_n \tag{4.8}$$

The general solution to eqn. 4.8 is:

$$H_z = C_1 e^{\alpha z} + C_2 e^{-\alpha z} \tag{4.9}$$

Hyperbolic functions can be used to simplify arithmetic manipulation and eqn. 4.9 becomes:

$$H_z = C_A \cosh(\alpha z) + C_B \sinh(\alpha z) \tag{4.10}$$

The upper boundary fields in the general layer can be obtained as function of the lower boundary fields. If $B_z=B_{n-1}$ and $H_x=H_{n-1}$ when $z=0$ and $B_z=B_n$ and $H_x=H_n$ when $z=S_n$, then by combining eqns. 4.10 and 4.5 the fields can be expressed as follows:

$$B_n = B_{n-1}\cosh(\alpha_n S_n) + \frac{1}{\beta_n} H_{n-1}\sinh(\alpha_n S_n) \tag{4.11}$$

$$H_n = \beta_n B_{n-1}\sinh(\alpha_n S_n) + H_{n-1}\cosh(\alpha_n S_n) \tag{4.12}$$

or in transfer matrix form: [68]

$$\begin{bmatrix} B_n \\ H_n \end{bmatrix} = [T_n] \begin{bmatrix} B_{n-1} \\ H_{n-1} \end{bmatrix} \tag{4.13}$$

And:

$$\begin{bmatrix} B_{n-1} \\ H_{n-1} \end{bmatrix} = [T_n]^{-1} \begin{bmatrix} B_n \\ H_n \end{bmatrix} \tag{4.14}$$

Where:

$$[T_n] = \begin{bmatrix} \cosh(\alpha_n S_n) & \frac{1}{\beta_n}\sinh(\alpha_n S_n) \\ \beta_n \sinh(\alpha_n S_n) & \cosh(\alpha_n S_n) \end{bmatrix} \tag{4.15}$$

$$[T_n]^{-1} = \begin{bmatrix} -\cosh(\alpha_n S_n) & \frac{1}{\beta_n}\sinh(\alpha_n S_n) \\ \beta_n \sinh(\alpha_n S_n) & -\cosh(\alpha_n S_n) \end{bmatrix} \tag{4.16}$$

$$\beta_n = \frac{\alpha_n}{jk\mu_n} \tag{4.17}$$

The transfer matrix T_n allows the calculation of the field distribution in any layer by simply multiplying the corresponding transfer matrices of the regions involved. The calculation of the fields, bearing in mind boundary conditions (b) and (c) can be summarised as follows: [68]

$$\begin{bmatrix} B_{N-1} \\ H_{N-1} \end{bmatrix} = [T_{N-1}][T_{N-2}]..[T_{r+1}] \begin{bmatrix} B_r \\ H_r - J' \end{bmatrix} \tag{4.18}$$

$$\begin{bmatrix} B_r \\ H_r \end{bmatrix} = [T_r][T_{r-1}]..[T_2] \begin{bmatrix} B_1 \\ H_1 \end{bmatrix} \tag{4.19}$$

Where H_{N-1} and H_1 are the boundary fields of the top and bottom regions respectively:

$$H_{N-1} = -\beta_N B_{N-1} \tag{4.20}$$

$$H_1 = \beta_1 B_1 \tag{4.21}$$

4.3.5 Power and force

According to the Poynting's theorem [74] electromagnetic wave energy can be quantified using the Poynting vector, which is defined as the cross product of the electric field *E* and the magnetic flux density *B*. The Poynting vector indicates the flow of electromagnetic energy traveling through space per unit area and per unit time (W/m^2). For instance the power transmitted from an energy source can be determined using spheres surrounding the source. Every sphere has an associated Poynting vector associated which is inversely proportional to the distance from the source. The application of the Poynting's theorem in the MLM provides the power entering and leaving each layer in the model.

The Poynting vector in the frequency domain is: [74]

$$\overline{P} = \frac{\overline{E}_y \times \overline{H}_x^*}{2} \tag{4.22}$$

The electric field strength E_y can be related to the magnetic flux density, B_z from Faraday's law:

$$\overline{E}_y = \frac{\omega}{k}\overline{B}_z \tag{4.23}$$

From eqn. 4.22 and 4.23 the power entering a layer can be determined as: [68]

$$P_{in} = \mathrm{Re}\left\{\frac{\omega}{2k}\overline{B}_{z,n-1}\overline{H}_{x,n-1}^*\right\} \tag{4.24}$$

The net power dissipated in the *n-th* layer is the difference between the power entering into layer *n* from the *(n-1)th* layer and the power leaving the layer *n* into the *(n+1)th* layer, thus from eqn. 4.24: [68]

$$P_{in} = \mathrm{Re}\left\{\frac{\omega}{2k}\left(\overline{B}_{z,n}\overline{H}_{x,n}^* - \overline{B}_{z,n-1}\overline{H}_{x,n-1}^*\right)\right\} \tag{4.25}$$

From eqn. 4.25 the tangential force acting on the layer is: [68]

$$F_t = \frac{P_n}{\lambda f} \tag{4.26}$$

The mechanical power developed by the *n-th* layer at slip *s* is: [68]

$$P_{mech} = P_n(1 - s_n) \tag{4.27}$$

and therefore the I^2R loss is: [68]

$$P_n - P_{mech} = s_n P_n \tag{4.28}$$

The radial *z* directed levitation force in the general layer *n* through Maxwell stress is: [68]

$$F_r = -\frac{\mu_0}{4}\left(\frac{\left|B_{z,n-1}\right|^2}{{\mu_0}^2} - \left|H_{x,n-1}\right|^2\right) + \frac{\mu_0}{4}\left(\frac{\left|B_{z,n}\right|^2}{{\mu_0}^2} - \left|H_{x,n}\right|^2\right) \tag{4.29}$$

Where the positive and negative terms in F_r represent the attractive and repulsive forces on the layer.

4.4 Methodology

4.4.1 Introduction

In this section the methodology and considerations used to analyse the HSIM are discussed. There are a number of changes needed compared to the original MLM. First, anisotropic magnetic properties are included in the MLM (eqn. 4.30). Second, the current sheet is represented as another layer (Figure 4.3). Third, the process is simplified by implementing the algebraic concept of admittance [14]. Forth, the differential equation is changed to deal with the rotor surface velocity instead of angular velocity (eqn. 4.30). Finally, the performance of the machine can be solved by setting the required voltage rather than current using an iterative process. Although it is possible to include the effects

of saturation in the model with further development [15], the MLM used here, similar as the original one, neglects the effect of saturation. The consequences of disregarding the saturation in the model is examined in chapter 6 in which the MLM is saturated with high values of current. Eqn. 4.30 shows the modifications to the differential equation including the features discussed above. Figures 4.3 and 4.4 illustrate how the multi-region is now represented compared to before in Figures 4.1 and 4.2.

$$\alpha^2 = k^2\left(\frac{\mu_x}{\mu_z}\right) + jk\sigma v\mu_x \tag{4.30}$$

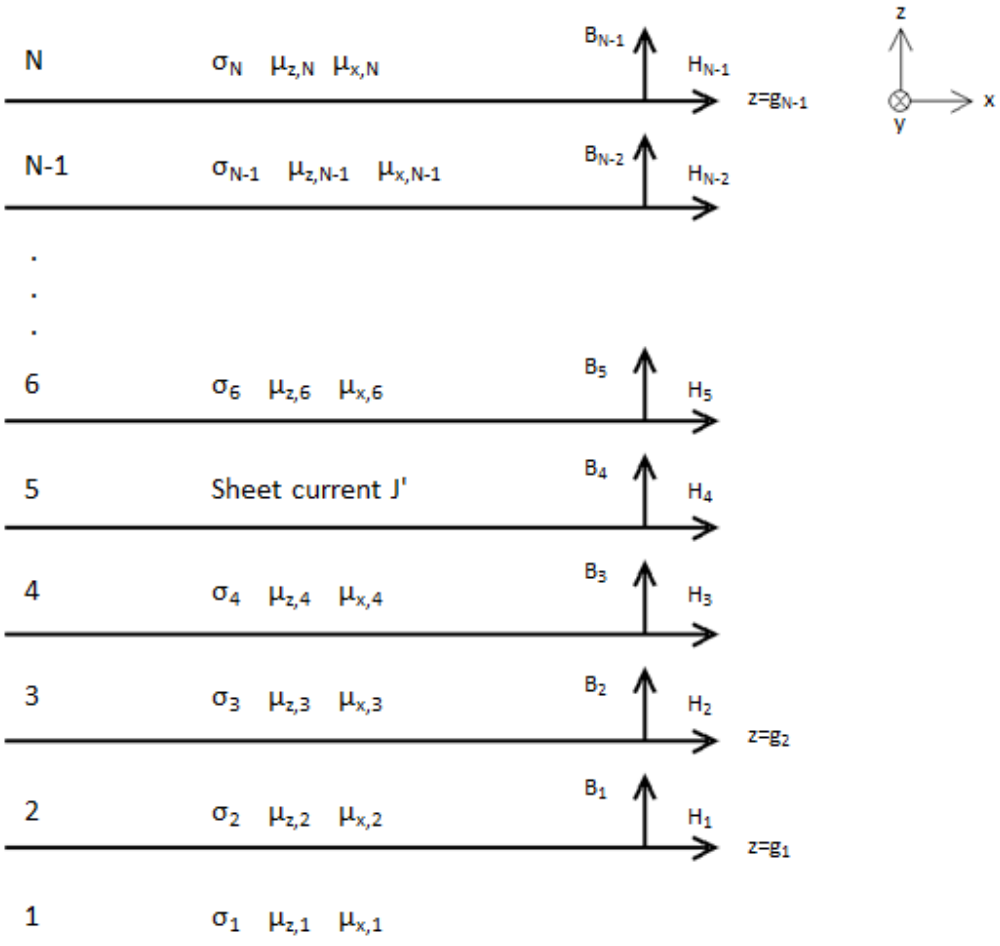

Figure 4.3 Improved multi-layer model.

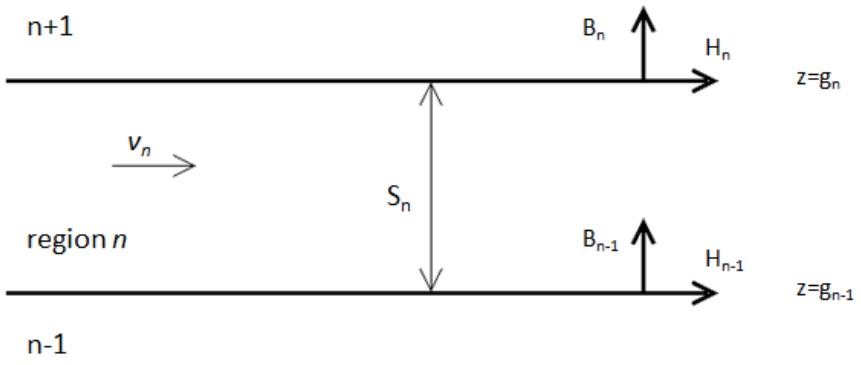

Figure 4.4 General layer.

4.4.2 Representing the stator slotting

The formulation of the MLM in a set of continuous layers is particularly well suited to linear and solid-rotor IMs. The rotor representation in these machines is straightforward. However, this is not the case for non-homogeneous regions such as the stator where there are alternating teeth and slots sections. The stator representation as a homogeneous layer sacrifices the finite details of construction and uses averaged permeabilities in the radial and tangential directions. Figure 4.5 illustrates how the non-homogeneous stator region is represented in the MLM as a group of continuous layers with anisotropic magnetic properties.

The anisotropic properties for the slotted region can be calculated using anisotropic layer theory [70]. Magnetic properties are approximated using the fundamental slotting harmonic values described in eqns. 4.31 and 4.32. Although this also applies to the conductivity, there is no need to calculate it since from eqn. 4.30 the conductivity only affects the solution in moving layers ($v \neq 0$).

Stator slot permeabilities: [70]

$$\mu_x \cong \frac{\mu_b p}{p_b + p_a \mu_b} \tag{4.31}$$

$$\mu_z \cong \frac{\mu_b p_b + p_a}{p} \tag{4.32}$$

Where:

$$p = p_a + p_b \tag{4.33}$$

μ_b is the permeability of the stator tooth, p_b is the tooth width, p_a is the slot width and p is the slot pitch.

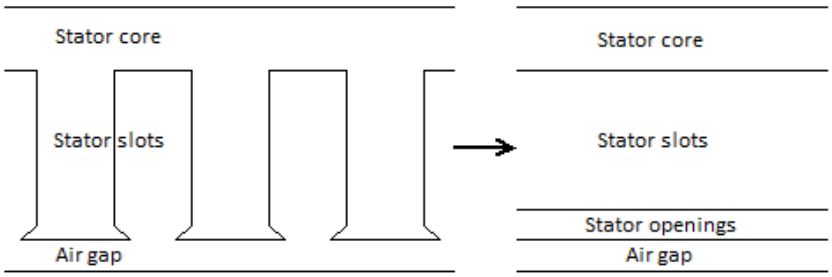

Figure 4.5 Layer representation of the IM stator.

4.4.3 Surface admittance

The surface admittance [14] is a mathematical simplification, which relates the boundary magnetising field strength with the flux density in each layer:

$$Y_n = \frac{H_n}{B_n} \tag{4.34}$$

Substituting and simplifying eqns. (4.11) and (4.12) in (4.34) yields:

$$Y_n = \frac{\beta_n B_{n-1} \sinh(\alpha_n S_n) + H_{n-1} \cosh(\alpha_n S_n)}{B_{n-1} \cosh(\alpha_n S_n) + \frac{1}{\beta_n} H_{n-1} \sinh(\alpha_n S_n)} \tag{4.35}$$

If eqn. 4.35 is divided by $\beta_n B_{n-1} cosh(\alpha_n S_n)$, the current layer admittance can be expressed in terms of the admittance of the layer below it:

$$Y_n = \frac{Y_{n-1} + \beta_n \tanh(\alpha_n S_n)}{1 + Y_{n-1} \dfrac{1}{\beta_n} \tanh(\alpha_n S_n)} \tag{4.36}$$

Or for the layer above it:

$$Y_{n-1} = \frac{Y_n - \beta_n \tanh(\alpha_n S_n)}{1 - Y_n \dfrac{1}{\beta_n} \tanh(\alpha_n S_n)} \tag{4.37}$$

From eqns. (4.36) and (4.37) the top and bottom boundary layer fields of Figure 4.3 are determined by considering condition (b) of section 4.3.3, in which the fields are assumed to decay to zero as *z* approaches $+\infty$ and $-\infty$

$$Y_1 = \frac{1}{j\sqrt{\mu_{x,1}\mu_{z,1}}} \tag{4.38}$$

$$Y_{N-1} = -\frac{1}{j\sqrt{\mu_{x,N}\mu_{z,N}}} \tag{4.39}$$

The top and bottom admittances of eqns. 4.38 and 4.39 can then be cascaded up and down through the layer model. Since the admittance relates the fields in each layer, H_n and B_n, by knowing one of them the other can be found. The determination of the fields in the MLM can be found with B_5 in Figure 4.3 following the process described below.

Since the current sheet layer has zero thickness, then it yields the following boundary conditions:

$$B_5 = B_4 \tag{4.40}$$

And:

$$H_5 = H_4 + \bar{J}^k \tag{4.41}$$

Dividing eqn. 4.41 by eqn. 4.40 we get:

$$Y_5 = Y_4 + \frac{\bar{J}^k}{B_5} \tag{4.42}$$

And solving eqn. 4.42 for the magnetic flux density:

$$B_5 = \frac{\bar{J}^k}{Y_5 - Y_4} \tag{4.43}$$

The magnetic strength can then be determined using the admittance:

$$H_5 = B_5 Y_5 \tag{4.44}$$

Using eqns. 4.44, 4.40 and 4.41 the fields B_5, H_5 can then be cascaded up to layer N whilst fields B_4, H_4 can be cascaded down to layer 1 using the transfer matrix of eqn. 4.15 or 4.16.

4.4.4 Stator winding input

4.4.4.1 Overview

In a similar fashion to the FE model, the MLM is based on a current input rather than voltage. However, by varying the current of the model it is possible to make the MLM behave as if it was voltage driven. Constant current operation is included to compare the MLM with the FEMM model in their original form and also as background to constant voltage operation.

4.4.4.2 Current input

It is common to represent the stator current sheet of a three-phase IM with a Fourier series; this extends the analysis of the MLM to induce the mmf harmonics. The MLM is solved by inserting each current harmonic separately as a current sheet layer (layer 5 of

Figure 4.3) and then using superposition to add up the harmonic contributions of the fields, forces, losses, etc.

The stator specific electric loading along the *x* direction can be expressed as follows:

$$\bar{J} = \frac{6N_{PH}I_{ph}}{\pi D}\sum_{\upsilon=-\infty}^{\infty} k_w^{\upsilon} e^{j(\omega t - k^{\upsilon}x)} \tag{4.45}$$

And $\upsilon = \pm 1, \pm 2, \pm 3, \ldots$ N_{PH} is the number of conductor per phase, I_{ph} is the *rms* stator current, D is the mean air gap diameter and k_w is the winding factor.

For a single harmonic therefore:

$$\bar{J}^{k} = \frac{6N_{PH}I_{ph}}{\pi D} k_w^{\upsilon} e^{j(\omega t - k^{\upsilon}x)} \tag{4.46}$$

Where:

$$k^{\upsilon} = \frac{2\pi}{\lambda} \tag{4.47}$$

As evident from eqns. 4.47, 4.11 and 4.12, special precaution should be taken with the solution for the fields when high harmonic numbers and thickness are involved, since high values in the argument of the hyperbolic functions can generate a numerical precision problem. Although the admittance transfer helps to minimise this problem (hyperbolic tangential functions do not grow exponentially), the hyperbolic functions cannot be avoided entirely because they are used in the transfer of the fields (eqns. 4.13 and 4.15) through the model. This tends to affect mainly the outer layers far from the air gap and the higher harmonic numbers. However, in practice there is no need to transfer fields further than a few layers away from the air gap region, since this is where torque production occurs. The number of harmonics should be limited to values that allow using hyperbolic functions.

The input to the layer model is current (the current sheet layer) and the output is the field distribution in the MLM. For a harmonic model, there would be different input currents, which correspond to each harmonic component of the winding current distribution. The losses, torque, fields, etc. are obtained by adding each individual harmonic contribution.

4.4.4.3 Voltage input

In section 3.4.3.3, the procedure to make the FEMM model voltage controlled rather than current controlled was described. The same iterative process can be implemented in the MLM to make it voltage driven as well. However, this needs a small variation because the MLM, as opposed to FEMM, does not calculate intrinsically the voltage across the terminals of the windings; an approximate stator voltage value has to be calculated from the field distribution.

The stator voltage in the model can be approximated from Faraday's law:

$$E_{ph} = \int (v \times B) \cdot dl \tag{4.48}$$

Where v is the relative speed and B is the magnetic field.

Considering the total number of conductors per phase, the velocity of the travelling fields, and the normal magnetic field component:

$$E_{ph} = k_w N_{ph} \left(\frac{\omega}{k^{\upsilon}} \cdot B \right) \cdot l \tag{4.49}$$

Where N_{ph} is the number of turns per phase and ω is the electrical stator angular frequency.

Eqn. 4.49 approximates the per-phase voltage in the stator layer. This voltage is shown as E_{MLM} in Figure 4.6. To determine the full per-phase stator voltage it is necessary to take into account the effect of the external winding impedance comprising the stator resistance and the leakage reactance. As Figure 4.6 illustrates, the excitation current of

the MLM enters directly into the node of the magnetising inductance branch omitting the external winding impedance.

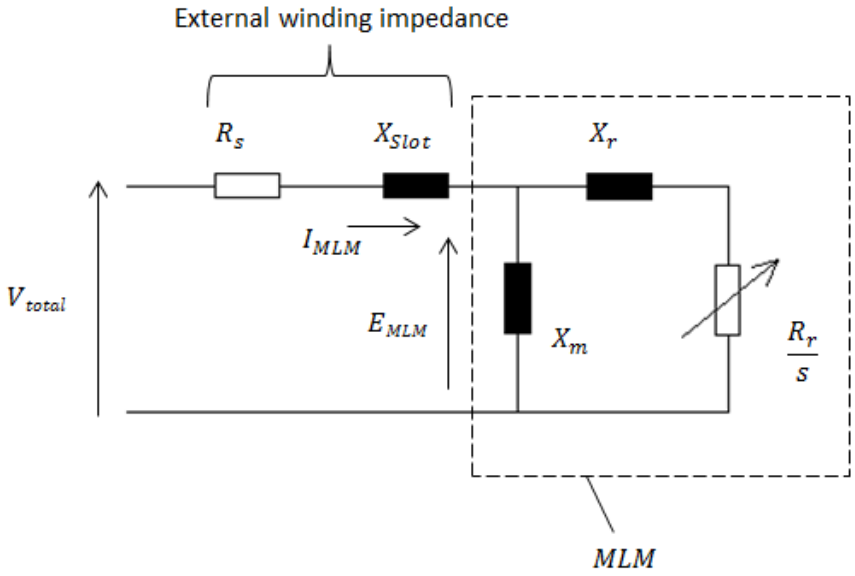

Figure 4.6 Excitation current and voltage generated in the MLM.

The total voltage can be calculated by including the winding impedance term:

$$V_{total} = I_{MLM} \cdot (R_S + jX_S) + E_{MLM} \tag{4.50}$$

For constant voltage operation, the desired value for the MLM voltage in eqn. 4.49 can be conveniently included in the model using:

$$E_{MLM} = V_{total} - I_{MLM} \cdot (R_S + jX_S) \tag{4.51}$$

The winding slot leakage reactance can be approximated by eqn. 4.52: [75]

$$X_{Slot} = \omega N_c^2 l \mu_0 \lambda_S \tag{4.52}$$

Figure 4.7 illustrates the concept of the MLM approach with the voltage as the input to the model. For a required voltage, an iterative method varies the current of the model until the relative error between the desired voltage and the approximated voltage is within the error tolerance. The fields resulting from the process are then used to

calculate: torque, losses, etc. The complete performance of the machine is obtained by implementing this iterative process for each value of slip.

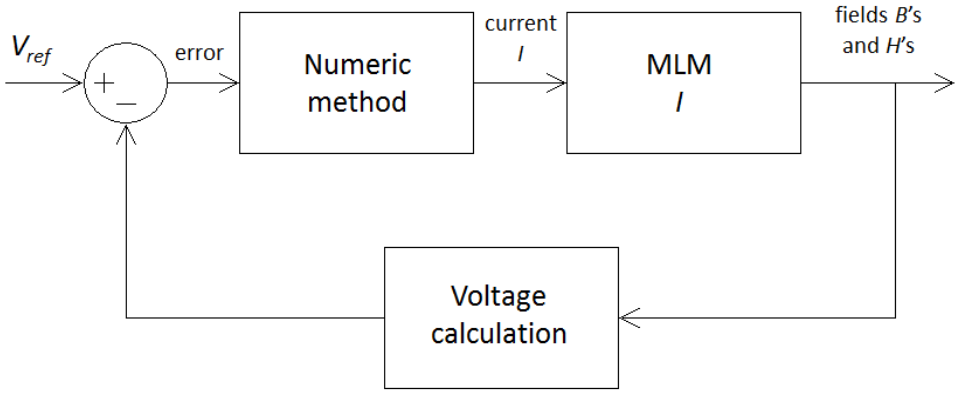

Figure 4.7 Representation of the constant voltage operation for the MLM.

4.5 High-speed induction motor modelling

4.5.1 Introduction

In this section the HSIM is analysed using the theory and methodology previously described. The inclusion of constant current operation results in the next chapter is for comparison purposes and understanding the saturation effects in the model.

4.5.2 Multi-layer model

Since the topology of the rotor in the HSIM consists of two continuous regions: a solid rotor steel core and a copper coating; representing the HSIM is not only suitable but straightforward as shown in Figure 4.8. There is only one non-homogeneous region in the stator that needs transforming into equivalent anisotropic layers, as described in section 4.4.2. Since layers 7 and 6 possess anisotropic properties, their permeabilities are different in z and x directions. The stator current excitation is represented by a current density sheet placed immediately above the air gap. All the field and excitation current values within the MLM are expressed in phasor notation.

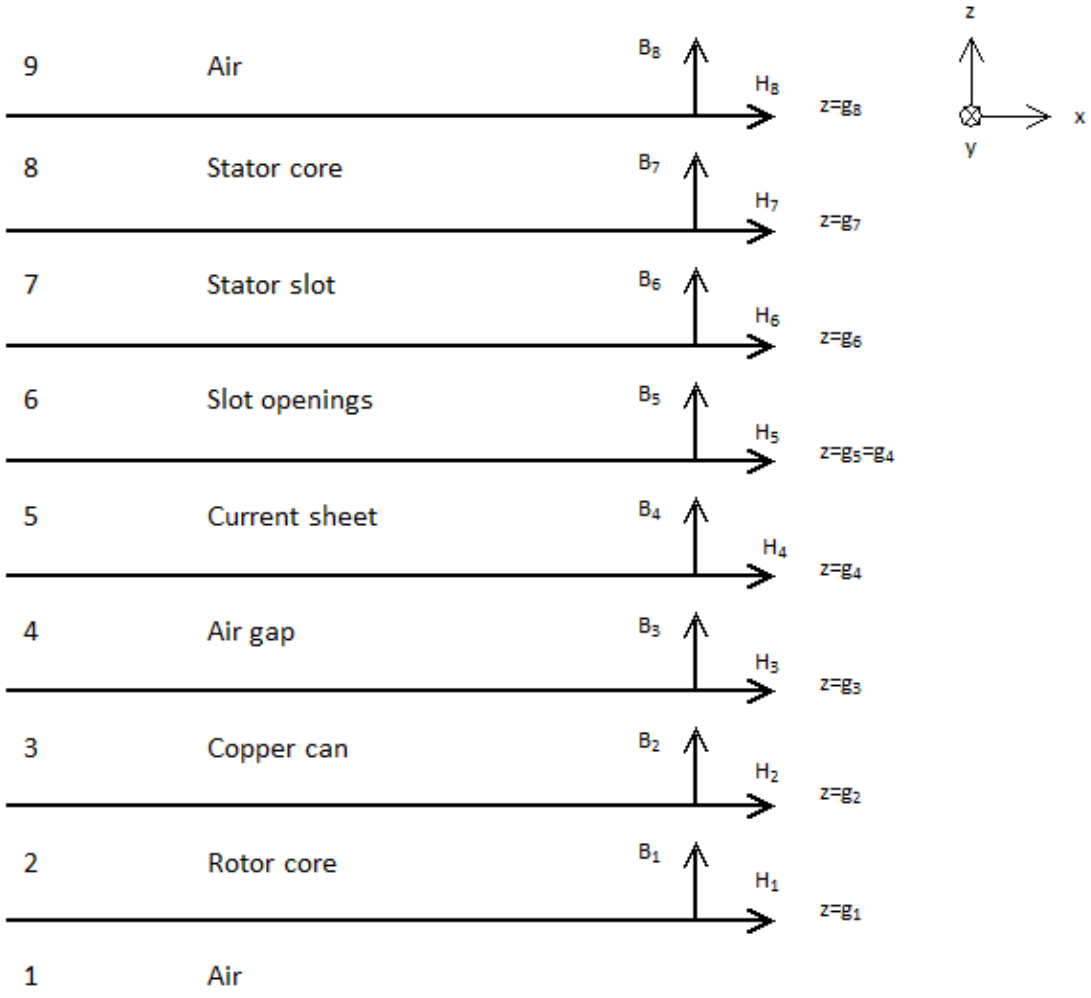

Figure 4.8 Multi-layer model of the HSIM.

4.5.3 Analysis of the HSIM

4.5.3.1 Overview

Constant current and voltage are the input source to the MLM throughout the entire slip domain. Both of them are based on the layer model of Figure 4.8 and have the properties summarised in Table 4.1. The inclusion of constant current operation is to compare FEMM with the MLM directly. The model is solved on a harmonic basis using 200 harmonics.

n	Layer	Velocity	Thickness	Conductivity	Permeability	Admittance	Fields
9	Air	0	∞	-	μ_0	-	0
8	Stator core	0	S_8	-	μ_8	Y_8	B_8, H_8
7	Stator slot	0	S_7	-	$\mu_{x,7} \neq \mu_{z,7}$	Y_7	B_7, H_7
6	Slot openings	0	S_6	-	$\mu_{x,6} \neq \mu_{z,6}$	Y_6	B_6, H_6
5	Current sheet	0	0	-	μ_0	-	B_5, H_5
4	Air gap	0	S_4	-	μ_0	Y_4	B_4, H_4
3	Copper can	v_n	S_3	σ_3	μ_0	Y_3	B_3, H_3
2	Rotor core	v_n	S_2	-	μ_2	Y_2	B_2, H_2
1	Air	0	∞	-	μ_0	Y_1	B_1, H_1

Table 4.1 Layer properties of the HSIM.

4.5.3.1 Constant current operation

The procedure to implement the MLM is described as follows. First, the data in Table 4.1 is introduced to the model. Then admittances of layers 1 and 8 are calculated using eqns. 4.38 and 4.39 respectively and they are cascaded upwards and downwards to the current sheet using eqns. 4.36 and 4.37. The fields of layers 5 and 4 are then calculated using eqns. 4.40-4.44. The fields are cascaded in a similar way as the admittances; upwards and downwards using eqns. 4.13 and 4.14 respectively. At this point solving the MLM only requires setting a per-phase current and varying the speed of layers 3 and 2 in accordance with the slip. In this case the current is maintained constant. However, for the constant voltage operation the current is varied until the desired voltage is reached.

The HSIM is fed with a constant current of 20 (A) throughout the entire slip domain. This produces a variable per-phase voltage through the slip domain (Figure 4.9). Figures 4.10 and 4.11 show the output of the model, the torque and losses in the copper can respectively. To avoid saturation (the MLM in this thesis does not take saturation into account), the current is set to the value of 20 (A) for which the flux density is 0.8 (T) in

the air gap region. Further increases in the current will produce proportional increases in the air gap flux density, the torque, etc. A more detailed description regarding saturation in the model is presented in chapter 5.

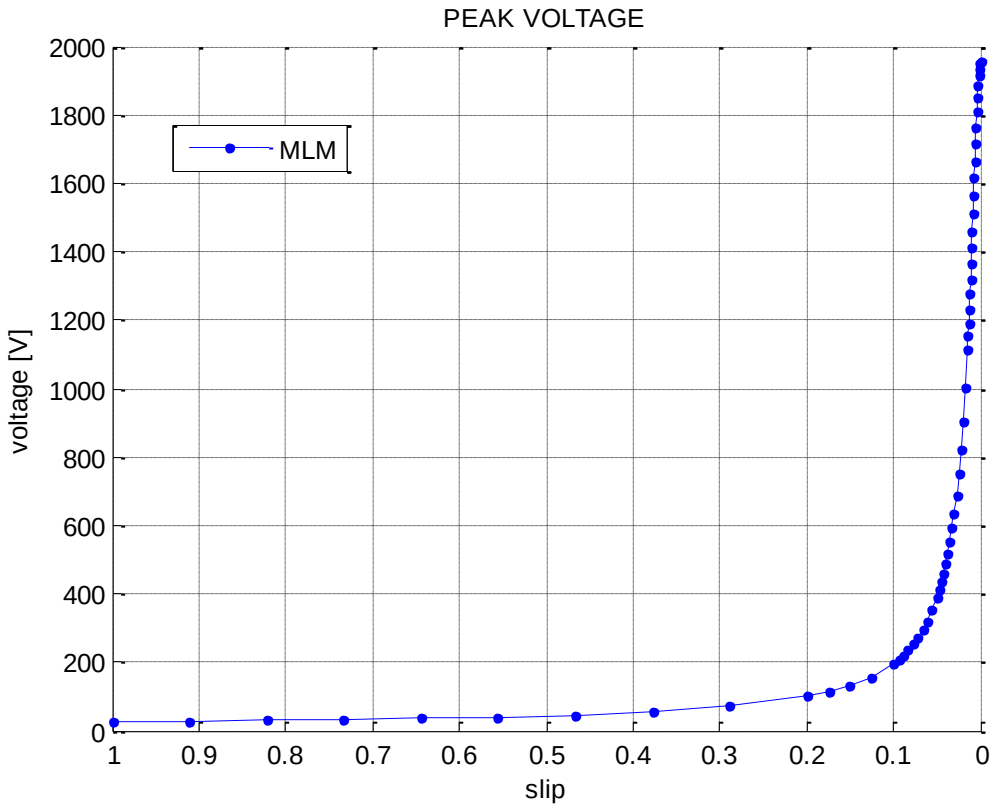

Figure 4.9 Per-phase peak stator voltage.

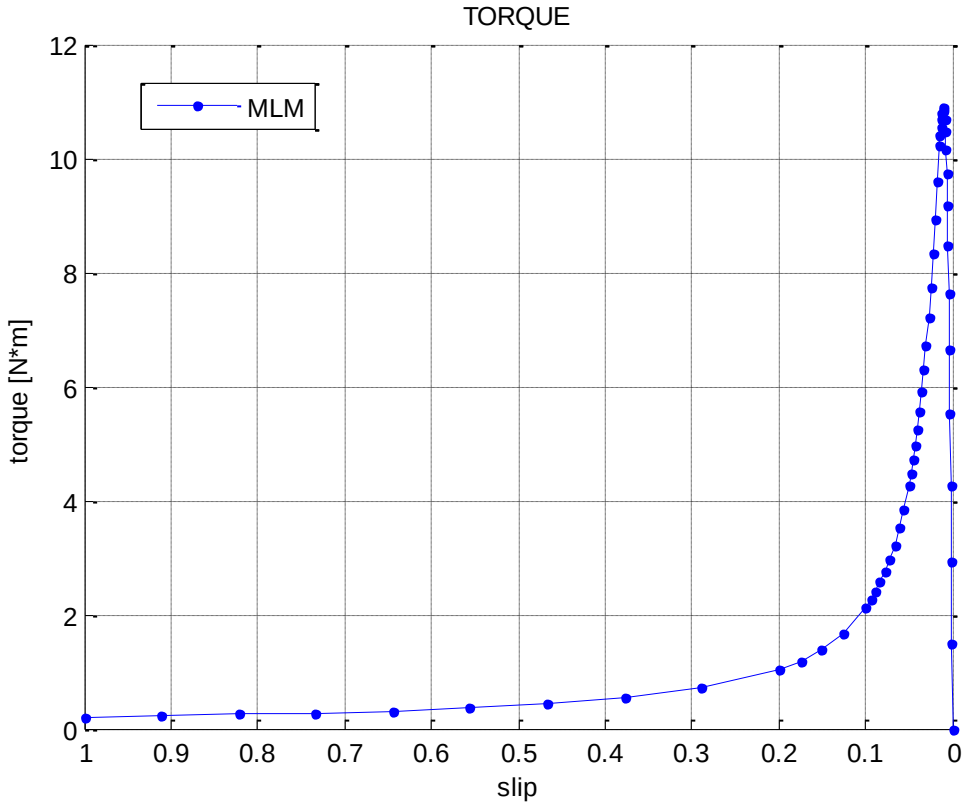

Figure 4.10 Torque developed.

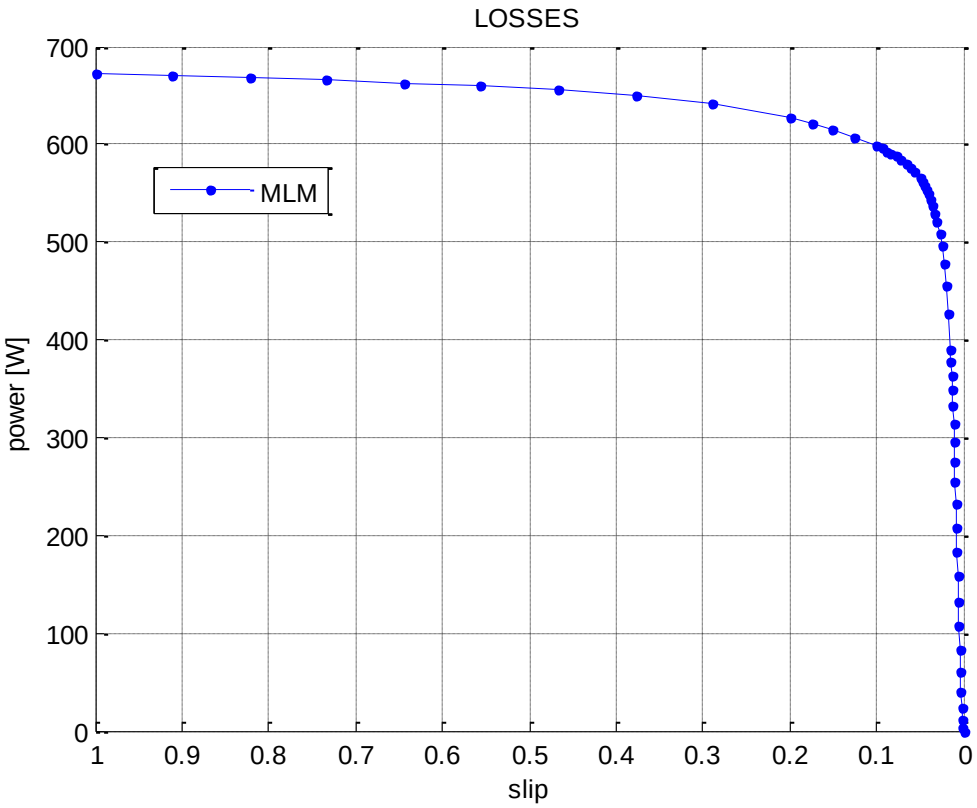

Figure 4.11 Rotor can losses.

4.5.3.2 Constant voltage operation

For a constant voltage operation the MLM follows the same procedure described in the previous section except from the fact that in voltage operation, the current is unknown. The model depends on the current to calculate all the other quantities (fields, torque, voltage, etc.). The MLM therefore needs to iterate the current until the voltage reaches the desired set voltage, as Figure 4.7 illustrates. Figure 4.12 shows the resultant voltage during the iterative process in the stator; its values are within the error bound of 2% with respect to the set voltage of 170 (V). The stator current for constant voltage performance is shown in Figure 4.13. The torque developed and copper can losses in Figures 4.14 and 4.15 respectively, are not as smooth compared to the constant current model due to the error bounds on the iterative approach. A reduction in the error bound would produce smoother torque and loss; it would require, however, more iterations and consequently more processing time. Increasing the processing time would be slightly counter-productive because the MLM is intended to be a fast auxiliary tool in the design of HSIMs.

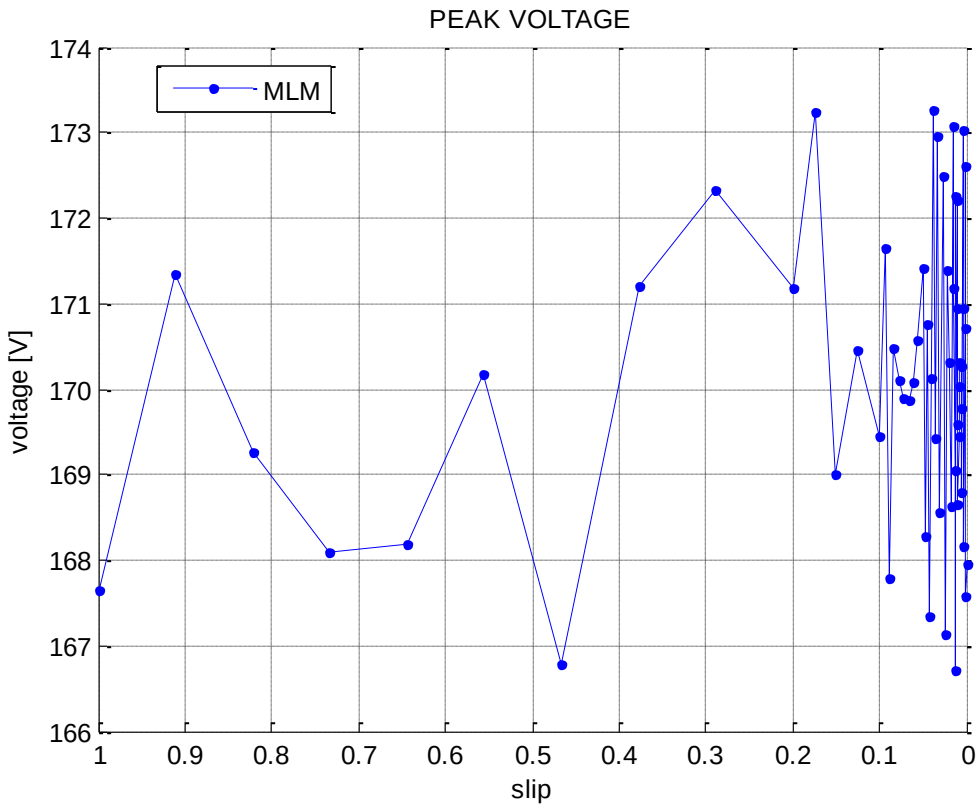

Figure 4.12 Per-phase peak voltage.

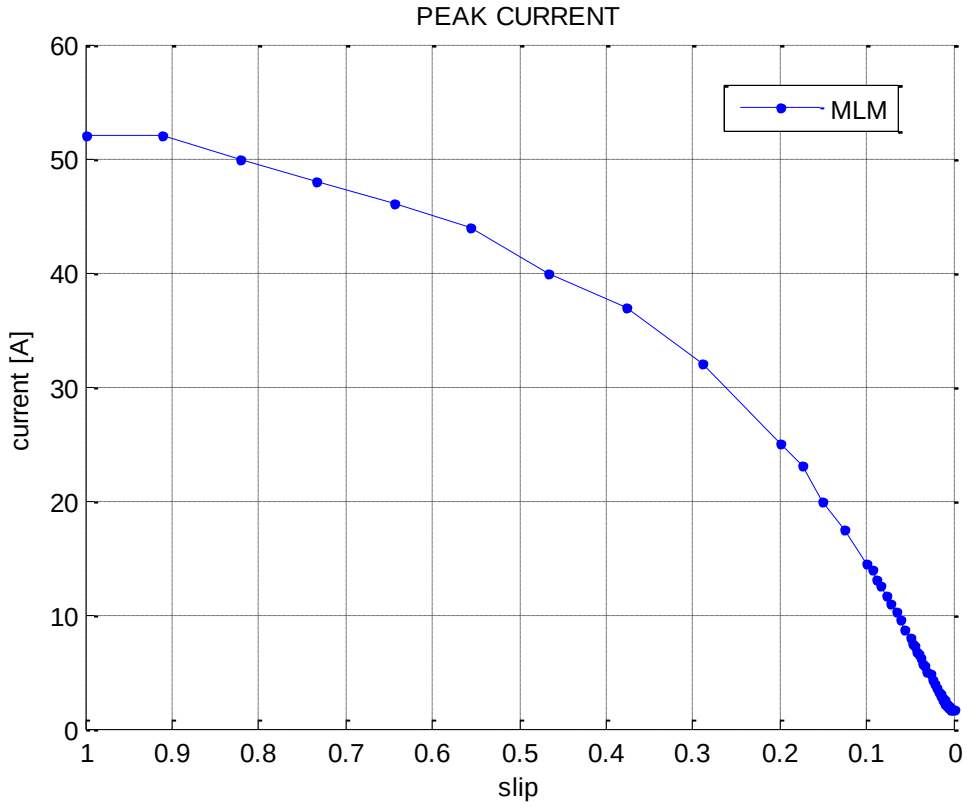

Figure 4.13 Peak current input.

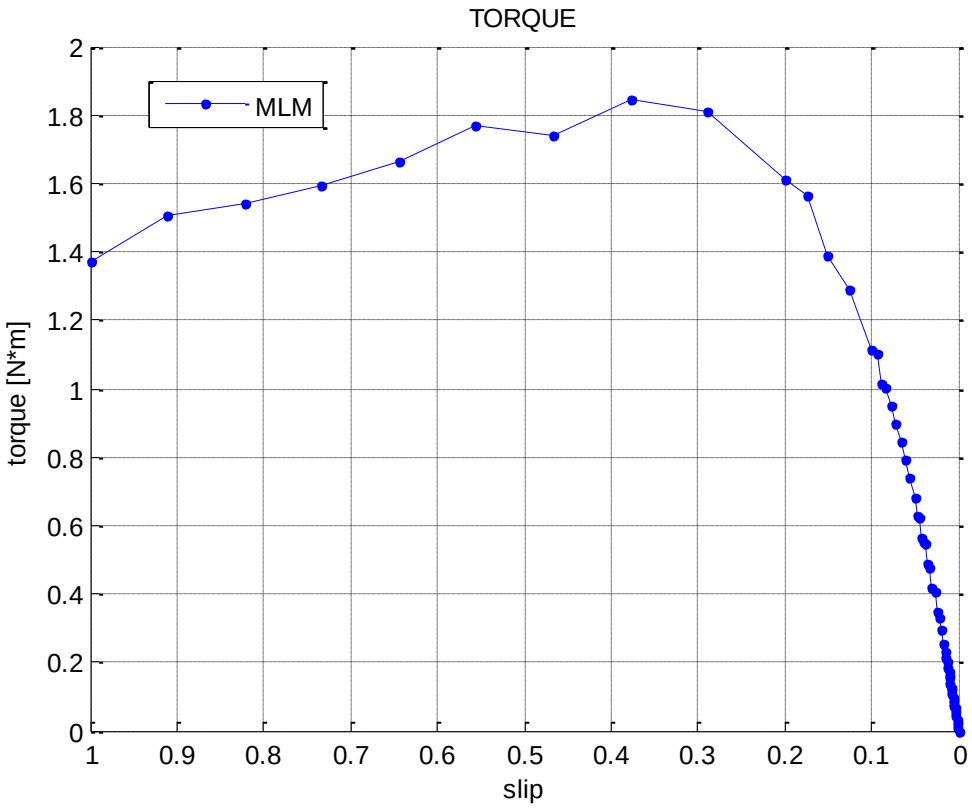

Figure 4.14 Torque developed.

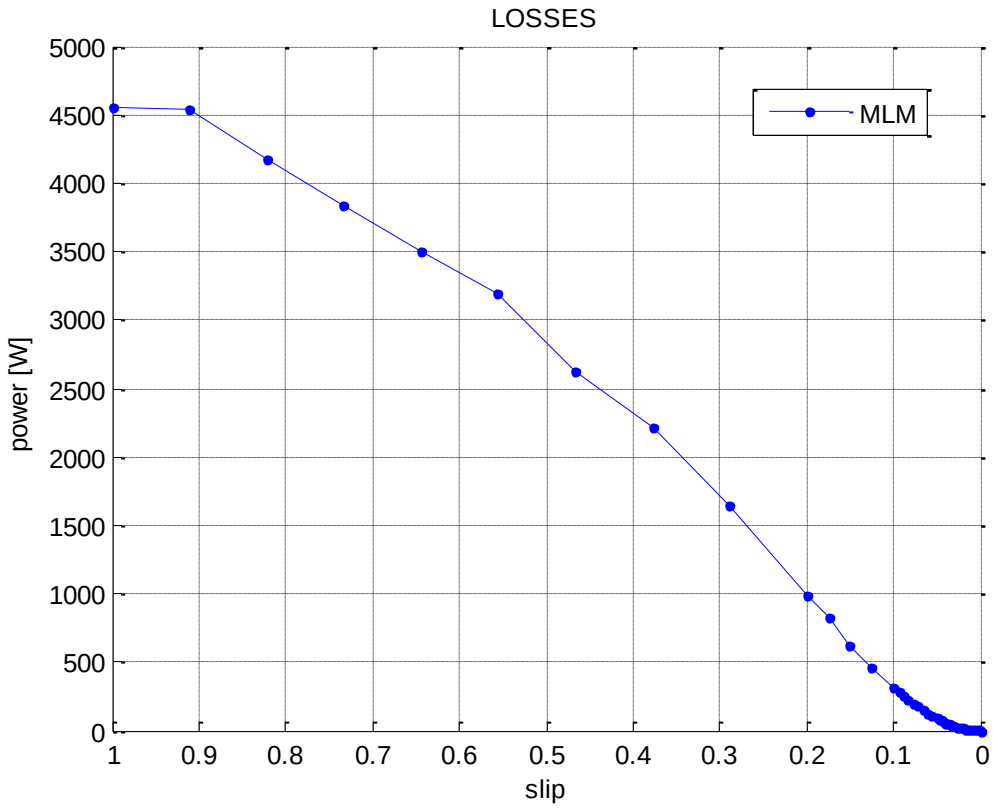

Figure 4.15 Can losses.

4.6 Summary

The MLM is an analytical method for IMs. Although it was originally conceived to predict the performance of squirrel-cage IMs, it was used subsequently to analyse other type of IM topologies. Given the planar geometry of continuous layers from which the MLM is formulated, the MLM is likely to deliver more accurate results depending how close the structure of the machine is to the layer formulation. Finer details of the machine like the toothed and slotted zones are approximated in the equivalent layer model. For the case of the canned solid-rotor HSIM, however, its topology suits the MLM formulation. Similar to FEMM, the MLM natural input is the current; so an iterative approach is needed to enforce a constant voltage input.

In this chapter the theory of the MLM was presented as well as the methodology to analyse an IM. Using this methodology, the HSIM was analysed under two conditions:

constant current and constant voltage operation. Constant current operation of the MLM was presented here to provide a better understanding of constant voltage operation and to use it in the next chapter to cover important points in the performance of the MLM.

Chapter 5

Comparison and Review of the Analytical and Finite Element Models

5.1 Introduction

The two previous chapters addressed the HSIM analysis using FE and analytical modelling. Here the results obtained in the previous chapters are compared in three sections. The first one contrasts the results of both models in constant current operation. The second section compares the models under constant voltage operation. The last section provides a comparison of the performance of the MLM and how the implementation could be improved further.

5.2 Comparison of models for constant current

As discussed in chapters 3 and 4, the natural input source for the MLM and FEMM models is current. Constant current operation is useful for comparison purposes because it is easier to assess the effect of disregarding magnetic saturation in the MLM (by definition the MLM ignores saturation). Additionally, this section shows how the flux density, from which all the other quantities are calculated, behaves for saturating current values.

Figures 5.1 and 5.3 show the voltage and torque of the MLM and FEMM (using the slip conductivity approach) models for 20 (A) throughout the entire slip domain. The difference between the voltages for the MLM and FEMM models in Figure 5.1 is small for slip values close to 0 but increases for slip values close to 1. This can be explained as

due to the approximate calculation of the voltage in the MLM using the flux density levels (section 4.4.4.3). The difference between the MLM and FEMM models becomes more noticeable under constant voltage operation, because the current is varied to obtain the desired voltage.

As illustrated in Figures 5.2 and 5.3, the flux density levels in the air gap and the torque predicted by the MLM are very close to those obtained from the FEMM model despite the simplification of the stator slotting using homogeneous layers in the MLM model (the main difference between graphs in Figure 5.2 is mostly due to the stator slotting which is modelled in more detail in FEMM). There are three main reasons for this: the simple HSIM geometry suits the formulation of the MLM; the MLM is being compared directly in a constant current basis (as opposed to constant voltage operation); and the current input does not saturate the MLM.

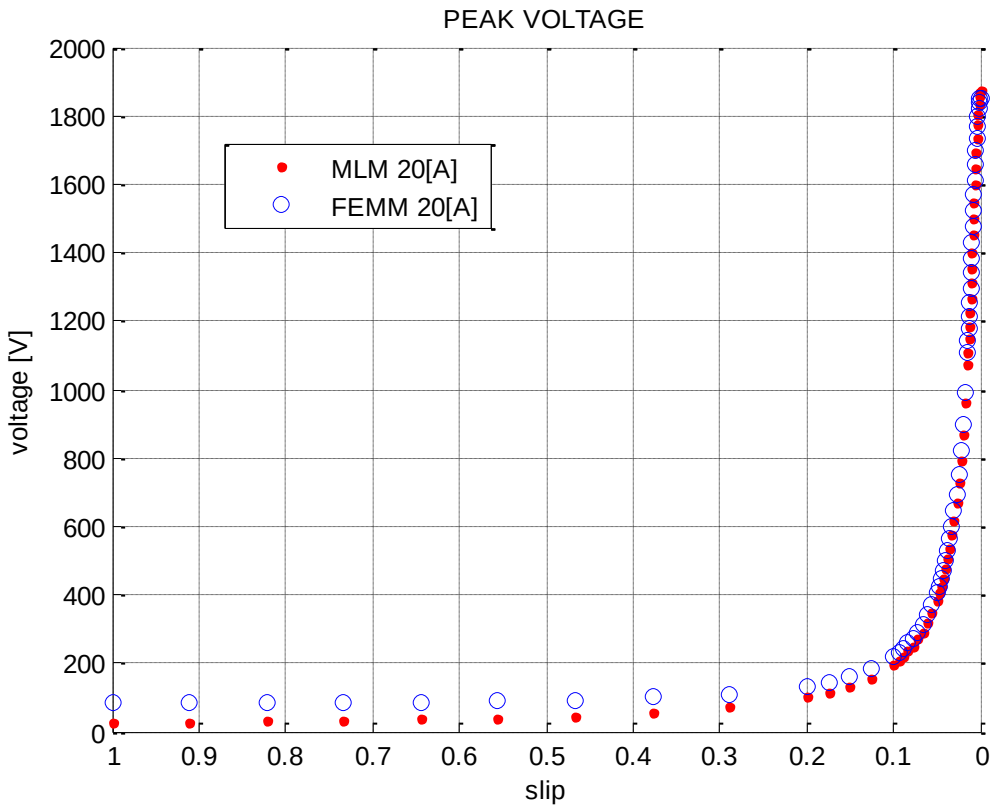

Figure 5.1 Peak voltage comparison between analytical and FE models.

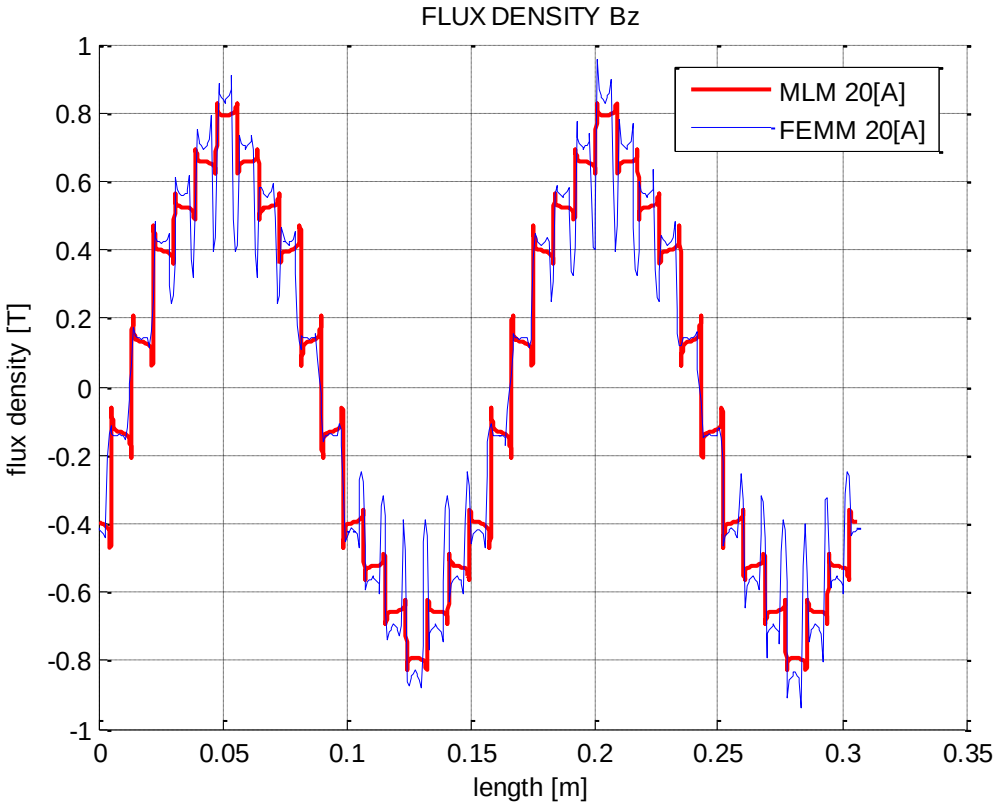

Figure 5.2 Flux density around the air gap of the HSIM.

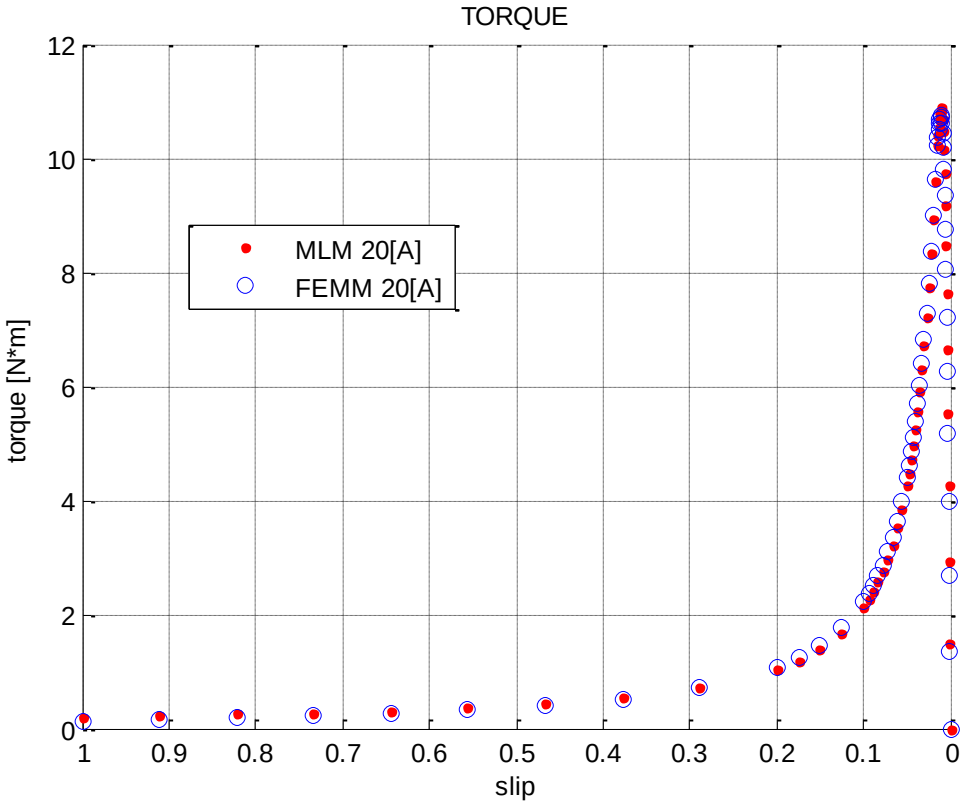

Figure 5.3 Torque comparison between analytical and FE models.

Since the MLM in its basic form does not consider saturation, any further increase in the current will cause a simple proportional increase in the field levels and consequently also reflected in the calculation of losses, torque, etc. Figures 5.2 and 5.3 illustrate a good agreement between the MLM and FEMM models when the input current does not lead to saturation. However, if the current input to the model is increased to a saturating value of 60 (A), the air gap flux density increases significantly beyond the recommended design value of 0.8 (T) [18] in Figure 5.4. As can be seen in Figure 5.5 the difference between the MLM and FEMM models is much more pronounced than before in Figure 5.3. Figures 5.4 and 5.5 clearly show the influence of saturation in the MLM as opposed to FEMM model, which calculates saturation automatically.

Although it is possible to modify the MLM to account for saturation effects as in [15], the MLM used in this thesis maintains the same approach as the original MLM. In order to obtain adequate results from the MLM therefore, it is sensible to check that the flux density around the air gap does not lead to saturation in the magnetic circuit. In Figure 5.2 the flux density is close to the design value of 0.8 (T), and the agreement between the MLM and FEMM is good. Figures 5.4 and 5.5 illustrate the large discrepancy between the MLM and FEMM when the MLM has a current input that produces a flux density significantly greater than the design value of 0.8 (T) in the air gap.

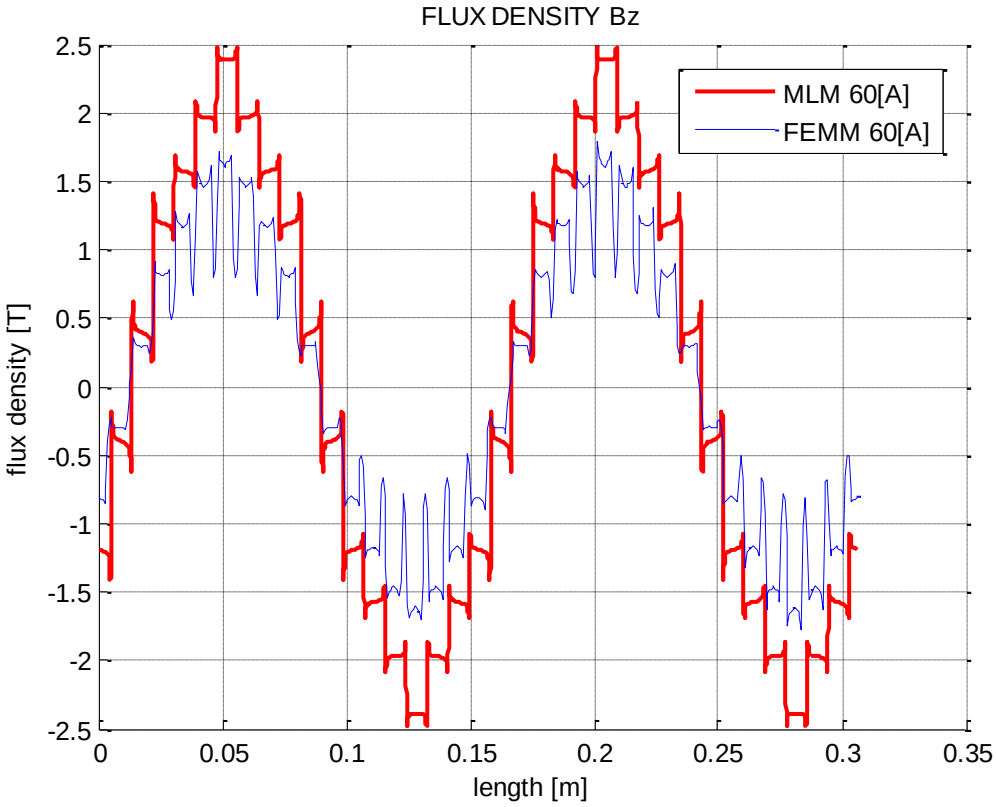

Figure 5.4 Effect of neglecting saturation in the MLM compared to the FEMM model.

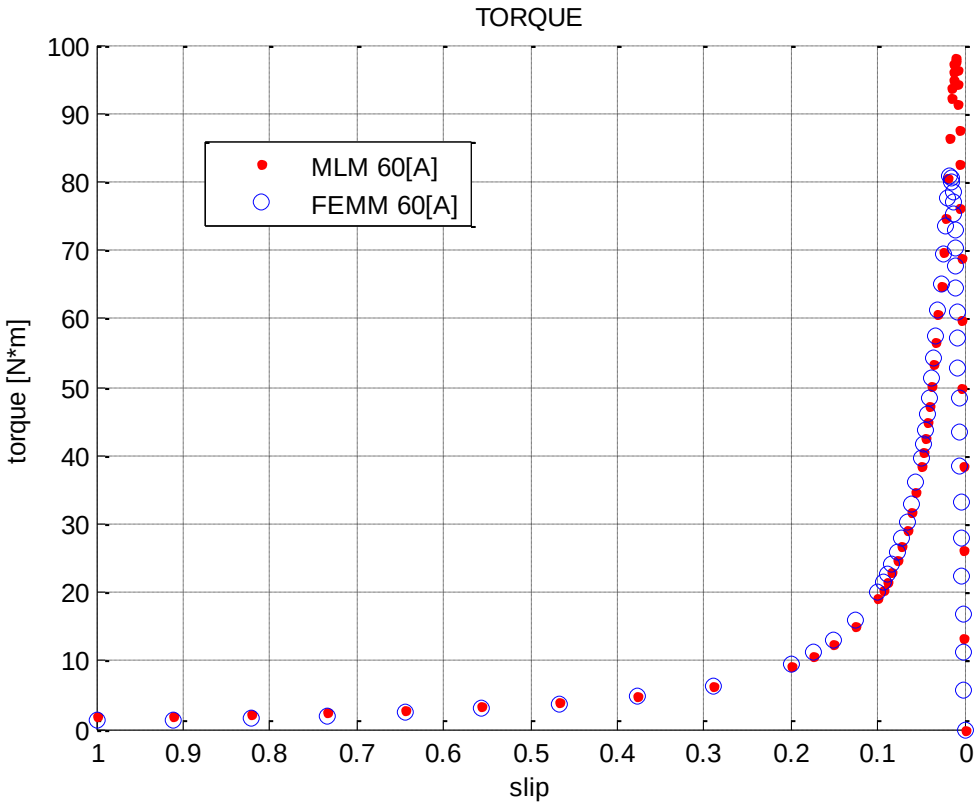

Figure 5.5 Torque characteristics.

5.3 Comparison of constant voltage models

Constant voltage operation for the MLM and FEMM models can be undertaken using an iterative process. Basically, from a starting value, the current is increased or decreased in steps until the desired voltage is reached. As shown in chapters 3 and 4 the procedure to simulate constant voltage operation is virtually the same for the MLM and FEMM models, the difference lies in that the MLM approximates the voltage from the flux density levels whereas the FEMM model determines the voltage using the magnetic vector potential solution.

Figures 5.6 and 5.7 show the current and torque obtained from the MLM and FEMM for a constant peak voltage value of 170[V] with an error tolerance of 2%. Figure 5.6 shows the current required to achieve constant voltage operation in the MLM and FEMM models. It can be seen that the MLM current deviates from the FEMM values as the slip approaches 1. This is related to the approximate method of determining the voltage using the flux density levels in the MLM.

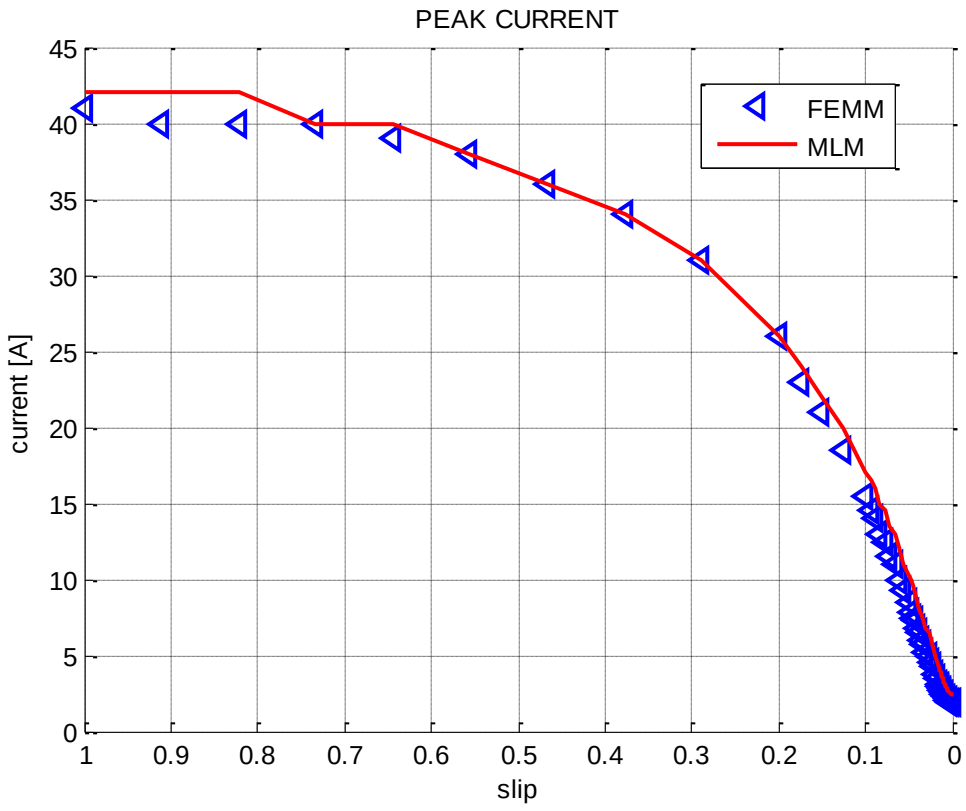

Figure 5.6 Peak current of both models under constant voltage operation.

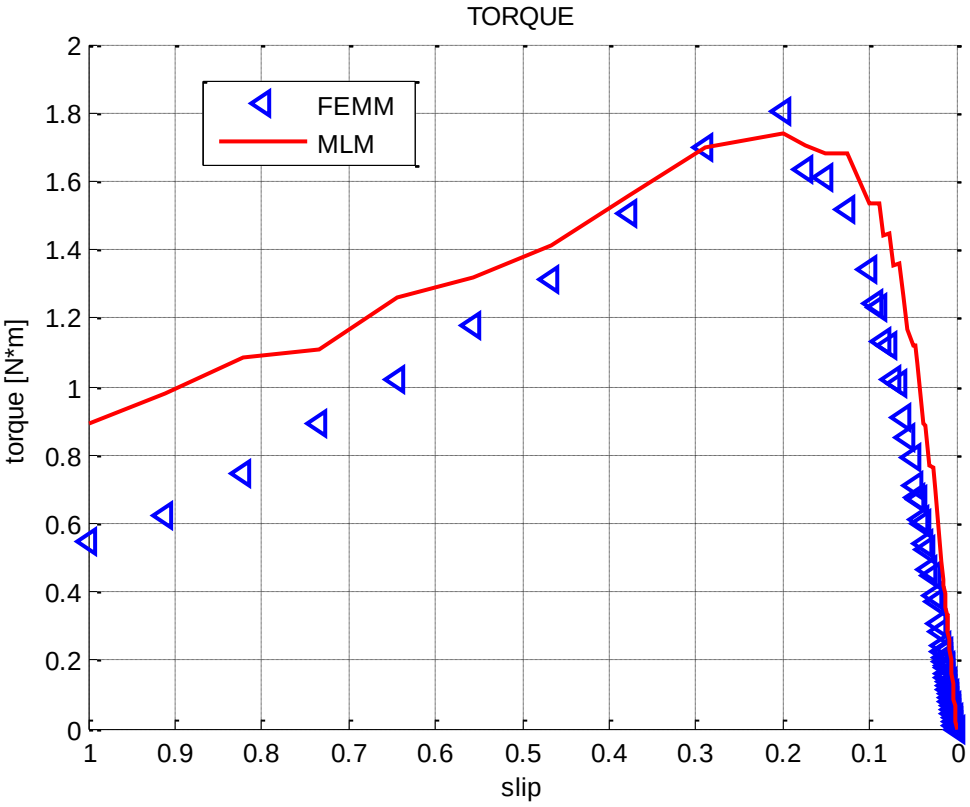

Figure 5.7 Torque comparison between the MLM and FEMM models.

5.4 Discussion

In the previous section it was pointed out that the main difference between the analytical and FE models under constant voltage operation was more evident as the slip approached 1; this was due to the approximation made in the MLM to determine the voltage in the MLM using the flux density in the air gap.

As mentioned before the natural input source for the MLM and FEMM models is current. IMs, however, are normally fed from a constant voltage source rather than current. A way to deal with this situation is varying the current input until the desired voltage is reached. Although this process is virtually the same for the MLM and FEMM, the implementation in the MLM tends to be less accurate for slip values close to 1 due to the simplistic calculation of voltage in the MLM. If the exact current required to produce

constant voltage operation in the MLM was known beforehand, then the MLM results would improve significantly.

Figure 5.8 shows three cases for comparison: the MLM operating at constant voltage of 170 (V), denoted as 'MLM 170[V]'; the FEMM model operating at a constant voltage of 170 (V), denoted as 'FEMM 170[V]' and finally the MLM fed by exactly the same current as the FEMM model, which operates at a constant voltage of 170 (V), denoted as 'MLM varI'. The respective torque of each one of these three cases is shown in Figure 5.9. It can be seen that 'MLM 170 [V]' differs from 'FEMM 170 [V]' at slip values close to 1; this is due to the approximation of the voltage using the calculation of the winding reactance under the constant voltage operation (eqn. 4.52). However, if the MLM is fed with exactly the same current as the FEMM model, then the MLM prediction becomes more accurate, as can be seen from Figure 5.9. This means that if the calculation of voltage can be improved in the MLM, then the MLM model results would also improve.

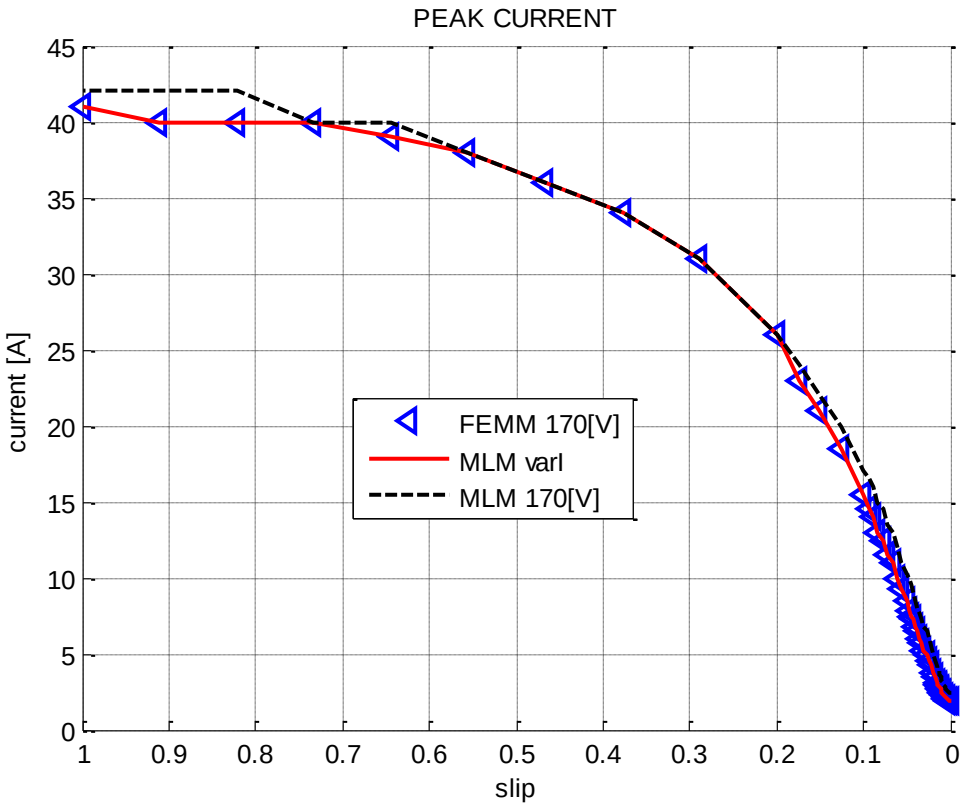

Figure 5.8 Peak current comparison.

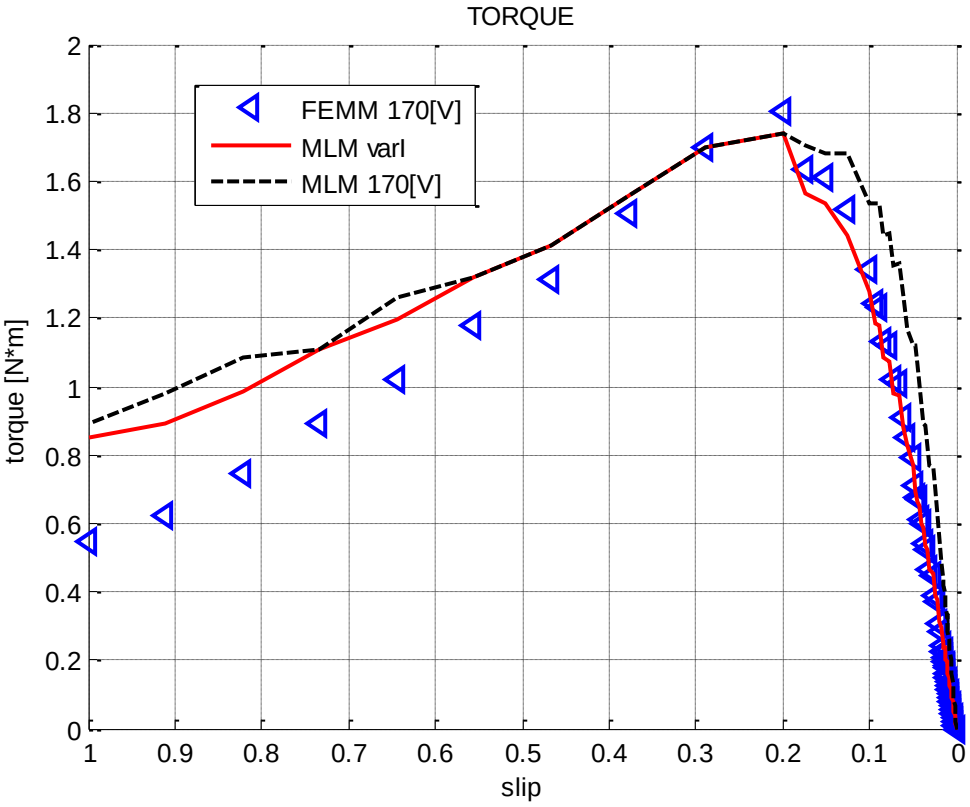

Figure 5.9 Torque comparison.

5.5 Summary

When implemented correctly the MLM can deliver accurate results close to those obtained from the FE model. The MLM approach can be modified to operate from a constant voltage source. To perform under a constant voltage operation, the current of the MLM is varied iteratively until the terminal voltage is within the error tolerance of the desired supply voltage.

This chapter addressed two important points for the implementation of the MLM. First, disregarding the saturation effects, which means that a check has to be included so that the field in the layers in the model that include electrical steel do not exceed a predetermined design level to avoid magnetic saturation. If operation is required in the saturated region, then the MLM approach needs to be further modified to include another iterative loop for the magnetic permeabilities linked to the saturation curve for the

electrical steels. The second point was that although the constant voltage operation of the MLM showed pronounced differences for slip values close to 1 comparing it with FEMM model, the MLM would deliver more accurate results if the voltage calculation was improved.

Chapter 6

Conclusions and Future Work

6.1 Conclusions

The work presented in this thesis describes the procedure to determine the electromagnetic performance of high-speed copper-coated solid rotors using the analytical MLM on a harmonic basis. The MLM is intended to reduce the time spent in the electromagnetic design by using it as a preliminary design tool. A high-speed motor model was analysed using both FEA and the MLM. The analytical MLM results were compared to those obtained from FEA and its suitability as a fast design tool for high-speed copper-coated solid rotors assessed.

The MLM was chosen as the analytical method to perform the electromagnetic analysis of a high-speed copper-coated solid rotor model because its formulation not only adequately suits the physical arrangement of the model but also because its methodology is practical and simple to implement. The MLM avoids the meshing issues that the FEA model would present for high-speed solid rotors; this feature is particularly useful in dealing with the problem of the small skin depths associated with those rotors.

The two-dimensional MLM based on Maxwell's equations determines the electromagnetic field distribution in a multi-regional arrangement of layers, which are defined by certain physical properties, such as velocity, magnetic permeability, conductivity, etc. The approach adopted to solve the MLM included: tangential permeability in the model; the current sheet (the natural source input to the model) as another layer; neglected the effect of saturation; and solved the fields by transferring the admittances in the layers. Voltage operation was achieved by varying the current to the model until the magnetic fields produced the desired reference voltage. The performance

characteristics obtained under constant voltage operation were not as smooth as the constant current operation because the iterative method of bisection used to determine the current employed an error bound to reach convergence. The error bound was set up to a value of 2% to obtain faster results; a reduction of the error bound would lead to smoother curves for constant voltage operation.

FEMM was the FE software selected to compare the analytical results because FEMM shares some similarities with the MLM and it made the assessment more appropriate for both constant current and constant voltage operation. FEMM runs in a 2-D environment and its source input is current. For constant voltage operation, the same iterative method of bisection used for the analytical model was also implemented in FEMM. Although FEMM does not simulate movement directly, it was possible to obtain the electromagnetic performance throughout the slip domain by using two different approaches: slip frequency or slip conductivity. The slip frequency approach varied the frequency in the conducting can by changing the supply frequency, whereas the slip conductivity approach varied the resistance in the can whilst maintaining a constant frequency. Both approaches were investigated and although they delivered the same torque values, the can losses differed due to the way in which the variation of the rotor with slip was modelled (see appendix B). The slip conductivity approach was chosen to make the comparison with the MLM because its constant frequency supply allowed operating under a complete constant voltage regime.

The MLM results were compared, for current and voltage operation, to those obtained using FEMM. The MLM results under current operation showed a very close agreement to FEMM. The MLM limitations of disregarding the saturation effect and simplifying the stator slotting into equivalent continuous layers were studied. When saturation was neglected in the MLM, the air gap flux density and the torque increased proportionally to the input current allowing the magnetic fields to achieve unrealistically high values, as opposed to the FE model where saturation prevented the fields from reaching such high levels. This translated into overestimating the torque in the MLM when saturation was present. Although regarding the stator slotting as continuous layers resulted in a good approximation of the peak values of the magnetic fields, the MLM was unable to account for the slotting effects in the magnetic field around the air gap. Despite this limitation, the torque of the MLM maintained good agreement with the torque obtained from the FE

model. In the voltage operation both the MLM and FEMM models used the same algorithm to approximate the voltage (by varying the input current). The relationship between voltage and current was established by means of the equivalent circuit. Once the voltage due to the magnetic fields in the stator slotting region was calculated, the winding leakage was added analytically to the voltage contribution because the MLM does not easily include external winding impedances. For the voltage operation, the accuracy of the MLM was slightly lower compared to current operation. When the current obtained under constant voltage operation in FEMM was fed into the MLM, the results were more accurate than the MLM operating under constant voltage because feeding the MLM with the exact current avoids approximating the external impedance in the MLM (under constant voltage operation). The greatest inaccuracies using the MLM under constant voltage operation were found at slips close to 1; this was attributed to the saturation being neglected in the analytical model. The resultant computing times in FEA and MLM were as follows: under current operation the MLM required 2 (secs), whilst the FEMM model 5 (mins); and under voltage operation 25 (secs) for the MLM and 38 (mins) for the FEMM model. There were two main factors that impacted the solution times in the analytical MLM: the number of harmonics used in the model, and the error bound used in the bisection method for the constant voltage operation.

Considering the simplicity of the MLM, the solution time and the accuracy of the results, which were in close agreement compared to the FE model, the MLM is well suited as a fast preliminary design tool in determining the electromagnetic performances of high-speed copper-coated induction machines.

6.2 Future work

There are two areas in which the MLM can be developed further: improving the accuracy of the MLM and reducing the solution times.

It is possible to take into account the saturation in the MLM as in [15]; here the layers are divided into several sub-layers and the permeability of the sub-layers is assigned the value which corresponds to the tangential field strength of the previous sub-layer. However, the approach used in this thesis would have to change because the procedure described above is carried out by assuming the field values at the lower boundary are transferred upwards and varied until the tangential field strength values match those of the current sheet. The determination of the fields in this thesis was found by transferring the admittance of the layers first, and then the fields (calculated from the current source), rather than transferring assumed values of the fields. A way to transfer the admittance in the layers whilst considering the effect of saturation in the MLM's layers could be explored. Another method to improve the accuracy of the MLM would be to divide the stator slotting region into more sub-layers to better account for the details of the stator slotting.

The solution times for the voltage operation MLM could be reduced by using another iterative method and by modifying the starting condition. The approach used here for convergence was initialised with a low value of current at every point in the slip domain. However, a reduction of the solution time would be achieved if the starting current for successive slips was the current determined from the previous slip instead of initialising it again at each step.

6.3 Publications

R. Velazquez, A.C. Smith, "Electromagnetic Modelling of High-speed Induction Motors", *in Proceedings of the 8th International Conference on Power Electronics, Machines and Drives (PEMD)*, Glasgow, UK, pp 1-6.

References

[1] M. Ikeda, S. Sakabe, and K. Higashi, "Experimental Study of High-speed Induction Motor Varying Rotor Core Construction," *IEEE Trans. Energy Convers.*, vol. 03, no. 01, pp. 98–103, 1990.

[2] D. Gerada, A. Mebarki, N. L.Brown, C. Gerada, A. Cavagnino, and A. Boglietti, "High-speed Electrical Machines–Technologies, Trends and Developments," *IEEE Trans. Ind. Electron.*, vol. 61, no. 6, pp. 2946–2959, 2014.

[3] J. F. Gieras, *Advancements in Electric Machines*, vol. 53, no. 9. 2013.

[4] J. Huppunen, "High-speed solid-rotor induction machine Electromagnetic calculation and design," Lappeenranta University of Technology, 2004.

[5] D. Ph and D. Phil, "Analysis of Solid-Rotor Induction Machine By," no. June, pp. 87–93, 1972.

[6] J. Pyrhönen, "The highs speed induction motor: Calculating the effects of solid rotor material on machine characteristics.," in *Acta Polytechnica Scandinavica Electrical Engineering Series no. 68*, Helsinki, 1991, p. 84.

[7] J. F. Gieras and J. Saari, "Performance Calculation for a High-Speed Solid-Rotor Induction Motor," *IECON 2010 - 36th Annu. Conf. IEEE Ind. Electron. Soc.*, vol. 59, no. 6, pp. 2689–2700, 2012.

[8] V. Raisanen, S. Suuriniemi, S. Kurz, and L. Kettunen, "Rapid computation of harmonic eddy-current losses in high-speed solid-rotor induction machines," *IEEE Trans. Energy Convers.*, vol. 28, no. 3, pp. 782–790, 2013.

[9] M. Mirzayee, H. Mehrjerdi, and I. Tsurkerman, "Analysis of a high-speed solid rotor induction motor using coupled analytical method and reluctance networks," *2005 IEEE/ACES Int. Conf. Wirel. Commun. Appl. Comput. Electromagn.*, vol. 2005, pp. 539–542, 2005.

[10] L. T. Ergene and S. J. Salon, "Determining the equivalent circuit parameters of canned solid-rotor induction motors," *IEEE Trans. Magn.*, vol. 41, no. 7, pp. 2281–2286, 2005.

[11] B. L. J. Gysen, K. J. Meessen, J. J. H. Paulides, and E. a Lomonova, "General

Formulation of the Electromagnetic Field Distribution in Machines and Devices Using Fourier Analysis," *Magn. IEEE Trans.*, vol. 46, no. 1, pp. 39–52, 2010.

[12] K. Boughrara, F. Dubas, and R. Ibtiouen, "2-D analytical prediction of eddy currents, circuit model parameters, and steady-state performances in solid rotor induction motors," *IEEE Trans. Magn.*, vol. 50, no. 12, 2014.

[13] M. Mirzayee, P. M. Mirsalim, H. Gholizad, and S. Javadi, "Combined 3D Numerical and Analytical Computation Approach for Analysis and Design of High-speed Solid Iron Rotor Induction Machines," no. 1, pp. 2–3.

[14] A. C. Smith, U. Brook Hansen, H. Willsamson, N. Benhama, L. Counter, and J. M. Papadopoulos, "Magnetic drive couplings," in *Ninth International Conference on Electrical Machines and Drives, 1999.*, 1999, no. 468, pp. 232–236.

[15] B. J. Chalmers and E. S. Hamdi, "New form of composite-rotor induction motor for fan drives," *IEE Proceedings, Electr. Power Appl.*, vol. 129, pp. 27–34, 1982.

[16] S. Greenberg, *Electric Motors*, vol. 2. Elsevier, 2004.

[17] M. a. Rahman, a. Chiba, and T. Fukao, "Super high-speed electrical machines - summary," *IEEE Power Eng. Soc. Gen. Meet. 2004.*, vol. 1, no. iii, pp. 1–4, 2004.

[18] J. Pyrhonen, T. Jokinen, and V. Hrabovcova, *Design of Rotating Electrical Machines*. Wiley.

[19] A. Borisavljevic, *Limits Modeling and Design of High-speed PM machine*. 2013.

[20] R. Lateb, J. Enon, and L. Durantay, "High-speed, high power electrical induction motor technologies for integrated compressors," *Proc. - 12th Int. Conf. Electr. Mach. Syst. ICEMS 2009*, 2009.

[21] J. Lähteenmäki, "Design and voltage supply of high-speed induction machines," Helsinki University of Technology, 2002.

[22] T. Mauffrey, "Comparison of 5 different squirrel cage rotor designs for large high-speed induction motors," pp. 1–9, 2013.

[23] M. Larsson, M. Johansson, L. Naslund, and J. Hylander, "Design and evaluation of high-speed induction machine," *IEEE Int. Electr. Mach. Drives Conf. 2003. IEMDC'03.*, vol. 1, pp. 77–82, 2003.

[24] Y. Kim, M. Choi, K. Suh, Y. Ji, and D. Wang, "High-speed Induction Motor Development for Small Centrifugal Compressor," *Proc. Fifth Int. Conf. Electr. Mach. Syst.*, pp. 891–894, 2001.

[25] M. Modreanu, N. Ivan, and T. Tudorache, "Numerical Modeling of a Small Power High-speed Induction Motor," in *The 7th International Symposium on Advanced*

Topics in Electrical Engineering, 2011, pp. 3–6.

[26] H. Zhou and F. Wang, "Comparative Study on High-speed Induction Machine with Different Rotor Structures," *Int. Conf. Electr. Mach. Syst. 2007. ICEMS.*, pp. 1009–1012, 2007.

[27] K. Dorairaj and M. Krishnamurthy, "Polyphase Induction Machine with a Slitted Ferromagnetic Rotor: II - Analysis," *IEEE Trans. Power Appar. Syst.*, vol. PAS-86, no. 7, pp. 844–855, 1967.

[28] P. K. Rajagopalan and V. B. Murty, "Effects of Axial Slits on the Performance of Induction Machines with Solid Iron Rotors," *IEEE Trans. Power Appar. Syst.*, vol. PAS-88, no. 11, pp. 1695–1709, 1969.

[29] Y. Gessese, A. Binder, and B. Funieru, "Analysis of the effect of radial rotor surface grooves on rotor losses of high-speed solid rotor induction motor," *SPEEDAM 2010 - Int. Symp. Power Electron. Electr. Drives, Autom. Motion*, no. 2, pp. 1762–1767, 2010.

[30] J. Klíma and O. Vítek, "Analysis of high-speed induction motor," in *16th International Conference on Mechatronics - Mechatronika (ME)*, 2014, no. 4.

[31] Y. Gessese and A. Binder, "Axially slitted, high-speed solid-rotor induction motor technology with copper end-rings," *Proc. - 12th Int. Conf. Electr. Mach. Syst. ICEMS 2009*, pp. 2–7, 2009.

[32] J. Pyrhönen, J. Nerg, A. Mikkola, J. Sopanen, and T. Aho, "Electromagnetic and mechanical design aspects of a high-speed solid-rotor induction machine with no separate copper electric circuit in the megawatt range," *Electr. Eng.*, vol. 91, no. 1, pp. 35–49, 2009.

[33] J. Pyrhonen, J. Nerg, P. Kurronen, and U. Lauber, "High-Speed High-Output Solid-Rotor Induction-Motor Technology for Gas Compression," *IEEE Trans. Ind. Electron.*, vol. 57, no. 1, pp. 272–280, 2010.

[34] T. Aho, J. Nerg, and J. Pyrhonen, "Experimental and Finite Element Analysis of Solid Rotor End Effects," *IEEE Int. Symp. Ind. Electron. 2007. ISIE 2007.*, pp. 1242–1247, 2007.

[35] M. Ahrens, U. Bikle, R. Gottkehaskamp, and H. Prenner, "Electrical design of high-speed induction motors of up to 15 MW and 20000 RPM," *IEEE Power Electron. Mach. Drives*, pp. 381– 386, 2002.

[36] M. Jagieła, J. Bumby, and E. Spooner, "Time-domain and frequency-domain finite element models of a solid-rotor induction/hysteresis motor," *IET Electr. Power*

Appl., vol. 4, no. 3, p. 185, 2010.

[37] S. L. Ho, Y. Zhao, and W. N. Fu, "Adaptive discontinuous galerkin method for transient analysis of eddy current fields in high-speed rotating solid rotors," *IEEE Trans. Magn.*, vol. 50, no. 2, 2014.

[38] A. H. O, M. O. G, and D. A. K, "Design and optimization of an axially-slitted high-speed solid rotor induction motor," pp. 568–573.

[39] T. S. Mekhtoub, "Complex Finite Element Analysis of," pp. 1606–1610.

[40] Y. Hu, J. Chen, and X. Ding, "Analysis and computation on magnetic field of solid rotor induction motor," *IEEE Trans. Appl. Supercond.*, vol. 20, no. 3, pp. 1844–1847, 2010.

[41] M. Johansson, M. Larsson, L. Naslund, and J. Hylander, "Small high-speed induction motors," *IEMDC 2003 - IEEE Int. Electr. Mach. Drives Conf.*, vol. 1, pp. 279–284, 2003.

[42] J. F. Gieras and J. Saari, "Performance calculation for a high-speed solid-rotor induction motor," *IEEE Trans. Ind. Electron.*, vol. 59, no. 6, pp. 2689–2700, 2012.

[43] S. S. Rao, *The Finite Element Method in Engineering*, 5th ed. Elsevier Science, 2011.

[44] G. R. Liu and S. S. Quek, *The finite element method: a practical course*. Elsevier Science, 2013.

[45] H. A. Toliyat and G. B. Kliman, *Handbook of Electric Motors*. CRC Press, 2004.

[46] K. Hameyer and R. Belmans, *Numerical modelling and design of electrical machines and devices*. WIT Press, 1999.

[47] J. R. Brauer, L. A. Larkin, and B. E. Macneal, "Higher order 3D isoparametric finite elements for improved magnetic field calculation accuracy," *IEEE Trans. Magn.*, vol. 27, no. 5, pp. 4185–4188, 1991.

[48] J. R. Brauer, G. A. Zimmerlee, T. A. Bush, and R. J. Sandel, "3D Finite element analysis of automotive alternator under any load," *IEEE Trans. Magn.*, vol. 24, no. 1, pp. 500–503, 1988.

[49] J. R. Brauer, B. E. MacNeal, L. A. Larkin, and V. D. Overbye, "New Method of Modeling Electronic Circuits Coupled With 3D Electromagnetic Finite Element Models," *IEEE Trans. Magn.*, vol. 27, no. 5, pp. 4085–4088, 1991.

[50] J. R. Brauer and B. E. MacNeal, "Finite element modeling of multiturn windings with attached electric circuits," *IEEE Trans. Magn.*, vol. 29, no. 2, pp. 1693–1696, 1993.

[51] J. R. Brauer, S. M. Schaefer, J. F. Lee, and R. Mittra, "Asymptotic boundary condition for three dimensional magnetostatic finite elements," *IEEE Trans. Magn.*, vol. 27, no. 6, pp. 5013–5015, 1991.

[52] A. Suhaimi, "Failure Analysis of Cable Accessories Using Finite Element Method Magnetics (FEMM) Software," in *2012 International Conference on Condition Monitoring and Diagnosis (CMD)*, 2012, pp. 995–998.

[53] T. Benamimour, A. Bentounsi, and H. Djeghloud, "CAD of electrical machines using coupled FEMM-MATLAB softwares," *2013 3rd Int. Conf. Electr. Power Energy Convers. Syst.*, pp. 1–6, 2013.

[54] Z. Zakaria, M. S. Badri Mansor, A. H. Jahidin, and M. S. Z. Azlan, "Simulation of magnetic flux leakage (MFL) analysis using FEMM software," in *2010 IEEE Symposium on Industrial Electronics and Applications (ISIEA)*, 2010, pp. 481–486.

[55] E. Saraiva, M. L. R. Chaves, and J. R. Camacho, "Three-phase transformer representation using FEMM, and a methodology for air gap calculation," in *18th International Conference on Electric Machines*, 2008, pp. 1–6.

[56] N. Grilo, D. M. Sousa, and A. Roque, "AC motors for application in a commercial electric vehicle: Designing aspects," in *2012 16th IEEE Mediterranean Electrotechnical Conference (MELECON)*, 2012, pp. 277–280.

[57] P. Grmela, M. Mach, and V. H. M. Ieee, "Permanent magnet DC motor re-design by FEMM," in *2011 International Aegean Conference on Electrical Machines and Power Electronics and 2011 Electromotion Joint Conference (ACEMP)*, 2011, pp. 666–669.

[58] J. K. Kamoun, N. Ben Hadj, M. Chabchoub, R. Neji, and M. Ghariani, "An Induction Motor FEM-Based Comparative Study : Analysis of Two Topologies," in *2013 8th International Conference and Exhibition on Ecological Vehicles and Renewable Energies (EVER)*, 2013, pp. 1–5.

[59] M. R. Hachicha, N. Ben Hadj, M. Ghariani, and R. Neji, "Finite element method for induction machine parameters identification," in *2012 First International Conference on Renewable Energies and Vehicular Technology (REVET)*, 2012, pp. 490–496.

[60] D. Meeker, "Finite Element Method Magnetics Version 4.2 User Manual," 2010. [Online]. Available: http://www.femm.info/Archives/doc/manual42.pdf.

[61] J. W. Arthur, "An elementary view of maxwell's displacement current," *IEEE*

Antennas Propag. Mag., vol. 51, no. 6, pp. 58–68, 2009.

[62] D. Meeker, "Induction Motor Example," 2002. [Online]. Available: http://www.femm.info/wiki/InductionMotorExample. [Accessed: 20-Aug-2015].

[63] R. Ierusalimschy, *Programming in Lua*, 2nd ed. lua.org, 2006.

[64] D. Meeker, "Finite Element Method Magnetics: OctaveFEMM," 2010. [Online]. Available: http://www.femm.info/Archives/doc/octavefemm.pdf. [Accessed: 16-Nov-2015].

[65] E. Mishkin, "Theory of the squirrel-cage induction machine derived directly from Maxwell's field equations," *Q. J. Mech. Appl. Math.*, vol. 7, no. July 1953, 1954.

[66] A. L. Cullen and T. H. Barton, "A simplified electromagnetic theory of the induciton motor, using the concept of wave impedance," *Proc. IEE - Part C Monogr.*, vol. 105, no. 8, pp. 331–336, 1958.

[67] L. A. Pipes, "Matrix theory of skin effect in laminations," *J. Franklin Inst.*, vol. 262, no. 2, pp. 127–138, 1956.

[68] J. Greig and E. M. Freeman, "Travelling-wave problem in electrical machines," *Proc. Inst. Electr. Eng.*, vol. 114, no. 11, pp. 1681–1683, 1967.

[69] E. M. Freeman, "Travelling waves in induction machines: input impedance and equivalent circuits," *Proc. Inst. Electr. Eng.*, vol. 115, no. 12, pp. 1772–1776, 1968.

[70] S. Williamson, "The anisotropic layer theory of induction machines and induction devices," *IMA J. Appl. Math.*, vol. 81, no. 1, pp. 370–373, 1976.

[71] S. Williamson and A. C. Smith, "Field analysis for rotating induction machines and its relationship to the equivalent-circuit method," *IEE Proc. B Electr. Power Appl.*, vol. 127, no. 2, pp. 83–90, 1980.

[72] E. Peralta, "Analysis of Canned Line-Start Permanent Magnet Motors," University of Manchester, 2006.

[73] T. D. Cox, "Development of Novel Linear Drive Machines," Bath, 2008.

[74] M. Fujimoto, *Physics of Classical Electromagnetism*, vol. 1. Springer, 2007.

[75] C. G. Veinott, *Theory and design of small induction motors*. 1986.

Appendix A

Dimensions of the Induction Machine Model

This appendix provides the dimensions and electrical specifications of the machine.

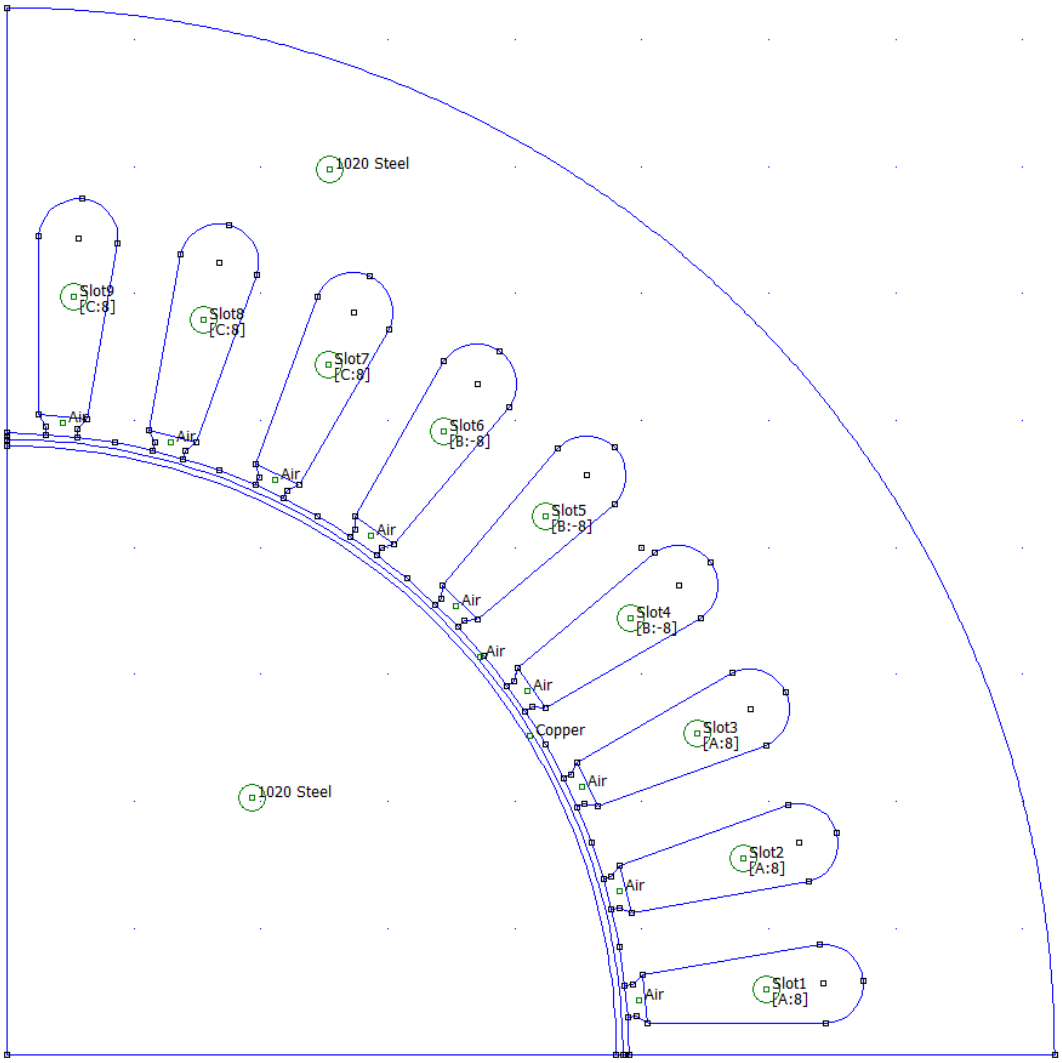

Figure A.1 Quarter of the geometry of the copper-coated HSIM.

Parameter	**Value**
Stator frequency	800 (Hz)
Per phase voltage	120 (V_{RMS})
Number of phases / pair poles	3
Number of pair poles	2
Number of stator slots	36
Number of turns per coil	12
Rotor core radius	48 (mm)
Copper can width	0.5 (mm)
Air gap width	0.5 (mm)
Outer radius	82.5 (mm)
Axial length	150 (mm)

Table A.1 Motor parameters.

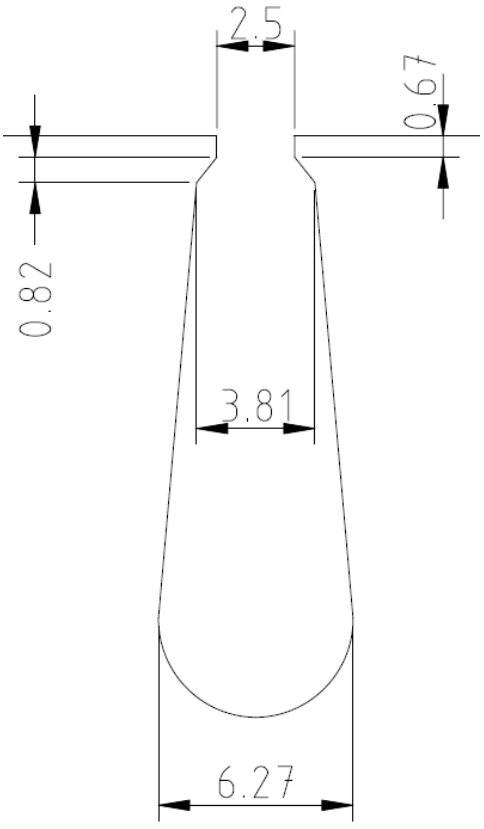

Figure A.2 Slot dimensions (mm).

Appendix B

Relationship between the slip frequency and slip conductivity approaches in FEMM

There are two approaches that can be used to obtain the electromagnetic performance of the copper-coated HSIM in FEMM. Comparing their results, both approaches had the same torque values (Figure B.1) but for the can losses their values differed (Figure B.2). In this appendix an explanation for this is provided.

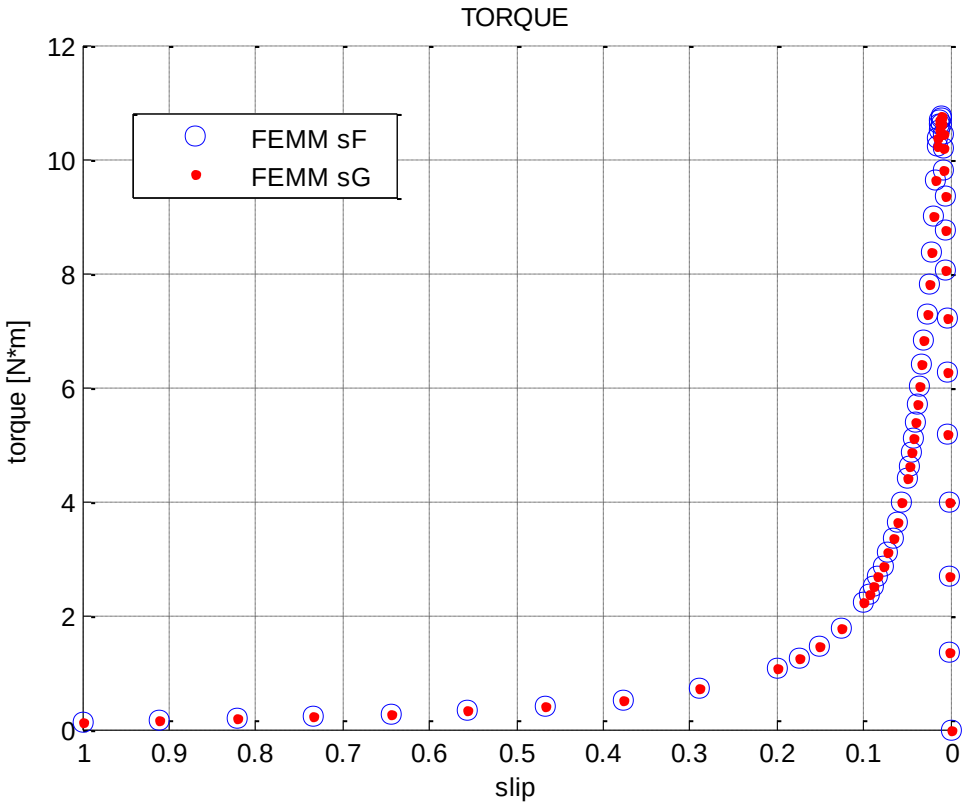

Figure B.1 Torque developed.

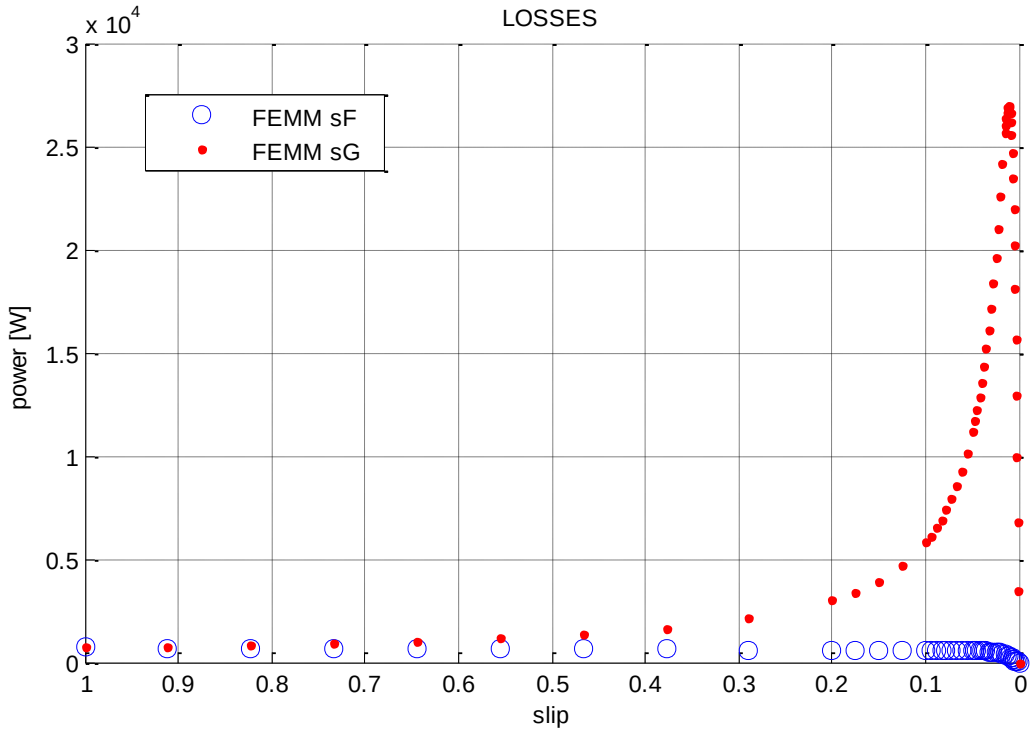

Figure B.2 Rotor can losses.

In the slip frequency approach (sF), the problem frequency is varied from zero up to the stator line frequency whilst maintaining the conductivity of the copper can constant. The resistance of the copper layer is given by:

$$R_{sF} = \frac{l}{\sigma A} \tag{B.1}$$

The electric field induced in the copper can is proportional to the rate of change of the magnetic field. This is also proportional to the frequency of the problem in FEMM (the slip frequency):

$$e \propto \frac{dB}{dt} \propto (sF)B \tag{B.2}$$

In terms of the circuit parameters, the voltage induced in the can depends on the current inside the can and the impedance of the can:

$$e = i_{can}\left(r_{can} + j \cdot sF \cdot L_{can}\right) \tag{B.3}$$

The rotor can losses are:

$$P_{loss}^{sF} = i_{can}^2 r_{can} \tag{B.4}$$

For the case of the slip conductivity approach (sG), the frequency of the problem remains constant whilst the conductivity of the can is varied from zero up to the normal conductivity of the copper can.

$$R_{sG} = \frac{l}{s\sigma A} \tag{B.5}$$

The electric field induced in the can is:

$$e \propto \frac{dB}{dt} \propto F \cdot B \tag{B.6}$$

In terms of the circuit parameters, the electric field becomes:

$$e = i_{can}\left(\frac{r_{can}}{s} + j \cdot F \cdot L_{can}\right) \tag{B.7}$$

The rotor can losses are:

$$P_{loss}^{sG} = i_{can}^2 \frac{r_{can}}{s} \tag{B.8}$$

Dividing eqn. B.4 by the slip:

$$\frac{P_{loss}^{sF}}{s} = i_{can}^2 \frac{r_{can}}{s} \tag{B.9}$$

It can be seen that the right-hand term of eqn. B.8 is the same as eqn. B.9, thus:

$$P_{loss}^{sG} = \frac{P_{loss}^{sF}}{s} \tag{B.10}$$

Eqn. B.10 describes the relationship between the slip conductivity and slip frequency approaches for the can losses that is shown in Figure B.2

In addition, the mechanical power can be determined by subtracting the loss from the slip frequency approach from the slip conductivity approach:

$$P_{loss}^{sG} - P_{loss}^{sF} = P_{can}^{sF}\left(\frac{1}{s} - 1\right) \tag{B.11}$$

Then:

$$P_{can}^{sF}\left(\frac{1}{s} - 1\right) = Ts\omega_s\left(\frac{1-s}{s}\right) \tag{B.12}$$

And finally:

$$Ts\omega_s\left(\frac{1-s}{s}\right) = T\omega_r \tag{B.13}$$

Appendix C

Reference Frame of the Travelling Field in the MLM

The reference frames attached to the stator and rotor are illustrated in Figure C.1

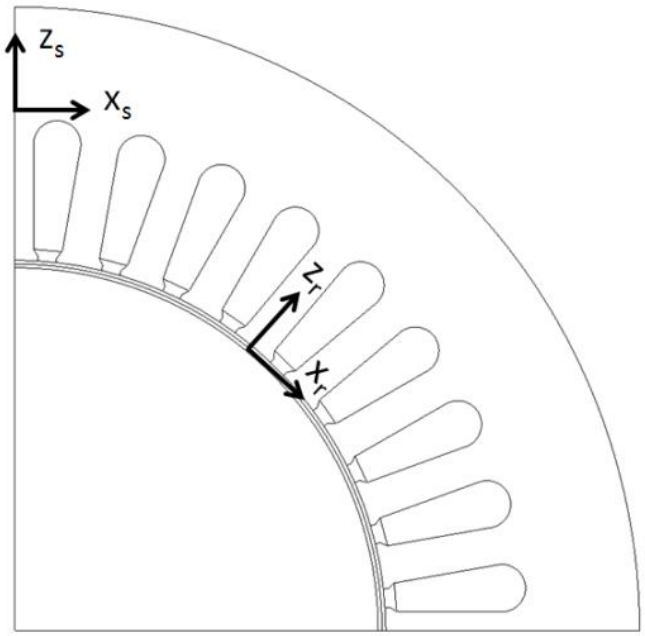

Figure C.1 Reference frames on the stator (s) and rotor (r).

If the stator and rotor are represented as layers, with the rotor layer moving at velocity *v* at an instant time *t*, then the reference frames can be represented in a Cartesian coordinate system.

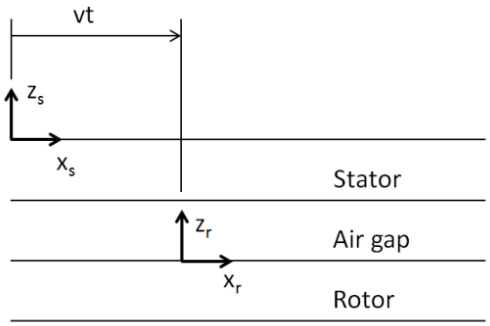

Figure C.2 Reference frames in the layer model.

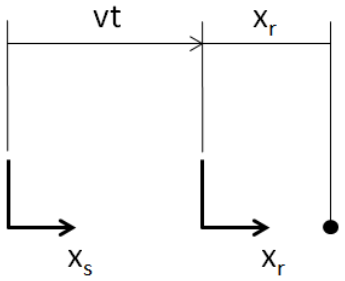

Figure C.3 Relationship between frames along x direction.

From Figure C.3 the relationship between reference frames is straightforward:

$$x_s = vt + x_r \tag{C.1}$$

Recalling that the tangential rotor velocity *v* is proportional to its rotor angular speed and diameter along with the concept of slip frequency (eqns. C.2 and C.3 respectively):

$$v = \omega_r \frac{D}{2} \tag{C.2}$$

$$s\omega_s = \omega_s - p\omega_r \tag{C.3}$$

From eqns. C.2 and C.3 the rotor velocity *v* can be expressed in terms of the slip and stator angular frequency ω_r resulting in:

$$\omega_s t - kx_s = s\omega_s t - kx_r \tag{C.4}$$

Where *k*, the wave number, takes into account the space harmonics:

$$k = \frac{2}{D} p\upsilon \tag{C.5}$$

Consequently for the reference frame attached to the stator, the fields vary as:

$$e^{j(\omega_s t - kx_s)} \tag{C.6}$$

And for the rotor reference frame the fields vary as:

$$e^{j(s\omega_s t - kx_r)} \tag{C.7}$$